Self-consistent modeling of ice-sheet evolution and paleoclimate

Jessica Marie Drees Lundin

A dissertation submitted in partial fulfillment of
the requirements for the degree of

Doctor of Philosophy

University of Washington

2012

Edwin D. Waddington, Chair

Howard Conway

Loyce Adams

Edward Brook

Eric Steig

Program Authorized to Offer Degree:
Geophysics

University of Washington

Abstract

Self-consistent modeling of ice-sheet evolution and paleoclimate

Jessica Marie Drees Lundin

Chair of the Supervisory Committee:
Professor Edwin D. Waddington
Earth and Space Sciences

A self-consistent approach has been developed to determine past climate histories while simultaneously determining the past ice-sheet evolution. We recognize that multiple physical processes are affected by the same climate history and ice-sheet evolution. By combining several processes into one self-consistent model based on physics of ice-sheet flow, heat flow, grain growth, and firn compaction, I can infer the climate history (accumulation rate and delta-age) and ice-sheet evolution (thickness and divide position), that match data sets from ice cores and ice-penetrating radar layers. Ice-sheet behavior has not previously been modeled to enforce self consistency. The self-consistent approach consists of modules, or subroutines, representing physical processes. I have developed forward models to simulate firn densification, grain growth, heat transfer, and ice flow, and inverse models to infer histories including the spatial pattern of accumulation, and the depth-age relationship for ice cores and radar layers. While individual modules can be replaced with modules based on a variety of physical approximations, I provide here proof of the concept that multiple data sets and multiple processes can be combined to provide improved estimates of ice-sheet histories that cannot be directly measured. This new approach provides a way to improve ice-core chronologies from Greenland and Antarctica, and to infer self-consistent histories of climate and ice-sheet evolution at those locations.

TABLE OF CONTENTS

LIST OF FIGURES

LIST OF TABLES

GLOSSARY

ACCUMULATION: All processes that add to the mass of the glacier. The main process of accumulation is snowfall. Accumulation also includes deposition of hoar, freezing rain, solid precipitation in forms other than snow, gain of wind-borne snow, avalanching and basal accumulation [*Cogley et al.*, 2011].

CRYOSPHERE: One of the earth's spheres of irregular form existing in the zone of interaction of the atmosphere, hydrosphere and lithosphere, distinguished by negative or zero temperature and the presence of water in the solid or super-cooled state; the term refers collectively to the portions of the earth where water is in solid form, including snow cover, floating ice, glaciers, ice caps, ice sheets, seasonally frozen ground and perennially frozen ground (permafrost) [*NSIDC*, undated].

DIVIDE FLOW: Polar ice-sheet Ice divides often form on basal ridges and domes and have different dominating stress terms. At an ice divide, the slope is undefined and the dominant deviatoric stresses are longitudinal, τ_{xx} and τ_{yy}, rather than shear, τ_{xz} or τ_{xy} [*Cuffey and Paterson*, 2010].

FIRN: (1) Snow that has survived at least one ablation season but has not been transformed to glacier ice. (2) Structurally, the metamorphic stage intermediate between snow and ice, in which the pore space is at least partially interconnected, allowing air and water to circulate; typical densities are 400-830 kg m^3. In this sense, the firn is generally up to a few tens of meters thick on a temperate glacier that is close to a steady state, and up to or more than 100m thick in the dry snow zone on the ice sheets [*Cogley et al.*, 2011].

ICE DYNAMICS: Ice dynamics refers to the movement of ice as a visco-elastic material in response to stress. Ice is the most dynamic solid, which flows like a liquid given long enough timescales.

ICE FLOW: The motion of ice driven by gravitational forces [*American Meteorogical Society*, 2000].

INVERSE APPROACH: A method consisting of a forward model and an inverse model, used to solve for unknown boundary conditions, initial conditions and coefficients.

LAST GLACIAL MAXIMUM: The Last Glacial Maximum (LGM) was the maximum extent of ice during the most recent glacial period, at 20 *ka* [*Cuffey and Paterson*, 2010].

PERSISTENCE: The previous value in a time series. Thus, if $x(t)$ denotes the present value, the value of persistence would be $x(t-1)$, whence the latter value is regarded as 'persisting' [*American Meteorogical Society*, 2000].

ACKNOWLEDGMENTS

First I would like to acknowledge Ed Waddington for his outstanding mentorship. It is an honor to work with such a great scientist. Thank you, Ed, for being a generous teacher and providing a role model for how to be an effective scientist, incorporating characteristics of kindness, respect, and quality. A big thanks to my reading committee Twit (Howard Conway) and Loyce Adams for helpful comments and editing, which helped broaden my scientific perspective and sharpen this dissertation. Thank you to the rest of the committee: Eric Steig and Ed Brook, for your feedback and encouragement. Thank you to Cecelia Bitz for serving as the committee Graduate Student Representative (GSR). Thank you to each committee member for feedback to improve this dissertation and the future publications.

Thank you to John, my co-captain and partner. Thank you to Mom and Dad for your encouragement and support of my pursuits in math and science. Thanks to Matt, Cress, and Alex.

Thank you to Michelle Koutnik, for assistence with 2-d flowband modeling and inverse methods. Thank you to Andy Ganse, Ken Creager and John Booker for conversations about inverse theory and geophysics. Thanks Anais Orsi for discussion of firn processes including densification and gas transport. Thank you to the Glaciology group. Thank you to my officemates over the years including: Twila Moon, Joe MacGregor, Michelle Koutnik, Steve Price, Al Rasmussen, Shelley Kunasek, Aurora Burd, Kristin Poinar, Brook Medley, and Kat Huybers. Thank you to previous and current grads Erin Whorton, Jonathan Claridge, Dave Argento, Mike Town, Spruce Shoenemann, Robert Sheerer, Rachel Headly, T.J. Fudge, Regina Carns, Adam Campbell, Max Stevens, Emily Newsom, Dan Kluskiewicz, and Mike Hay.

Thank you to the Amath and ESS department faculty and staff. Thank you to Ed Mulligan and Ali for keeping my computers functioning.

I would like to acknowledge colleagues I have been to the field with including Kenny Matsuoka, Ian Howit, Ellyn Enderlin, Able Brown, Ben Smith, and Dave Besson.

Thank you to National Science Foundation Office of Polar Programs (NSF OPP) grants, and UW NSF Amath and OACIS GK-12 grants.

DEDICATION

To my family: John, Mom, Dad, Matt+Cress and Alex.

Chapter 1

INTRODUCTION

1.1 The self-consistent approach

What is self consistency? I approach this work recognizing that ice sheets are self-consistent systems. My work seeks to 'think like an ice sheet' by combining methods from several previously addressed questions into one self-consistent method. Instead of focusing on one time or spatial scale to address a particular question, I have incorporated several modules into one self-consistent model. Paleoclimate histories including temperature and accumulation-rate are important for many ice-sheet processes, including firn densification and internal deformation of ice.

The self-consistent approach has implications for how climate records from ice sheets are interpreted. Ice sheet-volume (and thickness) is related to sea-level elevation; ice sheets gain and lose mass in glacial and interglacial periods. However, some more complicated processes including sources for meltwater pulses and ice-rafted debris events (such as Heinrich events), are poorly understood. Insight into past ice-sheet evolution is important for understanding the global paleoclimate picture in which ice sheets contribute directly to sea-level. Direct estimates of accumulation-rate histories from ice-sheet studies can improve Global Circulation Models of past climates in the polar regions.

Previous work by *Lemieux-Dudon et al.* [2010] incorporated several models into one method to date several Antarctic ice cores to match the same methane gas record, resulting in harmonized dating of the EDML and EPICA ice cores. The focus of the *Lemieux-Dudon et al.* method was on the dating of ice and atmospheric-gas histories from ice cores alone, and did not attempt to infer the past ice-sheet evolution. My approach is a distinct contribution beyond that method, because I am incorporating radar-layer data, which provide a rich spatial data set to complement the great temporal resolution from ice cores. I want to improve depth-age estimates by including 2-d effects, including spatial

histories of accumulation rate. By incorporating spatial and temporal data, and using a combination of models in a self-consistent fashion, I determine improved chronologies ice cores and for ice-penetrating radar-layer stratigraphy. Additionally, I infer the past ice-sheet evolution, including ice thickness and divide migration. I also infer climate histories including the accumulation-rate (precipitation minus evaporation) history, where upstream effects not captured in a 1-d model are important.

The self-consistent method presented in this thesis is a significant advance over previous work by formally recognizing that dating the ice and inferring the ice-sheet evolution are not distinct problems. The most-accurate method for dating an ice core incorporates the past ice-sheet evolution, including ice dynamics to incorporate realistic histories of accumulation-rate. Inferring the past ice-sheet evolution requires knowing the dates of stratigraphic layers.

1.2 Background

Interpreting paleoclimate records requires understanding of the record keeper. For example, ocean-sediment cores have preserved Foraminifera fossils that provide information about the past chemistry and temperature of the ocean. Assemblages of tree rings are pieced together to produce a continuous record, and past precipitation and temperature can be inferred from that record. In the realm of paleoclimate records, ice cores and ice-penetrating radar data sets are special because of their location in polar regions, providing an important puzzle piece to the picture of climate change. Ice sheets both record climate and respond to climate through time. As recorders, ice sheets preserve information from polar regions where the most significant changes between glacial and interglacial swings occur. Ice sheets respond to climate forcing in numerous ways, most notably through changes in extent and volume. A better understanding of climate records and ice-sheet evolution in response to climate can be determined by incorporating physical approximations to represent ice-sheet deformation. Ice cores give a one-dimensional, high-resolution temporal record of paleoclimate. Ice-penetrating radar provides a two-dimensional spatial picture of the inner workings of an ice sheet. For example, radar-detected layers (generally assumed to be isochrones) can be dated through intersections with dated ice cores. Combining these data sets yields both temporal and spatial information. Ultimately the goal is to make better

climate inferences, including improved dating of the ice cores and isochrone architecture, and better constraints on past ice-sheet evolution. This work improves climate records from ice sheets while providing better constraints on past ice-sheet evolution through thermo-mechanical modeling and inverse-theory techniques. Data sets come from ice-core chemistry and ice-penetrating radar isochrones. Products from this work include improved ice-core chronologies, which support better interpretation of paleoclimate records through more precise timing of changes in atmospheric composition, temperature and accumulation rate (precipitation minus evaporation). From improved dating of stratigraphic layers detected by ice-penetrating radar, this work provides improved information of ice-sheet evolution to support more accurate global climate modeling, where ice-sheets remain poorly represented.

1.3 Ice-sheet observations and modeling

1.3.1 Ice-core chemistry

Ice-core chemistry data sets are some of the best paleoclimate records from 800 ka to present. What makes these records so useful for paleoclimate interpretation is the high temporal resolution, which allows precise timing of climate events. Ice chemistry, including proxies and direct measurements, provides a window into the past climate. Ice cores provide the only direct measurement of past atmospheric composition, including detailed records of sulfates, nitrates, carbon dioxide and methane, among other constituents. Snowflakes (H_2O) that become incorporated into an ice sheet provide local temperature records through hydrogen (δD) and oxygen ($\delta^{18}O$) isotopes. Through combining isotopic fractionations from hydrogen and oxygen, the deuterium excess ($d = \delta D - 8 \times \delta^{18}O$) can be evaluated to reveal disequilibrium processes at source regions [*Jouzel et al.*, 2007]. New laboratory techniques are improving the temporal resolution of these data. Laser measurements [*Van Trigt et al.*, 2002] can quickly measure ice-core chemistry within days at improved temporal resolution, work that would take years by more traditional methods. These new techniques promise to add to the richness of the paleoclimate interpretation from ice chemistry.

Ice-core records allow us to look at Earth's climate back to the Eemian Interglacial period 123 ka in Greenland [*Andersen et al.*, 2004] and to 800 ka in Antarctica [*EPICA*

members, 2004], with the prospect that ice one million years old or older may be recovered from Dome A. Interpreting the Greenland and Antarctic ice cores together provides a bipolar picture of Earth's climate. Greenland glacial records are characterized by a sequence of rapid warming and slow cooling, known as Dansgaard-Oeschger (DO) events, where warming is preceded by Heinrich events. The bipolar seesaw describes the offset between the two poles: when Greenland warms, Antarctica cools [*Broecker*, 1998] and the opposite is observed, when Antarctica cools, Greenland warms. From high-temporal-resolution records of atmospheric gas and temperature from ice cores, we begin to assemble the puzzle pieces for determining the physical processes in the atmosphere and ocean that can create such a pattern. Combining this information with temperature reconstructions (from oxygen and carbon isotopes) from cave records with high-temporal resolution (Th/U dating) in the equatorial regions [*Paulsen et al.*, 2003], allows a more complete picture of a complex system of physical processes that dominate large-scale changes in the Earth system.

Combining ice-core records is useful to both extend and refine chronologies. The Greenland Ice Sheet Chronology 2005 (GICC05) timescale [*Andersen et al.*, 2010; *Svensson et al.*, 2010; *Vinther et al.*, 2006; *Rasmussen et al.*, 2006] is an assemblage of ice-core records, created by using the best core for each section of the chronology, and updating the other cores to match. Volcanic-ash layers were used to align the records. This effort required much time and expense but yielded a tremendous chronology on which all of the Greenlandic records can be compared.

Greenlandic records can be extended to Antarctica through the record of methane, which is well-mixed in the atmosphere. Methane has an atmospheric residence time of 8-12 years, which is greater than the 2 years required to mix across the equator. Dated methane events in Greenlandic records can then be extended to Antarctic records [*Blunier and Brook*, 2001; *Brook et al.*, 2005] to assist dating of more-challenging Antarctic records where annual layers cannot be counted. Antarctic ice cores are generally more difficult to date, due to lower accumulation rates than in Greenland. Lower surface accumulation rates produce thinner annual layers, which are more difficult to count, contributing to a higher uncertainty in the dating. West Antarctic Ice Sheet (WAIS) ice cores, including WAIS Divide promise to be exceptions to poorly dated East Antarctic cores.

The reason methane has not already dated all of the Antarctic cores from the GICC05 chronology is that atmospheric gas (including methane) and ice from the same year are stored in different locations within the ice sheet. Firn, which is snow that is older than a year, accumulates at the surface and over the course of hundreds to thousands of years metamorphoses into ice. Younger atmospheric gas diffuses into the firn until it is trapped in bubbles deep in the firn column. Delta-age, the difference in the age of the gas and the age of the ice, varies through time depending on accumulation rate and temperature. Current values for delta-age are on the order of hundreds of years (Greenland and West Antarctica) and thousands of years (East Antarctica).

For interpretations that link temperature with carbon dioxide and other atmospheric gases, great care must be taken in aligning the two records into a single chronology. It is as if there are two story lines, one for ice (and the isotope temperature proxy stored in the ice) and the other for atmospheric gas, stored in trapped bubbles and clathrates surrounded by older ice. Properly assigning the delta-age is important, because otherwise the correct relative timing of events may be obscured. For example, the rapid warmings in Antarctica records are characterized by increases in temperature with a subsequent 800 year lag in carbon dioxide increases [*Caillon*, 2003]. If the delta-age is incorrect, it would be possible to misinterpret differences in the timing of temperature and atmospheric gas changes.

1.3.2 Ice-Penetrating Radar

Ice-penetrating radar is a useful tool for measuring internal stratigraphy and thickness of glaciers and ice sheets [*Bogorodskii et al.*, 1985, e.g.]. Radio-echo sounding can be used to image internal layers, and to determine the ice thickness. Radar-detected layers (generally assumed to be isochrones) are not usually annually resolved, but they can be used to spatially extrapolate depth-age relations from ice cores. Uncertainty in the depth of a radar-detected layer arises from uncertainty in the wave speed in ice (about 2 m μs^{-1}, which corresponds to 1.2% of the depth of the layer), and uncertainty in picking the two-way travel time to the layer. Uncertainty in two-way travel time depends on the radar system; for a 2MHz system the uncertainty is about 0.1 μs, or 8.5m. Assuming that the two uncertainties are

uncorrelated, the depth uncertainty is 42 m for 3400 m thick ice [*Conway and Rasmussen*, 2009]. Comparatively, ice cores typically have very small uncertainty in depth, arising from piecing together cores end-to-end in core-processing lines. While ice radar does not provide the same temporal resolution as ice cores, the insight gained from extending ice-core records spatially can be very useful. In the Taylor Dome core, ice radar revealed two changes in storm direction, where windward and leeward directions reversed [*Morse et al.*, 1998]. The WAIS Divide core shows a clear spatial pattern in accumulation rate [*Morse et al.*, 2002; *Neumann et al.*, 2008], as evidenced by the thickness gradient of radar layers. Ice radar is a useful tool for connecting records from nearby ice cores, such as GRIP with GISP2 in Greenland, and WAIS with Byrd in Antarctica. The only limits for connecting ice-core records are the distances that one can trace volcanic and other isochrones, and difficulty in tracking continuous layers through regions of fast-flowing ice [*Welch and Jacobel*, 2003].

1.3.3 Numerical modeling and inverse methods

Scientific computing allows us to use known physics of ice deformation to interpret observed phenomena. Modeling is crucial for filling the gaps between field observations, and for estimating phenomena that cannot be directly observed, including boundary conditions and initial conditions. Inverse methods can also be used to better understand dominant physical processes through parameter estimation for terms in equations that represent physical systems. I use forward models to estimate heat flow and ice-sheet flow, in order to learn about past ice dynamics and to improve dating of ice cores and radar layers.

The inverse theory approach consists of a forward problem and an inverse problem. The forward algorithm makes predictions of observable data quantities, based on appropriate physics and values of those parameters. The inverse problem is designed to infer unknown parameters, boundary conditions, and initial conditions from data. Inverse methods have been paired with ice-sheet models to infer surface temperatures [*Cuffey and Clow*, 1997; *Dahl-Jensen et al.*, 1998, e.g.], basal sliding [*Raymond and Gudmundsson*, 2009; *Truffer*, 2004], geothermal flux [*Buchardt and Dahl-Jensen*, 2007], accumulation-rate patterns [*Koutnik*, 2009; *Waddington et al.*, 2007; *Steen-Larsen et al.*, 2010], and ice-core dates [*Parrenin*

et al., 2007].

In this work, I solve a non-linear problem to determine spatial histories of accumulation rate, ice-sheet thickness and divide migration, and a linear problem to infer an improved depth-age scale for ice cores. Both methods make use of Frequentist statistics.

1.4 Applications

In this thesis, I use synthetic data resembling Antarctic records to demonstrate the ability of ice-flow modeling to assist dating techniques. Antarctic ice cores present tremendous dating challenges. In general, Antarctica has lower temperatures and accumulation rates compared with Greenland, and cores can be dated farther back in time (currently to 800 ka BP). However, low accumulation rates translate to thinner annual layers within the ice sheet, and those layers are more difficult to count using Electrical Conductivity Measurement (ECM), Dielectric Profiling (DEP) and seasonal variation in electrical properties and chemistry in the ice.

I demonstrate a self-consistent approach using synthetic data similar to those expected for WAIS divide, including accumulation and temperature histories and depth-age data. The WAIS divide site has a high accumulation rate, and therefore the promise of a high-resolution ice-core chronology. A good WAIS chronology will provide a timeline on which to compare WAIS with comparable ice-core records, such as GISP2 in Greenland.

1.5 Limitations

The goal of this work is to incorporate several previously distinct approaches to determine the past accumulation rate and ice dynamics (ice thickness and divide position), into a self-consistent model. We seek to incorporate the best information for dating ice cores, including both the chemical record in the ice and the atmospheric-gas record in the trapped gas bubbles. There are several limitations to this approach.

(1) Data are limited. Although we use synthetic data here, there are limitations in the quantity and uncertainty of data. Radar data along flow lines do not always exist. Geothermal measurements, crucial for accurate heat-transfer calculation, are sparse at best.

(2) We are limited in what we can infer from observations. In the linear inverse problem

to determine the depth-age relationship for ice cores, we cannot solve for both the past ice dynamics and accumulation rate. If we know one, we can solve for the other.
(3) Incomplete or inadequate ice-flow physics can be a limitation. For example, ice-flow models that do not incorporate the crystal-fabric orientation can produce incorrect strain rates and velocities for ice that exhibits strong directional effects.
(4) Computational resources are limited. In particular, in nonlinear inverse problems, the forward problem must run many times to make updates to the estimates for the parameters for which we are solving.

1.6 Outlook

The Intergovernmental Panel on Climate Change (IPCC) report [*Solomon et al.*, 2007] outlined the significant changes in the cryosphere, including ice-sheet extent; thickness and flow; glacier mass balance; and declining sea-ice extent in the Arctic. While observations of ice loss from mountain glaciers and ice sheets bring chilling realizations of social and political importance, the technological revolution has ushered in advances in computational resources and created new data-collection techniques. For example, new laser gas analyzers are capable of making measurements along cores rapidly at high temporal resolution. Progress in computational resources is allowing greater numerical modeling capabilities. This work provides the proof of concept that ice sheets can be treated as a physical system, where we can learn simultaneously about initial conditions, boundary conditions and ice-flow physics while improving the ice-core chronology. This work paves a direction for future studies, modeling multiple ice-sheet processes simultaneously in order to get the most benefit out of limited observations and computational resources. The self-consistent method is more than the sum of its parts and can be a useful tool to glean the most information from valuable ice-penetrating radar isochrones and ice-core records.

Chapter 2

DETERMINING ICE CORE DEPTH-AGE RELATIONSHIPS FROM SPARSE DATA USING INVERSE METHODS

This chapter is soon to be submitted for publication. My co-authors are Edwin Waddington, Howard Conway, Edward Brook and Loyce Adams. The idea and initial method for dating ice cores from sparse data using an inverse approach was presented at the IGS Milano Conference [*Waddington et al.*, 2003]. I wrote the text and developed the numerical software presented here. All of the coauthors have edited the entire manuscript.

Ice cores are often dated at only a sparse number of discrete depths; a robust scheme is needed to determine the depth-age relationship between sparse data. Here we investigate different interpolation schemes using sparse synthetic depth-age data. Piece-wise linear, exact-fit spline, and smoothing spline schemes introduce non-physical results when inferring histories of ice dynamics and accumulation. Sparse age-depth data are best interpolated using a physically-based ice-flow model and inverse methods. An accumulation-rate history can be determined if the history of ice dynamics (divide migration and thickness change), is known. Even if the histories of ice dynamics and accumulation can not be separated, depth-age relationships determined with this method are robust.

2.1 Introduction

2.1.1 Dating ice cores

Depth-age relationships measured in ice sheets today contain information about past climate (accumulation and temperature) and ice dynamics (changes in ice-sheet thickness and divide location). Chronologies for ice cores are typically established by measuring physical, chemical and electrical properties of ice and trapped gases. Near the surface, layers can often be resolved annually by measuring physical and chemical properties of the ice. At greater depths where annual layers are too thin to resolve, age indicators such as volcanic layers, trapped gases, and are typically sparsely distributed, and have uncertainty associated with their age. A robust scheme is needed to fit the depth-age relationship between sparse data. Here we generate synthetic sparse data and investigate different interpolation and curve-fitting schemes.

There exists several methods for determining values between data points. All these methods put a curve through or near the data points, and then evaluate the curve at the points of interest. One strategy is to select the curve to be a piece-wise linear or a cubic spline interpolation that goes exactly through the data points. Alternately, we can select the curve of a particular form (for example, the best line or the best quadratic or cubic polynomial) in the least-squares sense. This best-fit curve will not necessarily go through any of the data, but instead it will minimize the misfit to the data (the sum of the squares of the differences between the data and the curve over all the data points). More advanced techniques select a curve that balances the misfit to the data with the smoothness of the curve. The inverse method presented in this work is a curve-fitting method that incorporates physics of ice deformation.

2.1.2 Synthetic depth-age data

We generate a synthetic depth-age relationship using an ice-flow model to calculate a depth profile of layer thickness in units of m a^{-1}. The thickness of an annual layer $\lambda[z(A)]$ of age A at depth z, depends on the ice-equivalent annual accumulation rate $\dot{b}(A)$ at the time of deposition, and a thinning function $\Lambda(A)$, which accounts for the cumulative vertical strain

on the layer $\epsilon(A) = \frac{\dot{b}(A)-\lambda[z(A)]}{\dot{b}(A)}$, that is:

$$\Lambda = 1 - \epsilon(A) = \frac{\lambda[z(A)]}{\dot{b}(A)}. \tag{2.1}$$

The thinning function varies from Λ=1 at the surface where no deformation has occurred, to Λ=0 at the bed in the absence of melting. We calculate the thinning function using a 1-D ice-flow model [*Dansgaard and Johnsen*, 1969]. A 1-D model allows us to include transients in accumulation and ice dynamics without high computational requirements of more complex models. The model does not explicitly account for variations in ice temperature and related variations in flow. For this synthetic example we assume the ice is frozen at the bed; there is no basal sliding or melting. For application to polar sites, basal sliding and melting could be incorporated into the ice dynamics algorithm. The focus of this work is not the details of the ice-flow model, but rather the development of a robust method to determine the ice-core depth-age relationship.

In the Dansgaard-Johnsen model [*Dansgaard and Johnsen*, 1969], ice dynamics are represented by time variations in ice thickness $H(t)$ and parameter $h(t)$, both measured from the bed. From the surface to the kink height h, the vertical strain rate is uniform; from h to the bed, the vertical strain rate decreases linearly to zero. The kink height h varies from $h = 0$ for an ice sheet undergoing plug flow, to h=0.25H for flank sites, to h=0.7H at ice divides [*Nereson et al.*, 1998]. Transients in both ice dynamics and accumulation rate $\dot{b}(A)$ are easily incorporated into the model. Particles are tracked from the current depths in the ice core back in time to the ice-sheet surface to determine their initial thickness. The non-dimensional thinning function in Equation (2.1) is evaluated for each depth.

Rearranging Equation 2.1, the thickness of an annual layer of age A at depth z is

$$\lambda[z(A)] = \Lambda(A)\dot{b}(A). \tag{2.2}$$

Equation (2.2) shows that multiple pairs of $\Lambda(A)$ and $\dot{b}(A)$ can produce the same $\lambda[z(A)]$; additional information is needed to separate the individual contributions.

We generate synthetic data that have similar (but not identical) characteristics to those measured on the Siple Dome ice core in West Antarctica, where layers were resolved annually from 8.3ka BP to present [*Taylor et al.*, 2004]. From 97.6ka to 8.3ka BP measurements

derived from methane and atmospheric $\delta^{18}O$ of O_2 tie points to GISP2 were used to date the core [*Brook et al.*, 2005]. Figure 2.1 shows a synthetic depth-age relationship generated with constant (0.12 m a^{-1}) accumulation rate, constant ice thickness, constant divide location. In order to simulate data typically available from ice cores, we decimate these synthetic data so that the resolution is annual from 8.3 ka BP to present, and 27 irregularly spaced ages between 97.6ka and 8.3ka BP. We use synthetic rather than measured data because they allow *a priori* knowledge of the histories of accumulation rate and ice dynamics, which enables assessment of the performance of the interpolation and curve-fitting schemes.

2.1.3 Dating uncertainty

Uncertainty in dating ice cores comes from uncertainty in age and depth of layers. Depth uncertainty arises from errors when piecing sections of the core together to estimate the total length. Age uncertainty comes from analytical error, uncertainty in the gas-age ice-age offset (delta-age) and error in assigning control point-ages based on other ice-core records. We assume depth uncertainty is small, and age uncertainty (assumed to be σ_A 2%) dominates. In Section 2.5 we explore uncertainty values of 1%, 2% and 5% of the age. The inverse approach described in Section 2.3.1 is set up more naturally in terms of depth uncertainty σ_z. Figure 2.3 shows that age uncertainty can be transformed into depth uncertainty using the local slope of the depth-age relationship. That is:

$$\sigma_z = \frac{dz}{dA}\sigma_A \tag{2.3}$$

Uncertainty in depth can be included by combining it with the transformed age uncertainty in quadrature.

We add red noise scaled by the age uncertainty to the synthetic data in order to simulate uncertainties in ice-core data, while maintaining full knowledge of the inherent assumptions and uncertainty. Red noise arises from layer-counting biases and from cumulative random age errors. Other uncertainty comes from using different methods of layer counting. For example the upper 100 m of Siple Dome was dated using borehole optical stratigraphy, visual stratigraphy and electrical stratigraphy [*Hawley et al.*, 2003, Figure 3], which resulted in

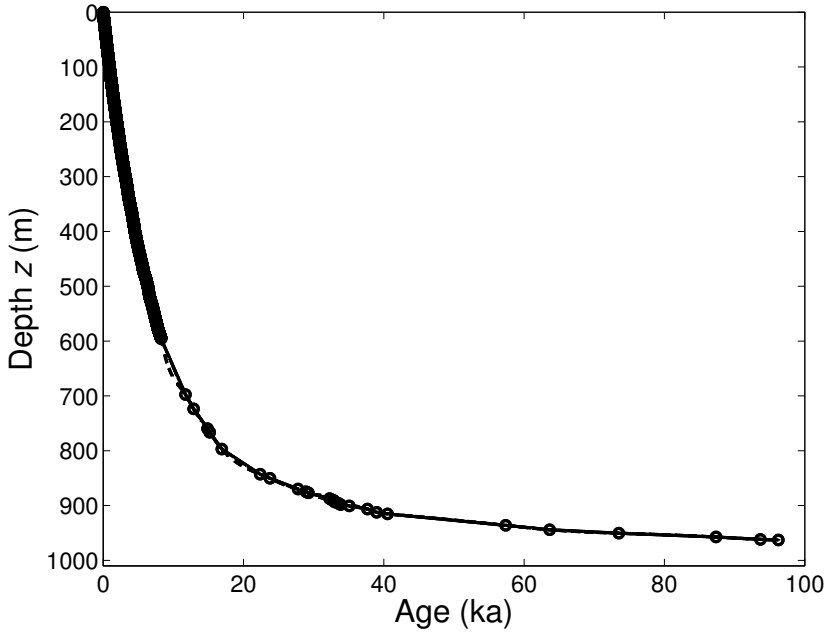

Figure 2.1: Linear (solid), spline(thick dashed) interpolations and smoothing spline (thin dased) curve fit are shown for synthetic depth-age data (circles). The inferred depth-age (dash-dot) is plotted as well. At this scale, all schemes appear to be adequate.

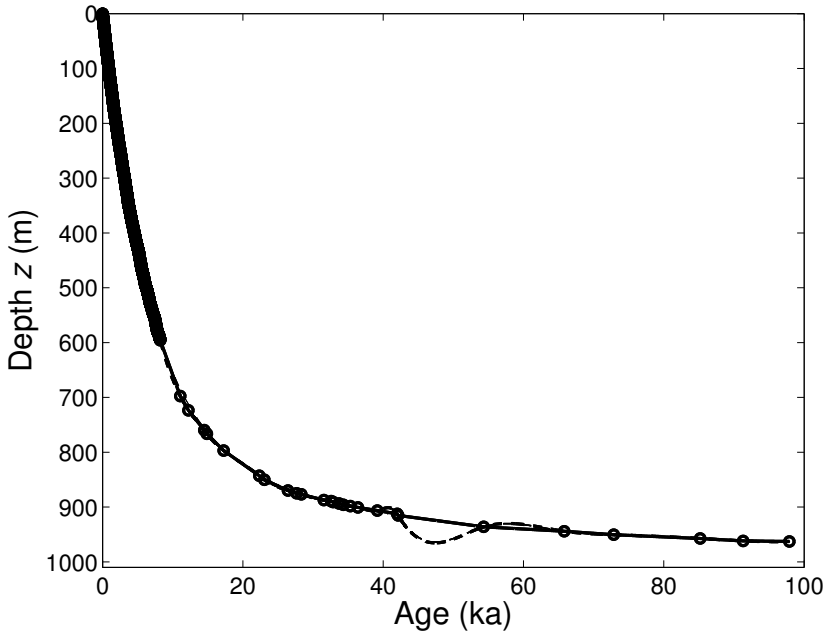

Figure 2.2: Linear (solid), spline(dashed) interpolations and smoothing spline (thin dashed) curve fit are shown for synthetic depth-age data (circles). The synthetic depth-age data have a different realization of the noise than Figure 2.1. The inferred depth-age (dash-dot) is plotted as well. Both the spline and smoothing spline schemes show large deviations from 60-40 ka.

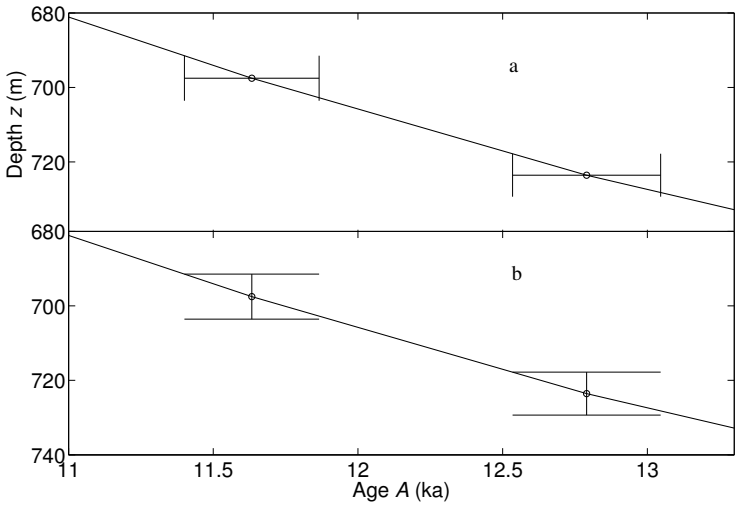

Figure 2.3: (a) An enlarged portion of the depth-age profile (Figure 2.1a) shows the uncertainty in age of two of the depth-age data. (b) The uncertainty in age can be expressed instead as an equivalent uncertainty in depth when the age uncertainty is multiplied by the depth-age slope (Equation 2.3). The uncertainties are equivalent.

three slightly different depth-age relationships. The differences are considered to be red rather than white noise, because it has persistence. Details of our prescribed red noise series are described in Appendix B.

2.2 Non-physical interpolation and curve-fitting schemes

We demonstrate the limitations of using interpolation and curve fitting schemes to determine the depth-age relationship between sparse data. We examine three schemes: linear, exact-fit spline, and a smoothing spline, which unlike the first two schemes, is not required to exactly fit each of the sparse data points. The interpolations and curve-fitting schemes have a smaller temporal spacing than the sparse ages A.

Linear and exact-fit spline interpolations between the sparse points (Figure 2.1) are difficult to distinguish by eye. One problem is over-fitting the data. Both the linear and exact-fit spline interpolations go through each depth-age exactly, and do not account for uncertainty. When a data set includes uncertainty, a good interpolation should not necessarily go through every data point. A smoothing spline is a curve-fitting scheme used to

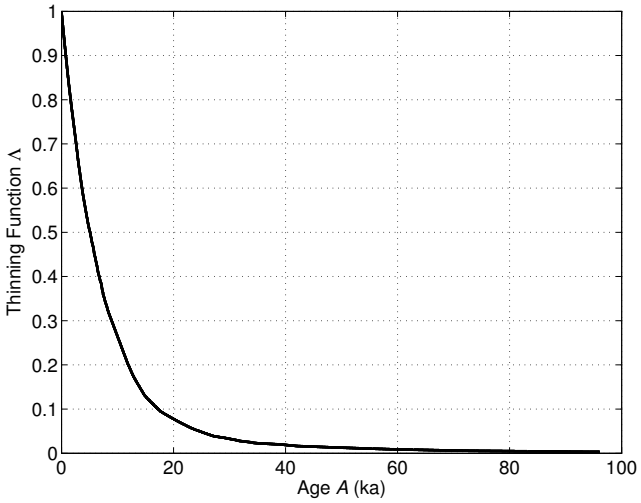

Figure 2.4: Thinning function $\Lambda(A)$ for ice flow with constant ice-sheet thickness and accumulation rate, and no divide migration.

fit noisy data. Similar to an exact-fit spline, a smoothing spline curve fit is not physically based, but it is not required to exactly fit each data point. We adopt a smoothing spline algorithm [*Hutchinson and de Hoog*, 1985] that uses a trade-off parameter to determine the balance between the data-model misfit and the second derivative of the depth-age fit. When we consider different realizations for the noise, as in Figure 2.2, we find the interpolations and smooth spline can introduce unphysical errors to the depth-age interpolation. We show non-physcially based schemes to fit noisy data, including linear and spline interpolations and smoothing spline curve fit, are not reliable at recovering the accumulation rate. A physically based method is necessary.

For the depth-age interpolations, we use the following procedure.

1) The thinning function Λ is calculated from the strain $\epsilon(A)$ from a flow model (Figure 2.4). This is the same thinning function used to generate the data.

2) Linear and exact-fit spline interpolations are applied to the sparse depth-age data.

3) The annual-layer thickness $\lambda(A)$ is determined from the slope, dz/dA of the depth-age interpolation.

4) The accumulation-rate history $\dot{b}(A)$ is determined from Equation (2.2).

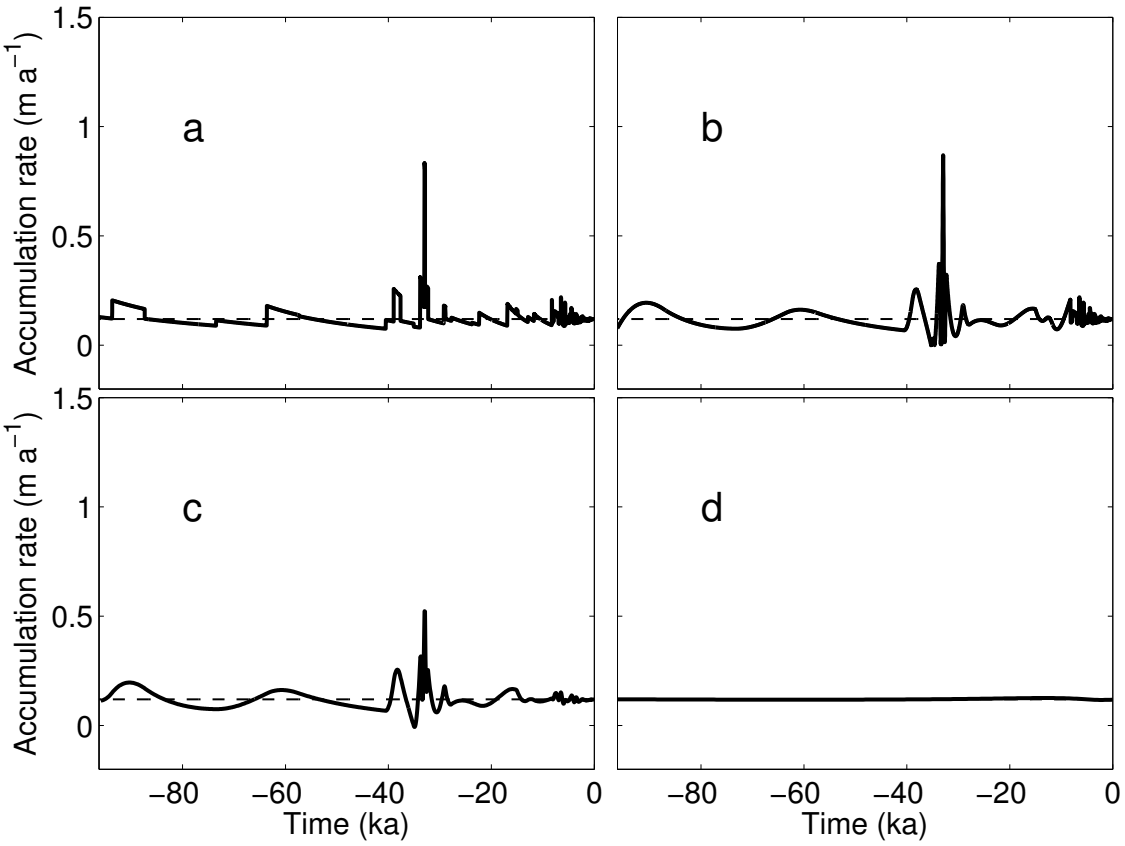

Figure 2.5: Accumulation-rate histories inferred from (a) linear, (b) exact-fit spline interpolations and (c) smoothing spline curve fit (bold, solid). The accumulation rate inferred from the inverse solution (d, bold solid) is near the constant 0.12 m a^{-1} (dashed) used to generate the sparse data. The 1-σ standard deviation (thin, solid) is indistinguishable from the inferred accumulation-rate history.

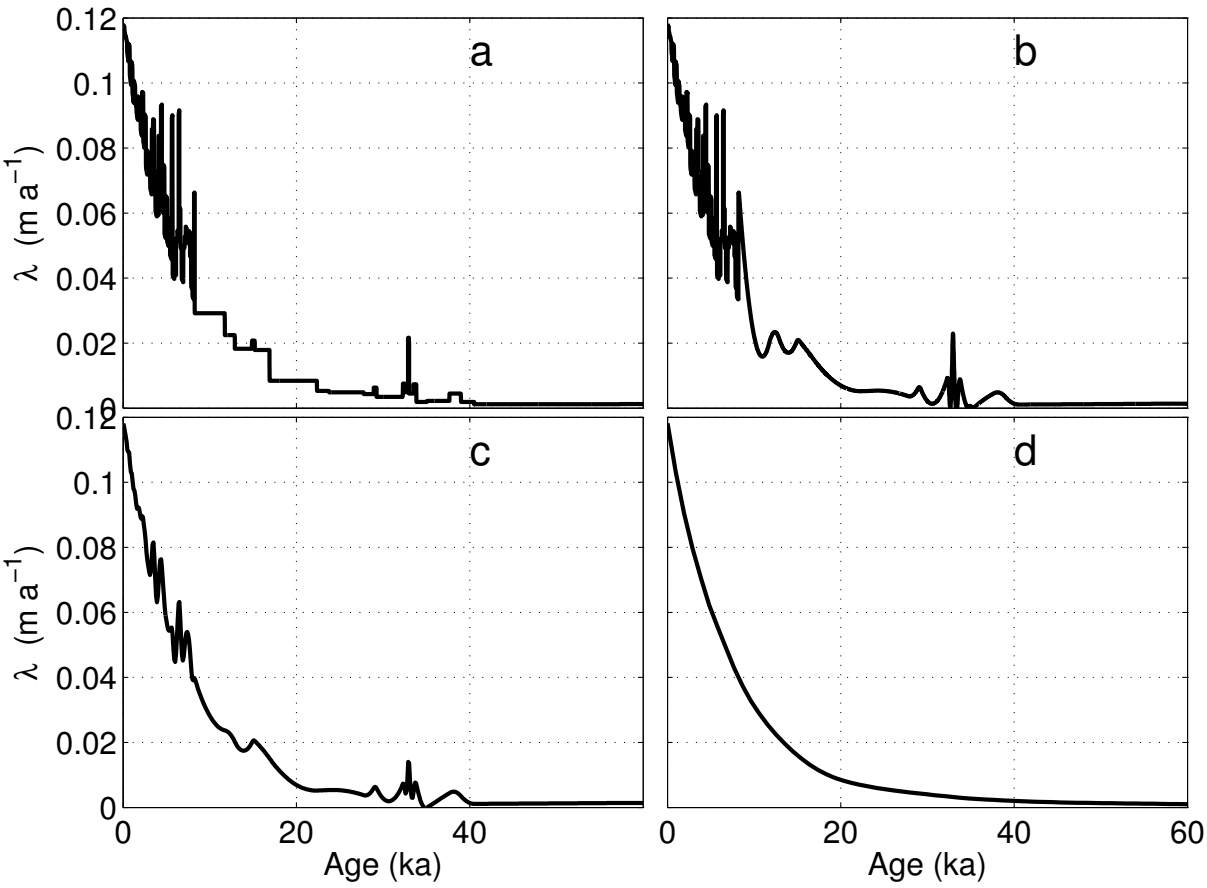

Figure 2.6: Annual-layer thickness $\lambda[z(A)]$ inferred from (a) linear and (b) exact-fit spline interpolations, and (c) smoothing spline curve fit show structures that are artifacts of a bad method. The layer thickness inferred from the inverse solution (d) matches the expected profile for steady-state dynamics. The age is shown from 60 ka to present to highlight differences in the layer thicknesses. Layer thicknesses for ice older than 60 ka are less than 0.005 m.

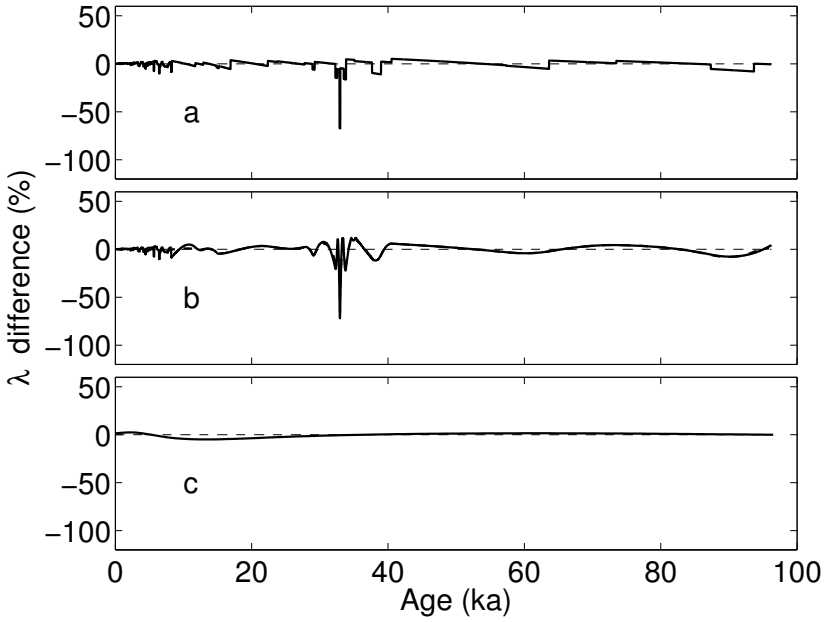

Figure 2.7: The percent difference in the (a) linear, (b) spline (solid line) and smoothing spline (dashed line), and (c) inferred layer thickness and the true layer thickness. Red noise (realization 1 of 3) is added to the synthetic data where the uncertainty is 2% of the age. The zero line (thin dashed line) is shown for reference. The maximum absolute differences in the linear, spline, and smoothing spline are 67.4%, 71.9% and 39%; and the maximum absolute difference in the inverse method is 4.9%.

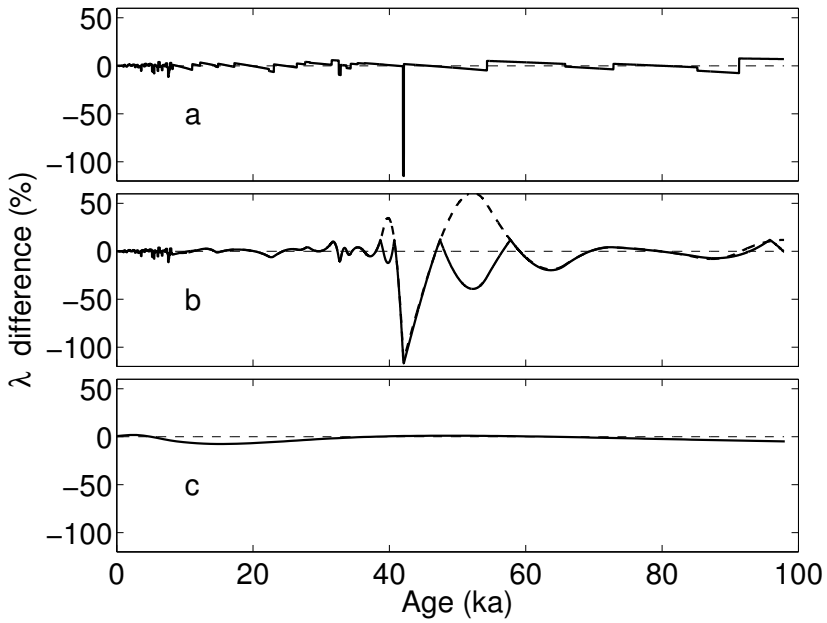

Figure 2.8: The percent difference in the (a) linear, (b) spline (solid) and smoothing spline (dashed line), and (c) inferred layer thickness and the true layer thickness. Red noise (realization 2 of 3) is added to the synthetic data where the uncertainty is 2% of the age. The zero line (thin dashed line) is shown for reference. The maximum absolute differences in the linear, spline, and smoothing spline are 114.9%, 116.8% and 112.4%; and the maximum absolute difference in the inverse method is 7.5%.

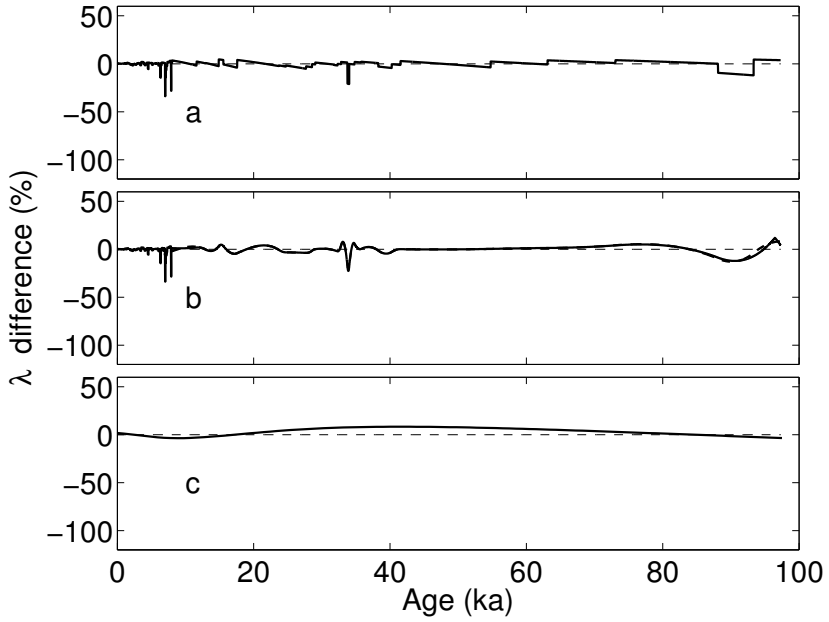

Figure 2.9: The percent difference in the (a) linear, (b) spline (solid line) and smoothing spline (bold dashed line), and (c) inferred layer thickness and the true layer thickness. Red noise (realization 3 of 3) is added to the synthetic data where the uncertainty is 2% of the age. The zero line (thin dashed line) is shown for reference. The maximum absolute differences in the linear, spline, and smoothing spline are 33.8%, 33.8% and 20.8%; and the maximum absolute difference in the inverse method is 12%.

Using the linear and exact-fit spline interpolations, we infer the accumulation-rate histories shown in Figure 2.5. The accumulation rate should be equal to the constant value 0.12 m a^{-1} ice equivalent that we used to create the steady-state sparse depth-age data. The inferred accumulation-rate histories deviates from the expected constant value as a result of an inappropriate interpolation. In the linear depth-age interpolations, the slope is constant between consecutive data points, so that all annual layers between two consecutive data points are assigned the same layer thickness (Figure 2.6). When layer thickness is invariant with depth, higher accumulation rate toward the older node is necessary to compensate for the additional thinning from ice dynamics (expressed through the thinning function) to achieve the same layer thickness. This results in the saw-tooth accumulation-rate history in Figure 2.5a.

Over time intervals where data are sparse (100ka to 40ka BP), the accumulation rate recovered by the smoothing spline is similar to the exact-fit spline (Figure 2.5), because no trade-off is required in the data misfit to achieve a smooth fit. From 40ka to present, the accumulation rate inferred from the smoothing spline differs from the exact fit spline, because the smoothing spline makes a trade-off to avoid fitting the data exactly.

The accumulation-rate histories inferred from linear and exact-fit spline interpolations fail to recover the constant accumulation rate. These interpolations have two problems: they over-fit the data and they are not physically based. Next we investigate the over-fitting problem.

The percent difference between the inferred layer thickness and true layer thickness is shown in Figures 2.7-2.9 for 3 synthetic data sets with different realizations of the noise, with the same age uncertainty (2%). The different noise realizations of the data create variation in the inferred layer thicknesses, with maximum absolute differences from 20.8% to 116.8% of the true layer thickness. However, the inferred solution is robust in determining an accurate layer thickness, between 4.9% to 12% of the true layer thickness. From three realizations of the data we find the inverse approach provides an improved estimate of the true layer thickness over linear, spline and smoothing spline schemes. From these three realizations we find motivation for the inverse approach.

2.3 Inverse approach

2.3.1 A physically based strategy

The inverse approach, consisting of a forward problem and an inverse problem, is designed to determine unknown parameters, boundary conditions, and initial conditions from data [*Aster et al.*, 2005; *Menke*, 1989; *Parker*, 1994; *Hansen*, 1998]. Here we adopt the convention that bold, upper-case letters are matrix operators, and bold, lower-case letters are vectors. The forward algorithm, represented by $\hat{\mathbf{G}}$, makes predictions of observable data quantities $\hat{\mathbf{d}}$ based on appropriate physics, where the hat represents non-dimensionalized variables. The model $\hat{\mathbf{m}}$ is the non-dimensional vector for which we are solving in the inverse problem and it can consist of coefficients, boundary conditions and initial conditions. For a linear forward problem,

$$\hat{\mathbf{d}} = \hat{\mathbf{G}}\hat{\mathbf{m}}. \tag{2.4}$$

The data uncertainty is represented by the covariance matrix $\mathbf{C}_d$. Without knowledge of whether the data are independent or not, we assume that the errors are independent and normally distributed, such that the data have a covariance matrix $\mathbf{C}_d$ with the squared standard deviations $\sigma^2_{z_j}$ from Equation (2.3) in the jth position on the diagonal. The matrix $\mathbf{G}$ and data $\mathbf{d}$ are scaled by the uncertainty,

$$\mathbf{G} = \mathbf{C}_d^{-1/2}\hat{\mathbf{G}}, \text{ and } \mathbf{d} = \mathbf{C}_d^{-1/2}\hat{\mathbf{d}}. \tag{2.5}$$

Now the inverse equation is both non-dimensionalized and scaled by the uncertainty and we can solve for the non-dimensional model $\hat{\mathbf{m}} = \mathbf{m}$,

$$\mathbf{d} = \mathbf{G}\mathbf{m}. \tag{2.6}$$

The inverse problem infers non-dimensional, unknown model parameters in the vector $\mathbf{m}$ based on the mismatch between the data $\mathbf{d}$ and the forward model prediction $\mathbf{G}_{q\times n}\mathbf{m}_{n\times 1}$. We represent the inferred model by $n-1$ piecewise-linear segments m_k, where k ranges from 1 to n. The data is d_j, where j ranges from 1 to q.

The methodology for this depth-age curve-fitting scheme calls for two inverse problems. In the first problem we determine a smoothly varying thinning function, where the thinning

function is known only at the ages where there are data. The second inverse problem requires the thinning function at model nodes to infer the accumulation-rate history.

2.3.2 Forward problems

Two distinct forward problems are required to solve for the depth-age solution. The first forward problem determines the thinning function at age nodes A and the second forward problem determines depths z based on the thinning function and accumulation-rate histories.

The first forward problem determines the thinning function at age nodes A. The matrix $\mathbf{G}$ is composed of n columns corresponding to basis functions Φ_k where k ranges from 1 to n, so that $\mathbf{G}_{jk} = \Phi_k(A_j)$. The thinning function at the data ages $\Lambda(A)$ is evaluated from model age nodes $\Lambda(a)$,

$$\Lambda(A) = \sum_{k=1}^{n} \Lambda(a_k)\Phi_k(A). \tag{2.7}$$

The basis functions $\Phi_k(A)$ are the piecewise linear functions chosen to be 1 at a_k and 0 at a_j for $j \neq k$. We can evaluate Equation (2.7) for any data age A and if we set $A = a_j$, then we reproduce $\Lambda(a_j)$. If A falls between age nodes a_i and a_{i+1}, then $\Phi_i(A)$ and $\Phi_{i+1}(A)$ sum to unity. Equation (2.7) interpolates $\Lambda(A)$ using the neighboring $\Lambda(a_i)$ and $\Lambda(a_{i+1})$ values.

The second forward problem computes depths for ice of given ages from specified accumulation-rate histories and thinning functions (incorporating ice-sheet thickness and divide-migration histories). The height, y, ranges from 0 at the bed, to the ice-sheet thickness H at the surface. The difference between $H(A)$ and $y(A)$ is the depth z of a particle of age A,

$$z(A) = H(A) - y(A) = \int_0^A \Lambda(a)\dot{b}(a)da, \tag{2.8}$$

which is given by summing up thicknesses of the younger overlying annual layers.

2.3.3 Inverse problems

Two inverse problems are performed. The first infers a smooth thinning function $\Lambda(a)$ at model age nodes. $\Lambda(A)$ is known where there are depth-age data from particle tracking (described in Section 1.2). We find a smoothest thinning function at the model nodes. The second inverse problem uses the thinning function at model ages a to infer the accumulation

rate $\dot{b}$ so that Equation (2.8) is a good fit to the data depth $z = H - y(A)$. For both inverse problems the procedure is the same, which is finding the smoothest model that fits the data well. The steps for the linear inverse procedure used for the two inverse problems are shown in Appendix C. It is possible to instead solve for $H(t)$ or $h(t)/H(t)$ instead of $\dot{b}(A)$, but it would be a non-linear problem that adds addition complication in the inverse procedure.

The forward problems in Section 2.3.2 are both mixed determined [*Menke*, 1989, p. 50], where the model is overdetermined corresponding with the annual layer counting portion of the ice core record, and the model is is underdetermined corresponding with the sparse depth-age data from other techniques including control-point dating.

Equation (2.6) cannot be solved directly, since $\mathbf{G}$ is underdetermined, or rank deficient, hence the inverse of $\mathbf{G}$ does not exist, and we cannot compute $\mathbf{m}$ as,

$$\mathbf{m} = \mathbf{G}^{-1}\mathbf{d}. \tag{2.9}$$

The matrix $\mathbf{G}$ is also ill conditioned, meaning that a small perturbation in the data $\mathbf{d}$ can result in a large change in the model $\mathbf{m}$. Because $\mathbf{G}$ is an underdetermined and poorly conditioned problem, it is not appropriate to use normal equations for least squares,

$$\mathbf{m} = (\mathbf{G}^T\mathbf{G})^{-1}\mathbf{G}^T\mathbf{d}, \tag{2.10}$$

since there is no unique solution and the matrix $\mathbf{G}^T\mathbf{G}$ is even more poorly conditioned than $\mathbf{G}$ and its inverse may not exist. Problems arise with stability and accuracy of the solution when taking the inverse of ill-conditioned matrices. See Appendix D for more discussion. The Singular Value Decomposition (SVD) is a better approach than normal equations; however, the SVD finds a unique solution through filtering out singular values. This option does not allow for adding knowledge about the problem to guide the best solution.

To set up a well-conditioned problem with a unique solution we use regularization, which lends *a priori* information about the nature of the expected solution. We expect $\mathbf{m}$ is the smoothest solution with the smallest second derivative that still fits the data $\mathbf{d}$ at a level consistent with its uncertainties. This approach is called a second-order Tikhonov regularization [*Phillips*, 1962; *Tikhonov*, 1963]. For equally-spaced model ages a, we find

the second-derivative roughening matrix operator $\mathbf{L}$,

$$\mathbf{L} = \begin{bmatrix} 1 & -2 & 1 & & & & & \\ & 1 & -2 & 1 & & & & \\ & & & ... & & & & \\ & & & & 1 & -2 & 1 & \\ & & & & & 1 & -2 & 1 \end{bmatrix}. \tag{2.11}$$

The semi norm $||\mathbf{Lm}||_2^2$ is given by

$$||\mathbf{Lm}||_2^2 = \mathbf{m}^T(\mathbf{L}^T\mathbf{L})\mathbf{m}. \tag{2.12}$$

We note a few interesting features of the second derivative operator $\mathbf{L}$, including scaling and boundary conditions. A second-derivative operator usually includes a scalar $1/\Delta t^2$, however, this is not required since the scalar becomes incorporated in the trade-off parameter ν in Equation (2.15). The second derivative matrix $\mathbf{L}_{n-2\times n}$ is without boundary conditions and the number of rows is two less than the number of columns. It has rank $n-2$, with a 2-dimensional null space. It is important that the null space of $\mathbf{L}$ does not overlap with the null space of $\mathbf{G}$ to ensure a unique solution to Equation (2.16). To test this, we find the product of $\mathbf{G}$ with two vectors from the null space of $\mathbf{L}$, $\mathbf{l}_1$ and $\mathbf{l}_2$. If products of $\mathbf{Gl}_1$ and $\mathbf{Gl}_2$ are not zero the null spaces of $\mathbf{L}$ and $\mathbf{G}$ do not overlap.

How much smoothness is necessary? A balance between the model smoothness and data misfit is achieved through the trade-off parameter ν. A perfectly smooth model with a constant slope and zero second derivative may result in a poor model-data misfit. If ν is too small, the model is too rough, and if ν is too big, the model has a large residual. How well the model prediction of the data fits the observed data $\mathbf{d}$ is measured by the non-dimensional residual $\mathbf{r}$, a vector of length q. The residual $\mathbf{r}$,

$$\mathbf{r} = \mathbf{d} - \mathbf{Gm}, \tag{2.13}$$

is the misfit between each element of data $\mathbf{d}$ and prediction from the model $\mathbf{Gm}$. Because the problem has been scaled by the covariance matrix, the elements of the residual vector measure the misfit in the standard deviations between the modeled depth and the data depth.

The goodness of fit of the model-data mismatch is evaluated using the residual norm scalar, which is the sum of squared residuals. The residual norm,

$$||\mathbf{Gm} - \mathbf{d}||_2^2 = \sum_{i=1}^{q}((\mathbf{Gm})_i - \mathbf{d}_i)^2 = \mathbf{r}^T\mathbf{r}. \tag{2.14}$$

With measurements for the model smoothness in the semi norm and the data misfit in the residual norm, we vary the value of ν to select the $\mathbf{m}$ that minimizes the function,

$$||\mathbf{Gm} - \mathbf{d}||_2^2 + \nu||\mathbf{Lm}||_2^2, \tag{2.15}$$

which is equivalent to minimizing,

$$\left\| \begin{bmatrix} \mathbf{G} \\ \nu\mathbf{L} \end{bmatrix} \mathbf{m} - \begin{bmatrix} \mathbf{d} \\ \mathbf{0} \end{bmatrix} \right\|_2. \tag{2.16}$$

Solving the least-squares equations for the model with the trade-off parameter scaling the smoothness gives,

$$\mathbf{m} = \left([\mathbf{G}^T \nu\mathbf{L}^T] \begin{bmatrix} \mathbf{G} \\ \nu\mathbf{L} \end{bmatrix} \right)^{-1} [\mathbf{G}^T \nu\mathbf{L}^T] \begin{bmatrix} \mathbf{d} \\ \mathbf{0} \end{bmatrix}. \tag{2.17}$$

Rearranging Equation (2.17), the normal equations for the model $\mathbf{m}$ using a generalized inverse $\mathbf{G}^{\#}$ are,

$$\mathbf{m} = (\mathbf{G}^T\mathbf{G} + \nu^2\mathbf{L}^T\mathbf{L})^{-1}\mathbf{G}^T\mathbf{d} = \mathbf{G}^{\#}\mathbf{d}. \tag{2.18}$$

We solve the system of equations using the Singular Value Decomposition (SVD),

$$\mathbf{m} = \mathbf{G}_{svd}^{\#}\mathbf{d} = \mathbf{G}^{\#}\mathbf{d}, \tag{2.19}$$

where $\mathbf{G}_{svd}^{\#}$ is more efficient and numerically accurate than $\mathbf{G}^{\#}$. See Appendix D for motivation for the SVD method over normal equations and Appendix E for a detailed description of the SVD formulation.

The trade-off parameter ν is determined using an L-curve plot [*Hansen*, 1992; *Aster et al.*, 2005], where the residual norm and roughness semi norm are shown for a range of ν values. The best ν value comes from the 'corner' of the L-shaped plot. In Figure 2.10, the trade-off parameter ν and the amount of smoothing increases from left to right.

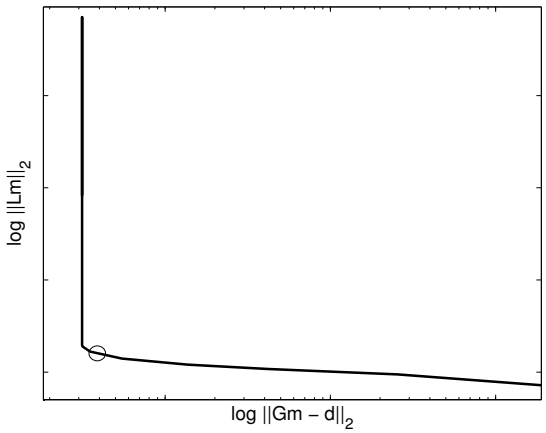

Figure 2.10: The L-curve is parameterized by ν. The circle shows the preferred value of the Lagrange multiplier ν is selected in the 'corner' of the L-curve.

By stepping through values of ν, and viewing the changes in the model resolution and uncertainty (described in the following Section) the best trade-off parameter is selected.

An alternate way to choose the trade-off parameter is to find ν where the residual norm is equal to the squared tolerance, $||r||_2^2 = T^2$ [*Parker*, 1994]. The tolerance T is defined in terms of the number of data q,

$$T = q^{-1/2}\Big[1 - \frac{1}{4q} - \frac{1}{32q^2} + O(q^{-3})\Big]. \tag{2.20}$$

We find that determining ν such that the residual norm equals the tolerance $||r||_2^2 = T^2$ yields model solutions that are close to those where ν is determined using the L-curve; however, we find the model solutions with the L-curve are better at finding the balance between the residual norm and semi norm.

The model uncertainty and resolution trade off with a change in ν; the uncertainty increases and the resolution decreases as ν increases. The more smoothing increases the uncertainty in the model solution. Details of how the model uncertainty and resolution are determined are given in Appendix F.

As a consequence of the smoothness assumption, the inferred model may not capture abrupt changes that are real. If rapid changes in the accumulation rate are inferred despite

the smoothness criterion, then we have confidence that the structure is real. Furthermore, it is likely that the change in accumulation rate was larger than our inferred accumulation-rate change, because the inferred accumulation rate is smoothed in time in our inverse approach. If we have prior knowledge that accumulation rate changed rapidly at a time of abrupt climate change, the smoothness criterion could be relaxed for that time interval.

A benefit of the inverse method is that the resolution and uncertainty of the model solution can be estimated before data have been collected, since these properties are dependent on the spatial and temporal geometry of the problem in the formulation of $\mathbf{G}$, rather than the actual data $\mathbf{d}$. This ability to project the resolution of the expected solution can guide the spatial and temporal sampling of the data.

2.4 Steady-state results

2.4.1 Known ice dynamics

We test the inverse method described in Section 3 with the same depth-age data used to illustrate the poor interpolations in Section 2. Two inverse problems are performed, first to solve for the thinning function, and then to determine the accumulation-rate history. The inferred accumulation-rate history should match the steady-state value used to generate the data.

The resolution is a way to quantify the bias in the generalized inverse $\mathbf{G}^{\#}$, described in detail in Appendix F. The resolution matrix, $\mathbf{R}_m$ is composed of columns of resolution kernels, which reflect how well individual model parameters are recovered (similar to model-resolving functions [*Waddington et al.*, 2007]). Resolution kernels are equivalent to the result of spike model tests (that is, finding the model vector that is the product of the resolution matrix with a spike model $\mathbf{m}_{spike}$, a vector of zeros with a single element equal to 1). The resolution kernels are diagnostic of how well a given model parameter is recovered, where perfect resolution would result in a delta function. In practice, good resolution depends on how much regularization, in this case smoothing, is needed. If there is no regularization, the resolution matrix is an identity matrix and resolution kernels for the kth column are zero except for a 1 at the kth entry. When regularization is necessary, the resolution kernels have

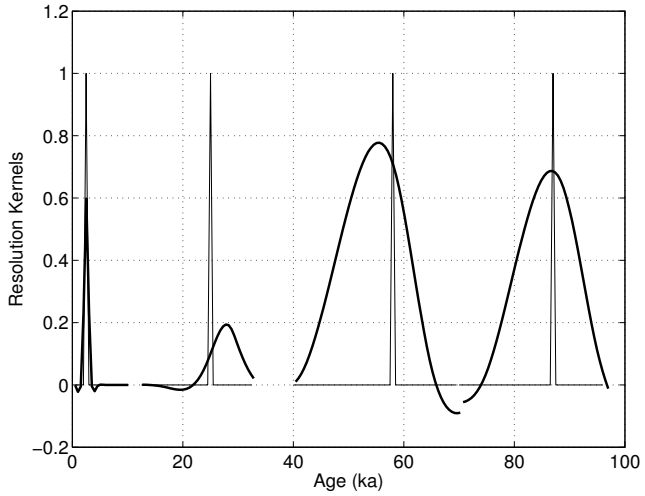

Figure 2.11: Spike model test results for the thinning function inverse problem for 4 model parameters, corresponding to model ages 5 ka, 25 ka, 58 ka and 89 ka.

a magnitude smaller than 1 and span a larger number of model parameters to achieve the smooth model solution. The resolution kernels for the thinning-function inverse problem are shown in Figure 2.11. Spike models and resolution kernels are shown for model nodes corresponding to ages 5 ka, 25 ka, 58 ka and 89 ka. The width of the resolution kernel indicates how many neighboring model nodes affect the solution for the particular model nodes of interest. Model nodes at 25 ka, 58 ka and 89 ka require smoothing over a greater number of neighbors than at 5 ka. This is because there are annually spaced data at 5 ka and data are sparse before 8 ka. The smoothness constraint in the inverse problem is important for constraining solutions where data are sparse.

In the second inverse problem, the accumulation-rate solution is inferred. Compared to the bad interpolations from Section 2, this accumulation-rate history is more similar to the constant accumulation rate of 0.12 m a^{-1} used to generate the data, shown in Figure 2.5. The inferred accumulation rate is not expected to be exactly the same as the prescribed accumulation rate because noise was added to the data. The deviation from the true value in the inverse solution is also due to forcing the residual norm to form a minimum with the semi norm in Equation 2.15 and in the L-curve. The depth residual in Figure 2.13 reflects

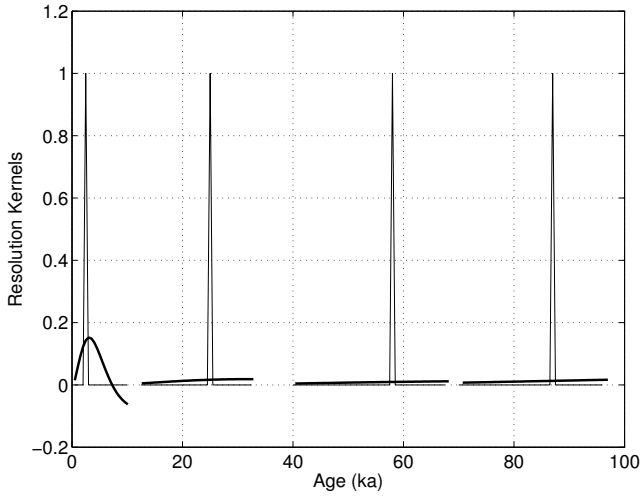

Figure 2.12: Spike model test results for the accumulation inverse problem for 4 model parameters, corresponding to 5 ka, 25 ka, 58 ka and 89 ka.

the mismatch in the modeled and observed depth. The residual illustrates the depth-age profile does not fit perfectly through the data.

The resolution kernels for the second inverse problem at ages 5 ka, 25 ka, 58 ka and 89 ka in Figure 2.12 show more regularization was necessary when selecting the best value for ν in the L-curve. The resolution is poorer in this case, however, when comparing the expected model $\mathbf{m}_E$ to the true model $\mathbf{m}_{true}$, we find the difference is less than 1% and negligible.

Although the depth-age relationship inferred from the inverse approach is difficult to distinguish by eye from those derived using non-physical interpolation and curve-fitting schemes (Figure 2.1), the inverse approach is an improvement because it is able to recover the accumulation rate (Figure 2.5) used to generate the data and the layer thicknesses. Figure 2.6d shows the inferred layer thickness.

The accumulation model and age-integrated thinning functions form a linear combination to estimate the depth. The resolution matrix shows how each model parameter is dependent upon the younger accumulation. The resolution kernels in Figure 2.12 for ages 5 ka, 25 ka, 58 ka and 89 ka, show how these model nodes require more regularization,

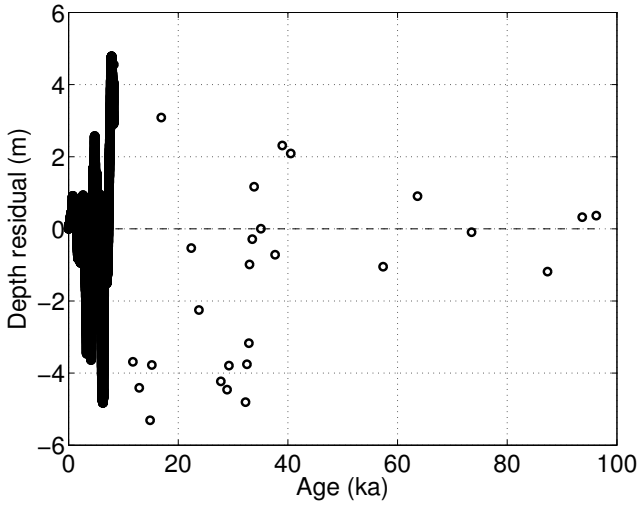

Figure 2.13: The residual for the modeled and data depths for steady state dynamics.

and therefore have smoother resolution kernels than those for the thinning-function inverse problem.

The resolution kernels are not shown for subsequent inverse problems in the following Sections; however the 1-σ standard deviation is shown in the model solutions for accumulation rate.

Resolution tests for all of the inverse problems produced an expected model $\mathbf{m}_E$ less than 1% difference than the unity $\mathbf{m}_{true}$.

2.4.2 Unknown ice dynamics

In Sections 2.2 through 2.4.1 we assumed that the ice dynamics, represented by the thinning function Λ (including ice-sheet thickness H and divide position kink height h/H), were known, in addition to the depth-age data and the uncertainty. Now we consider the more realistic case when magnitude and duration of changes in H and h/H are not known. In the model, this is represented by a thinning function Λ that is generated from an ice flow model for a different divide position represented by the non-dimensional kink height h/H, or a different thickness history $H(t)$. Often the magnitude and timing of changes in ice-sheet thickness and divide position are not well known. East Antarctica is thought to

have changed little in thickness since the LGM, while West Antarctica has thinned since the LGM, although the timing and magnitude of this thinning are not well constrained. Often the timing and magnitude of changes in the ice dynamics in polar ice sheets are not well known. By assuming different ice dynamics in the forward problem than those used to generate the data, we are using a physically-based thinning function, but a thinning function that is incorrect for the site.

In this Section we use the same synthetic depth-age data from Section 2, which was created using the kink height of $h = 0.25H$ (representing flank flow) and ice-sheet thickness that was constant at $H = 1000$m. The age uncertainty was 2%. In this experiment the thinning function $\Lambda(A)$ used as the data $\mathbf{d}$ in the thinning-function inverse problem does not represent the ice dynamics used to generate the data. To show that the ice dynamics including divide migration and the thickness histories (in the thinning function) are unknown, we carry out two numerical experiments, where the (1) divide-position history and (2) ice-sheet thickness history are unknown.

For the first experiment, the kink height $h = 0.7H$, associated with divide flow, is used in the forward problem to generate the thinning function. An inverse solution for a smooth thinning function is determined. A second inverse solution for the inferred accumulation rate (Figure 2.14) is found to be greater than the constant 0.12 m a^{-1} used to generate the data. Because the forward-problem physics assume divide-flow dynamics, a regime with little vertical and horizontal velocity, the thinning function is smaller than for flank-flow dynamics. Smaller thinning functions reflect greater thinning from ice flow. For case (1) the inferred accumulation-rate history is larger to make up for the smaller thinning function.

The depth-age relationship from the unknown ice dynamics is indistinguishable by eye from the depth-age relationship from the known dynamics and poor interpolations. We show the residual mismatches of the model and data depths in Figure 2.15. These residuals show a mismatch in depth that is similar to the previous experiment in Section 2.4.1 where the ice dynamics are known. This is to say that with or without knowledge of the ice dynamics, we can determine a robust depth-age relationship. To additionally determine the proper accumulation rate, we must have knowledge of the ice dynamics.

The inverse method provides a robust way to estimate the layer thicknesses without

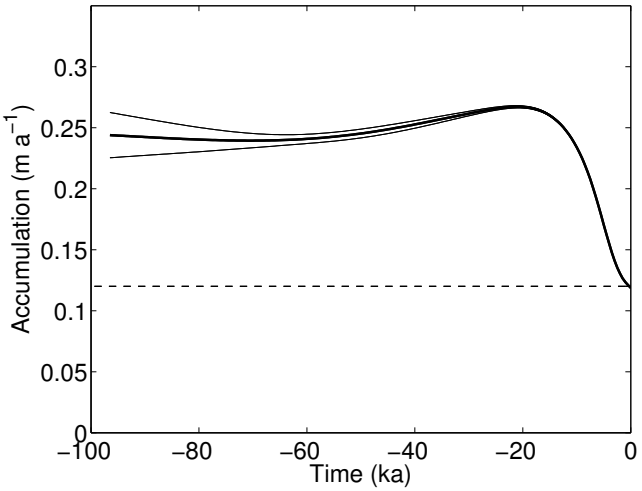

Figure 2.14: The different ice dynamics in the forward problem than that used to create the synthetic depth-age data results in an inferred accumulation-rate history (bold, solid) with 1-σ uncertainty (thin, solid) that is greater than the 0.12 m a^{-1} prescribed accumulation rate (dashed). To infer the proper accumulation history we need to know the ice-dynamics history.

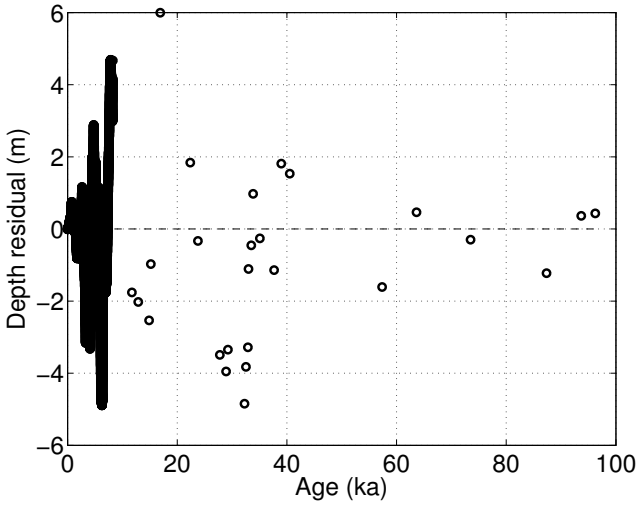

Figure 2.15: The misfit between the inferred and data depths for steady state dynamics with the wrong h/H.

knowledge of past ice dynamics, including possible timing and magnitude of past ice dynamics changes.

Taking the results from this Section with the previous Section, we see approximately the same layer thicknesses and depth-age relationship is found, with two different pairs of accumulation rate and thinning function (ice dynamics). That is two pairs (or more) of accumulation and thinning function histories can reproduce essentially the same depth-age relationship.

In case (2), which is not shown, the ice-sheet thickness H of 1500m is used in the forward problem to generate the thinning function. The increase in thickness produces a smaller thinning function than the case of $H = 1000$m, requiring a greater inferred accumulation rate to match the same depth-age data.

When the dynamics histories are not known, it is not possible to recover an accurate accumulation-rate history. The robust result from this experiment is the depth-age profile, which is the same with or without knowing the unique pair of accumulation rate and ice dynamics history. Since the depth predicted by the forward problem $\mathbf{G}^{\#}\mathbf{m}$ matches the data depth $\mathbf{d}$, balanced with the model smoothness, we find that the depth-age profile is nearly indistinguishable as Section 2.2.

To summarize Section 4, the depth-age relationship from the inverse problem is pinned to the depth-age data. When the dynamics in the forward problem are the true dynamics, the accumulation-rate history may be recovered. If the forward problem dynamics differ from the true dynamics, then the accumulation-rate history will be too high or too low to accommodate the difference while matching the proper depth-age data.

2.5 Transient dynamics

The transient forward problem in the inverse approach is explored in a similar way to recover the thinning function and accumulation-rate. Synthetic data are generated using transient accumulation rate, uniform ice-sheet thickness $H = 1000$m and uniform kink height $h = 0.25H$, representing a flank position. The depth-age points are not the same as Sections 1-4. The ages are the same but the ice is at different depths.

Similar to the steady-state examples, smoothly varying thinning functions are deter-

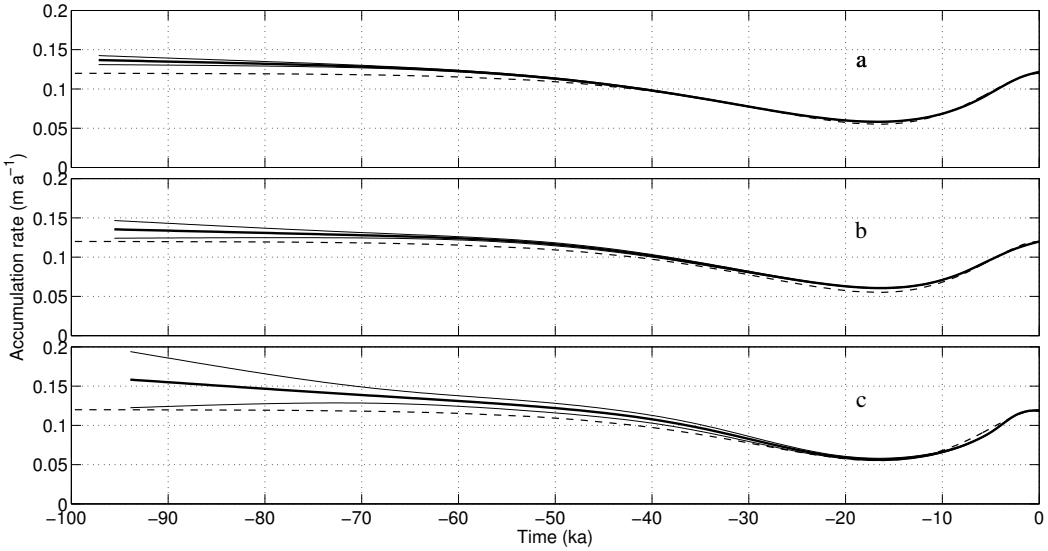

Figure 2.16: Synthetic (dashed) and modeled (solid, thick) accumulation-rate histories for age uncertainties of 1%(a), 2% (b), and 5% (c). The 1-σ_m uncertainties (solid thin) for the inferred accumulation rate are shown as well.

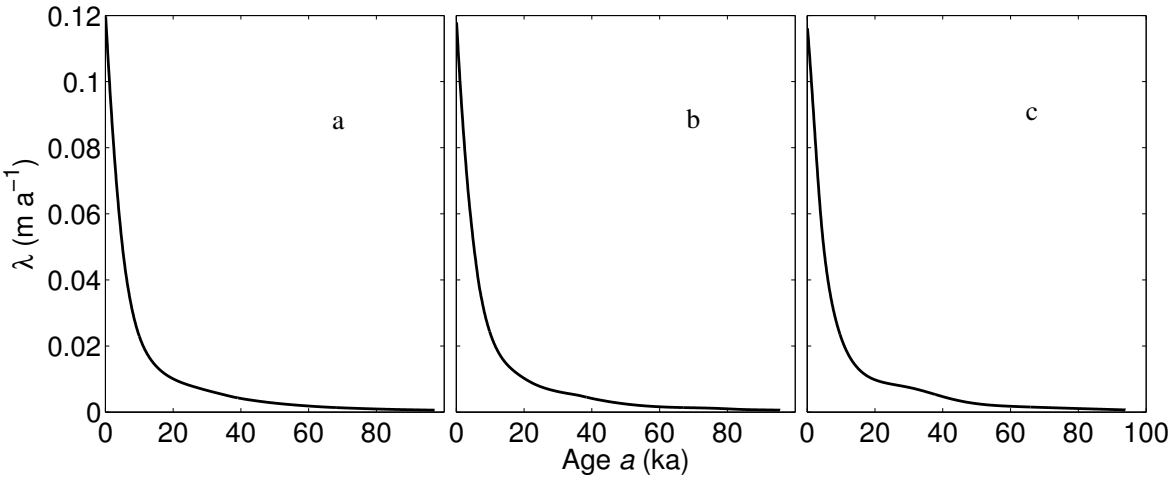

Figure 2.17: Annual layer thickness with Age a. Age uncertainty is 1%(a), 2%(b), and 5%(c).

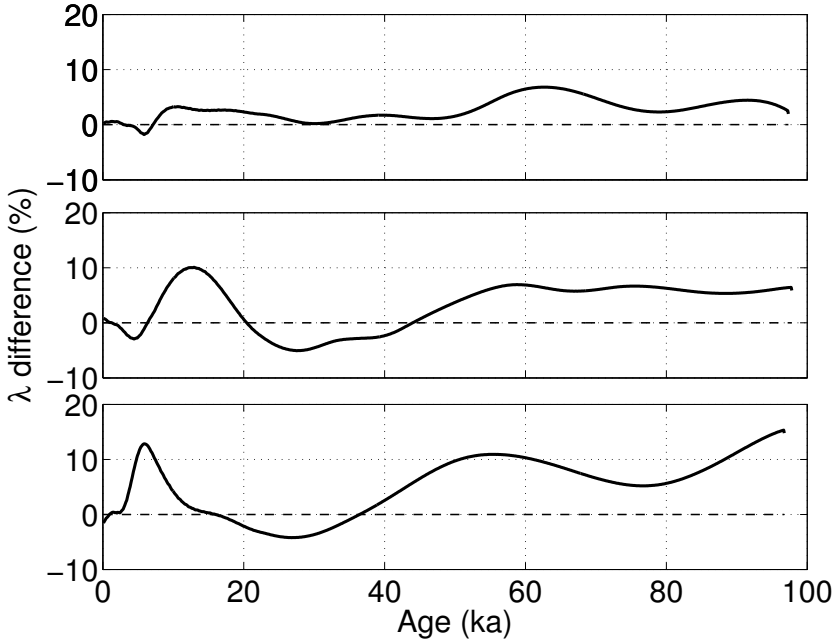

Figure 2.18: The percent difference between the inferred layer thickness and true layer thickness for 1%(a), 2%(b), and 5%(c).

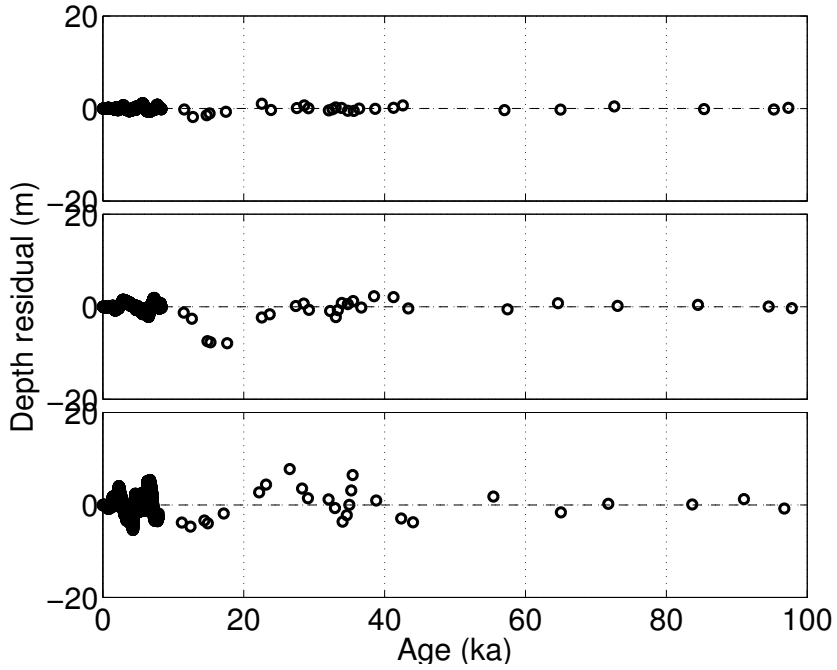

Figure 2.19: Depth residuals are shown for 1%(a), 2%(b), and 5%(c) uncertainty.

mined from the sparse thinning-functions $\mathbf{\Lambda}(A)$. Next the accumulation-rate history, layer thicknesses and depth-age relationships are inferred for age uncertainties of 1%, 2%, and 5%.

The accumulation-rate history in Figure 2.16 shows the recovery of the accumulation-rate history prescribed to generate the data. The inferred accumulation-rate history best recovers the original accumulation-rate history when the age uncertainty is 1%. The recovery of the accumulation-rate history is poorest when the age uncertainty is 5%. The inferred depth-age data fits the data the closest for the 1% uncertainty. With the 5% age uncertainty, the inferred depth has the greatest residual mismatches.

The layer thicknesses inferred in the inverse approach (Figure 2.17) for 1%, 2% and 5% age uncertainty are very similar. The layer thicknesses for 2% and 5% show deviations from the 1% uncertainty. The inferred layer thicknesses reflect that it is important to have a low uncertainty on the data.

Figure 2.18 shows the percent difference between the inferred and true layer thickness.

Residuals from the model-data difference (rescaled by the uncertainty) in Figure 2.19 show larger misfits in the residual for the data with greater age uncertainty.

In this Section, different uncertainties on the depth-age data allow the inverse method to recover the prescribed accumulation rate to varying satisfaction. When the age uncertainty is 5% of the age, the inferred accumulation-rate history, layer thickness, and the depth-age profile is not as well constrained by the data. However, all of the uncertainties considered, including 1%, 2%, and 5% uncertainties allow for both a good depth-age profile and a recover the accumulation-rate history reasonably well.

2.6 Summary and discussion

We show that linear and spline and smoothing-spline schemes are not sufficient to recover histories of accumulation rate and ice dynamics from sparsely dated ice cores. These are methods to fit noisy data, but contain no physics and cannot recover the accumulation-rate used to generate the synthetic data even when the ice dynamics history is fully known, motivation is provided for a physically based inverse method. In Section 4.1, we show with a steady-state inverse problem the near-constant accumulation can be recovered using the

inverse approach. The depth-age relationship from the inverse approach matches the data well, but not exactly, since the data contain noise.

Often past ice sheet dynamics, including thickness and divide position, are not known. In Section 4, the ice dynamics used to generate the thinning function in the forward problem differs from the ice dynamics used to generate the data. The accumulation-rate history cannot be recovered when the ice dynamics are not known. The robust result is that a depth-age relationship can be achieved regardless of the wrong dynamics.

Transient dynamics, including temporal variations in ice-divide position and ice-sheet thickness, are explored in Section 5. We attempt to recover the accumulation history for different age uncertainties of 1%,2% and 5%, and we show that the inferred depth-age relationship is affected more by the uncertainty in depth-age data, rather than uncertainty in the thinning function. If past ice dynamics are known, reasonable accumulation-rate histories are inferred and a physically based depth-age profile is produced. Even with sparse data, we can achieve a robust depth-age relationship for uncertainties as high as 5% of the age.

The curve-fitting inverse method presented here is applied to synthetic data and it is particularly useful for Antarctic ice cores, which often present a challenge to date due to low accumulation-rate and windy conditions that can mix or remove annual layers. Antarctic accumulation and temperature reconstructions show smooth temporal variations, which allows us to apply a smoothness criterion in the inverse method. A robust method for fitting depth-ages for ice cores, even when past ice dynamics are not known, provides an important contribution for best interpreting paleoclimate records from ice cores.

Chapter 3

FIRN DENSIFICATION: A COUPLED THERMOMECHANICAL MODEL WITH GRAIN GROWTH

We have developed a 1-d Lagrangian firn model to track distinct layers of polar firn, coupling heat flow, grain growth and densification. Recent observations from firn cores show that layers vary seasonally in density, grain size and c-axis orientation, and initially high-density layers at the surface densify more slowly than initially low-density layers. Layers maintain distinct physical characteristics in addition to density through time and depth; however, current models account only for density. By accurately reconstructing firn-density evolution, our goal is to better estimate delta-age, the difference in ice age and gas age. Delta-age varies with climate and is a large source of uncertainty in dating ice cores and atmospheric gas records. Here we develop a model of the evolution of firn density profiles and delta-age histories through time with applications to polar ice cores including the WAIS divide ice core from West Antarctica.

3.1 Introduction

3.1.1 Background

Investigation of polar firn densification is important for several applications in glaciology. Mass-balance studies of ice sheets have significant uncertainty in estimating mass of polar firn when only the upper-surface elevation is known. In paleoclimate applications, atmospheric gas records from ice cores require a history of gas-age ice-age offset (delta-age) in order to assign a consistent chronology to both ice and gas. This work focuses on the paleoclimate application, to quantify delta-age through time. Ice takes decades to millennia to compact enough to trap atmospheric gas, and trapped gas is younger than the enclosing ice, often by an uncertain amount. Delta-age can be estimated with firn-compaction models to account for the age of the ice at the estimated depths for gas lock-in and bubble close-off.

Firn density increases with depth and time primarily as a function of temperature and overburden stress. The increase in accumulation rate increases densification of firn, by increasing the overburden load (vertical longitudinal stress). The densification of firn is often divided into three zones defined by densities of 550 kg m^{-3} and 830 kg m^{-3}. In zone 1 ($\rho < 550$ kg m^{-3}), firn experiences grain-boundary sliding until approximately 550 kg m^{-3}, corresponding to the effective maximum packing of spheres observed with a porosity of 40% [*Cuffey and Paterson*, 2010, p. 21]; however, the observed transition from zone 1 to zone 2 is not always at 550 kg m^{-3} [*Hörhold et al.*, 2011]. In zone 2, densification occurs through sintering. At bubble close-off density, gas bubbles are trapped and no longer communicate with the surface. In zone 3, deformation occurs through bubble compression until the density of ice is reached, at approximately 917 kg m^{-3}. The processes mentioned are the dominant processes; however these processes overlap and it cannot be ruled out that other processes are important and should be explicitly included in modeling.

3.1.2 Previous work

Schytt [1958] derived an empirical density-depth $\rho(z)$ relationship from observations:

$$\rho(z) = \rho_i(\rho_i - \rho_s)\exp(-z/z_p). \tag{3.1}$$

The density of ice is ρ_i and the surface density is ρ_s. The characteristic depth z_p is a site-dependent constant. The approximate value of the characteristic depth is $z_t/1.9$ where z_t is the depth of the firn-ice transition. Several values for z_p can be referenced [*Cuffey and Paterson*, 2010, p. 16].

Several firn-density models have been used to characterize the behavior of polar firn. *Herron and Langway* [1980] proposed a model of firn densification model that assumes the rate of densification changes at different critical densities:

$$D\rho/Dt = c_0(\rho_i - \rho) \qquad \rho <= 550 \text{ kg m}^{-3} \tag{3.2}$$

$$D\rho/Dt = c_1(\rho_i - \rho) \qquad \rho > 550 \text{ kg m}^{-3} \tag{3.3}$$

Herron and Langway [1980] do not define a coefficient for snow densities greater than the critical density of 830 kg m^{-3}. The coefficients c_0 and c_1 (units a^{-1}) in the Herron and Lanway model have an Arrhenius rate law including the temperature $T(K)$ and the gas constant R, 8.314 J mol^{-1}K^{-1},

$$c_0 = 11(\dot{b}_w)^a \exp\left[-\frac{10160}{RT}\right], \tag{3.4}$$

$$c_1 = 575(\dot{b}_w)^b \exp\left[-\frac{21400}{RT}\right]. \tag{3.5}$$

The activation-energy values for the 2 zones are 10160 mol J^{-1} and 21400 mol J^{-1}. The powers a and b are site-specific constants determined from the slope of the line formed by $\ln(\rho/(\rho_i - \rho))$ plotted as a function of the water-equivalent (w.e.) accumulation rate $\dot{b}_w$. The mean and standard deviation of a and b are 1.1±0.2 and 0.5±0.2. The coefficients 11 and 575 have units (a m^{-3})^a and (a m^{-3})^b.

Several modeling efforts have built upon the Herron and Langway approach. For example, *Barnola et al.* [1991] included effects of heat transport through the firn; *Li and Zwally* [2004] parameterized the model coefficients c_0 and c_1 based on studies of grain growth. *Helsen et al.* [2008] adjusted the *Li and Zwally* model coefficients c_0 and c_1 based on firn density observations.

Arthern et al. [2010] used Nabarro-Herring creep for firn densification incorporating an

improved grain-growth model [*Gow et al.*, 2004] for the coefficients c_0 and c_1,

$$c_0 = f_0 \exp\left[-\frac{E_c}{RT} + \frac{E_g}{RT_{av}} \right] \tag{3.6}$$

$$c_1 = f_1 \exp\left[-\frac{E_c}{RT} + \frac{E_g}{RT_{av}} \right] \tag{3.7}$$

The coefficients f_0 and f_1 of 0.3 a^{-1} and 0.7 a^{-1} were tuned to three Antarctic Peninsula sites and activation energies of creep E_c and grain growth E_g, 60 kJ mol^{-1} and 42 kJ mol^{-1} are derived from laboratory measurements [*Petrenko and Whitworth*, 1999] and tuned to the slope of crystal size and age [*Cuffey and Paterson*, 2010, p. 39-40]. *Arthern et al.* [2010] suggest that the activation energy from grain growth reduces the temperature sensitivity of the firn compaction for densities less than 550 kg m^{-3}.

It is a non-unique problem to determine activation energies and coefficients simultaneously. Using parameter estimation to solve for coefficients and the activation energy provides different solutions for the activation energy of the two zones than what is determined from laboratory measurements [*Arthern et al.*, 2010]. Therefore, we cannot rule out the possibility that other processes besides creep and grain growth are important. It is possible that these processes might vary between firn densification zones or in the entire firn column.

Other models have varied from the pioneering Herron and Langway style of modeling densification. *Spencer et al.* [2001] tuned five parameters for three zones of firn densification (15 parameters total), to 38 sites with known accumulation, density and temperature. The *Spencer et al.* [2001] model is valid within the limits its of calibration; however, it contains negative exponents on the stress terms, which is not physically meaningful. *Goujon et al.* [2003] developed a semi-empirical model with different physics for the three zones of densification. The model was applied to determine the lock-in age for Vostok and GISP2.

3.1.3 Density observations

Low-accumulation sites in interior Antarctica exhibit seasonal summer and winter layers, and high accumulation sites in Greenland show layering within the same storm. Recent observations from firn cores show that surface accumulation is not homogeneous, and instead

shows variation in density and grain size. Layers retain distinct characteristics from the surface throughout densification.

At the surface, summer layers are large-grained and have low density, while winter layers are small-grained and have higher density. Initially high-density fine-grained layers densify slower than initially low density course-grained layers [*Hörhold et al.*, 2011; *Freitag et al.*, 2004], potentially due to impurity content [Freitag, *in review*]. Initially high-density firn forms in the summer and initially low density firn forms in the winter and these layers can also have distinct c-axis orientations [*Fujita et al.*, 2009].

Between 600 kg m^{-3} and 650 kg m^{-3} the density variation crosses over between summer and winter layers, where initially low density layers become more dense than the initially high density layers. This cross-over in density is also a minimum in the density variability. There is initially a high variability at the surface, a minimum (600-650 kg m^{-3}), followed by a second maximum in variability, which differs among cores. Cores from higher accumulation-rate sites have a greater variability in the density at the firn-ice transition than cores from lower accumulation-rate sites.

3.1.4 Gas transport and observations

Firn is a permeable porous medium. There are three zones of gas transport, distinct from the three zones of firn densification in Section 3.1.3. The three zones of gas transport are (1) the convective zone, where air is well-mixed with the overlying atmosphere; (2) the diffusive zone where there is gravitational settling and diffusion driven by gradients in concentration and temperature; and (3) the non-diffusive zone, where air no longer diffuses. This is defined as the lock-in depth and the lock-in age is the difference in the ice-age and gas-age at the lock-in depth. The diffusive column height refers to the depth of the non-diffusive zone, at the top of zone 3. Current lock-in depths and ages in Table 3.1 for different cores reflect differences in site accumulation rate and annual-average temperature.

Measurements of noble gas and nitrogen isotope profiles in cores provide insight into the length of the diffusive column in the past, and can be used to help constrain models of the lock-in zone [*Goujon et al.*, 2003; *Schwander et al.*, 1997]. Trapped atmospheric δAr and

Table 3.1: Current lock-in values for some Greenland and Antarctic ice cores reflect dependence on accumulation rate and temperature.

Location (Reference)	Accumulation rate (m a^{-1} i.e.)	Temperature T_{av} °C	lock-in age (years)	lock-in depth (m)
GRIP [*Schwander et al.*, 1997]	0.23	-31.7	210	71
GISP2 [*Schwander et al.*, 1997]	0.248	-31.4	195	72
GISP2 [*Goujon et al.*, 2003]	0.248	-31.4	192	65
WSD [*Mischler et al.*, 2009]	0.22	-30	205	65.5
Vostok [*Goujon et al.*, 2003]	-	-57.4	3300	98

$\delta^{15}N$ reflect differences in $^{40}Ar/^{36}Ar$ and $^{15}N/^{14}N$ compared to laboratory standards. Nitrogen and noble-gas isotopes fractionate in response to thermal gradients and gravitation [*Severinghaus et al.*, 1998; *Severinghaus and Brook*, 1999]. The effect of temperature on fractionation is known from laboratory measurements. Gravitational fractionation occurs due to mass differences. By comparing values for $\delta^{40}Ar$ (or isotope ratios from other noble gases) and $\delta^{15}N$, the gravitational and thermal effects can be separated. The diffusive firn column height can be determined from the gravitational signal. Other noble gases are used to constrain the diffusive firn column, including Kr, which has a lower sensitivity to gravitational settling than Ar and offers an improved constraint over Ar on the gravitational and thermal effects [*Orsi*, 2011]. The diffusive firn column depth estimates provide no insight on the depth of the convective zone. The convective zone is typically assumed to be between 2 and 10 m.

It has been suggested [*Landais et al.*, 2006] that the non-diffusive zone is absent in low-accumulation sites, but only where strong firn layering occurs. However, other work [*Hörhold et al.*, 2011] shows that seasonal layering is present at low accumulation-rate sites. A separate study [*Buizert et al.*, 2011] suggests there is gas transport below the lock-in, in the non-diffusive zone.

3.2 Model method

3.2.1 Lagrangian framework

I have developed a densification model using a transient 1-d Lagrangian formulation. Previous work has implemented a Lagrangian reference frame [*Arthern et al.*, 2010; *Arthern and Wingham*, 1998, e.g.].

We use a coupled grain-growth and densification model [*Arthern et al.*, 2010, Equation B1] in a creep equation, relating the change in densification to grain size [*Coble*, 1970]. With each time step (greater or less than 1 year), a snow parcel is added to the top of the firn column and a parcel is removed from the bottom.

Firn temperature $T(z,t)$ and density $\rho(z,t)$ are coupled properties that vary with time and depth. Temperature evolution depends on density because thermal conductivity K and

specific heat c depend on density. The densification rate depends on temperature through the Arrhenius factor.

3.2.2 Densification

We use a coupled densification, grain-growth and heat-transfer system of equations [*Arthern et al.*, 2010, Equation (B1)], with Lagrangian densification rate is

$$\frac{D\rho}{Dt} = k_c(\rho_{ice} - \rho)\exp(-E_c/RT)\sigma/r^2. \tag{3.8}$$

The grain radius is r and overburden stress is σ.

The surface boundary condition $\rho(0,t)$ is either constant or parameterized based on temperature. A relationship was proposed [*Reeh et al.*, 2005], based on Greenland surface density ρ_s kg m^{-3} and surface temperature data T_s in Kelvin in a least-squares quadratic fit, to get

$$\rho_s = 625 + 18.7T_s + 0.293T_s^2. \tag{3.9}$$

The surface density from Equation (3.9) is shown in Figure 3.1 for temperatures ranging from -50 to 0 °C. The parameterization fails for temperatures colder than -32 °C, which is outside of the range of data used to calibrate the model. Other parameterizations [*Kaspers et al.*, 2004] are based on wind speed, accumulation rate, and surface temperature.

Any parameterization for the surface density should take site conditions into account. We use a constant surface density of 330 kg m^{-3}, but recognize that a more complex surface-density calibration could be used.

3.2.3 Heat transfer

Heat transfer is handled using an implicit finite-volume power-law scheme [*Patankar*, 1980]. The partial differential equation for temperature in the Lagrangian format is

$$\frac{DT}{Dt} = \frac{1}{\rho c}\frac{\partial}{\partial z}\left(k\frac{\partial T}{\partial z}\right). \tag{3.10}$$

The diffusion of heat with depth z is based on the thermal conductivity k and specific heat c in W m^{-1}K^{-1} which depends on temperature T. The thermal conductivity of ice k_{ice}

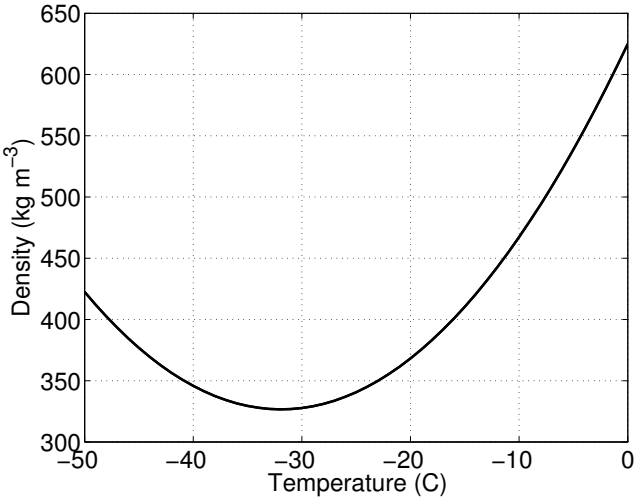

Figure 3.1: The surface density can be parameterized based on the surface temperature [*Reeh et al.*, 2005]. The surface densities for temperatures colder than -32 °C are unreliable and are outside of the calibration range for the model.

used by *Goujon et al.* [2003],

$$k_{ice} = 2.22(1 - 0.0067)T. \tag{3.11}$$

The thermal conductivity of the firn k_{firn} is based on k_{ice} and density ρ [*Schwander et al.*, 1997; *Goujon et al.*, 2003],

$$k_{firn} = k_{ice}\left(\frac{\rho}{\rho_{ice}}\right)^{2-0.5\rho/\rho_{ice}}. \tag{3.12}$$

The specific heat of the firn c_{firn} in units of J kg^{-1}K^{-1} is evaluated as a linear mixture of the specific heat of the air c_{air} and ice c_{ice},

$$c_{firn} = \left(\frac{\rho}{\rho_{ice}}\right)c_{ice} + \left(1 - \frac{\rho}{\rho_{ice}}\right)c_{air}. \tag{3.13}$$

The specific heat of ice depends on temperature [*Cuffey and Paterson*, 2010], through

$$c_{ice} = 152.5 + 7.122T. \tag{3.14}$$

The specific heat of air c_{air} is 10^{-3} J kg^{-1}K^{-1} at -50 °C. The specific heat of the firn is dominated by the specific heat of the ice; however, for completeness we incorporate in Equation 3.13 the specific heat of the air as well as ice.

The thermal diffusivity $\kappa = k/\rho c$, depends on the density ρ and specific heat c, in addition to the conductivity k. Inverse methods to determine thermal diffusivity from thermistor string data reveal that thermal properties exhibit great variation [*Sergienko et al.*, 2008, e.g.].

Thermal boundary conditions

The surface Dirichlet boundary condition to Equation (3.10) is prescribed from temperature reconstructions using profiles of water isotopes $\delta^{18}O$ and δH. Other methods for reconstructing surface boundary conditions come from borehole thermometry [*Cuffey and Clow*, 1997; *Dahl-Jensen et al.*, 1998]. The estimate of the geothermal flux is assigned as the bottom Neumann boundary condition in Equation (3.10).

Figure 3.2 shows the analytical solution for the decay with depth of seasonal surface temperatures [*Cuffey and Paterson*, 2010, p. 401-403, cf., e.g.]. The temperature $T(0,t)$ at the surface (depth $z = 0$) is

$$T(0,t) = T_{av} + A_T \cos(2\pi t). \tag{3.15}$$

Where the average surface temperature is T_{av}, the frequency ω is defined as cycles per time and thermal diffusivity is $\alpha = k/\rho c$. The amplitude of the seasonal signal is A_T, where the magnitude of the seasonal signal is $2A_T$. The analytical solution for the temperature with depth is

$$T(z,t) = T_{av} + A_T \exp(-z\sqrt{\pi\omega\alpha}) \cos(2\pi t - z\sqrt{\pi\omega\alpha_T})). \tag{3.16}$$

Thermal boundary conditions at the surface of the ice sheet are similar to a sine-wave temperature forcing. We integrate over a year the term $\exp(-E/RT)$ rather than using the average surface temperature T_{av} because warmer temperatures in summer months cause more rapid densification and grain growth than that captured by mean annual temperatures. Due to the Arrhenius-factor, the effective temperature T_{eff} at the site is greater than the average surface temperature T_{av}. At depth ($\geq$10m) T_{eff} is equivalent to the mean temperature since seasonal changes are no longer apparent. To determine the influence of

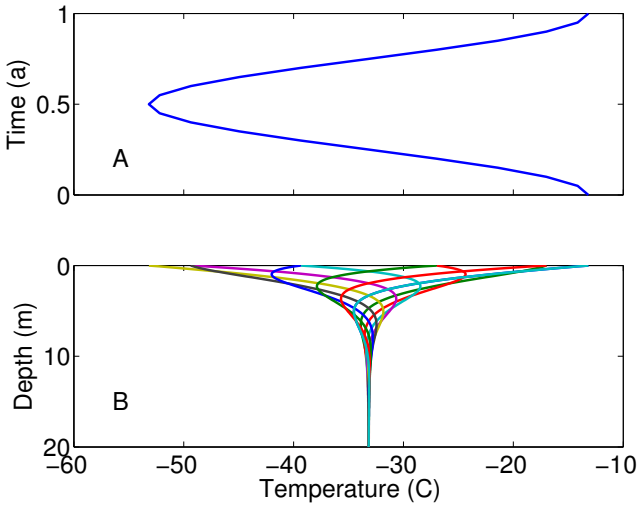

Figure 3.2: A) The surface temperature from Equation (3.15) with a 20K amplitude. B) An analytical solution in Equation (3.16) for the decay of seasonal surface temperatures with depth over the period of one year.

the seasonal signal, it is necessary to take time steps less than one year. For time steps greater than one year the effective temperature T_{eff} can be used. The effective temperature is solved from integrating the seasonal temperature cycle.

$$T_{eff} = -E_c / \left(R \ln\left(\frac{1}{t_a} \int_0^{t_a} \exp\left(-E/RT(t) \right) dt' \right) \right) \tag{3.17}$$

The activation energy E in Equation (3.17). We consider the activation energy for creep E_c and the activation energy from the sum of activation energies from creep and grain growth $E_c + E_g$. The activation energy is lower when including the activation energy from grain growth. Figure 3.3 shows that the effective surface temperature is $3K$ greater than the mean temperature when including grain growth. Without the activation energy from grain growth, the effective surface temperature is 10K greater than the mean temperature. Some firn models are tuned using the effective temperature [*Spencer et al.*, 2001] and other models [*Herron and Langway*, 1980, e.g.], use the average surface temperature.

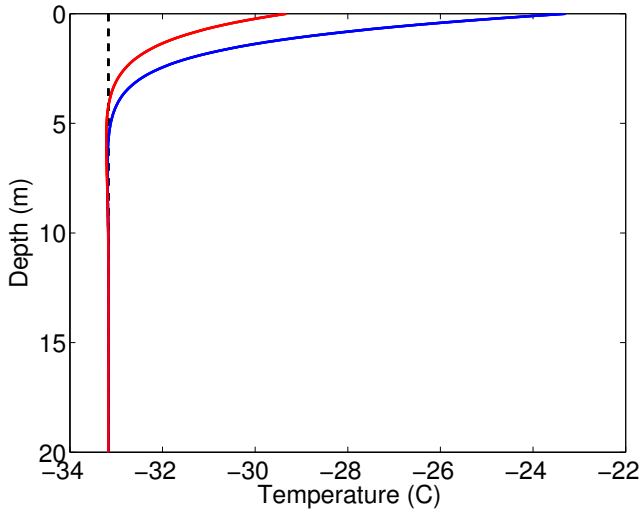

Figure 3.3: The effective temperature is determined for the time series of the surface temperature, as in Equation (3.17). The mean temperature is shown for reference (dashed black). The effective temperature (blue) is 10K greater at the surface for activation energy from creep alone. With the activation energy from grain growth and creep (red), the effective temperature is smaller, approximately 3C greater than the mean temperature.

3.2.4 Grain growth

The grain growth is modeled using the following relationship [*Gow et al.*, 2004],

$$\frac{Dr^2}{Dt} = k_g \exp(-E_g/RT). \tag{3.18}$$

The choice of grain-growth model is not the focus of this application and a different model could be used. More complex models include insolation and temperature gradients, which are important at the surface.

3.2.5 Deformation from ice flow

While we treat firn in 1-d, we include 2-d effects of horizontal extension and vertical compression of ice flow, even though this is a small effect.

The surface strain rate ϵ_{h0} is evaluated from the accumulation rate $\dot{b}_0$,

$$\epsilon_{h0} = \frac{n+2}{n+1}\frac{\dot{b}_0}{H_{ice}}. \tag{3.19}$$

The ice-equivalent ice-sheet thickness H_{ice} is corrected by the height of the air in the firn column h_{air},

$$H_{ice} = H - h_{air}. \tag{3.20}$$

The vertical velocity w_z is then evaluated for each time step

$$w_z = w_0 - \epsilon_{h0}(z_{fb} - z_{rock}) - \Big(\frac{\epsilon_{h0}}{n+2}\Big)H\bigg(\Big(1 - \frac{z_{fb}}{H_{ice}}\Big)^{n+2} - \Big(1 - \frac{z_{rock}}{H_{ice}}\Big)^{n+2}\bigg) \tag{3.21}$$

The vertical velocity calculation includes the vertical velocity w_0 at the bed, and at the bottom of the firn column z_{fb}. The bottom of the firn column in the Lagrangian reference system changes depending on the thickness of the firn column. The bed elevation z_{rock} is constant. The power n is 1 for firn, which behaves as a linear viscous material [*Alley*, 1992]. The power n is 3 for this model, since strain is driven by the ice below the firn.

The method for determining the vertical velocity used here assumes the ice sheet is a parallel-sided slab, and the $u(z)$ and $v(z)$ have the same shape function.

The updated base of the firn column z_{bf} is evaluated,

$$z_{bf+1} = z_{bf} + w_z\Big(\frac{\rho_{ice}}{\rho}\Big)\Delta t \tag{3.22}$$

The horizontal and vertical dimension of the boxes are updated to reflect the strain from flow.

3.2.6 Bubble close-off

The critical density of bubble close-off was suggested by *Herron and Langway* [1980] to be between 820 and 840 kg m^{-3}. More recently, the critical density is taken to be a constant, 815 kg m^{-3} [*Barnola et al.*, 1991]. The most common way to evaluate the critical density of bubble close-off is based on surface temperature T_s (K) and pore volume V_c (cm^3 g^{-1}) [*Martinerie et al.*, 1994]. Pore volume relates to the surface temperature,

$$V_c = (6.95 \times 10^{-4})T_s - 0.043. \tag{3.23}$$

The critical density ρ_c is empirically based on the pore volume [*Martinerie et al.*, 1992],

$$V_c = \frac{1}{\rho_c} + \frac{1}{\rho_{ice}}. \tag{3.24}$$

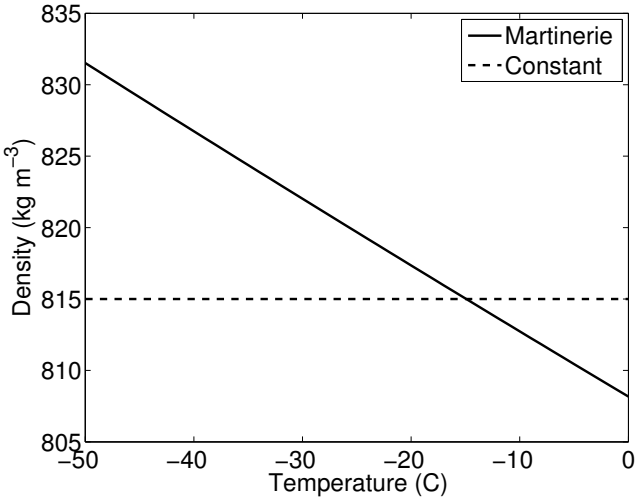

Figure 3.4: The critical density of bubble close-off is based on the surface temperature T_s [*Martinerie et al.*, 1994]. Other work uses a constant critical density of 815 kg m^{-3} [*Barnola et al.*, 1991].

In Equation (3.24) the units for ρ_c and ρ_{ice} are in units of cm^3 g^{-1}. We rearrange the equation and solve for ρ_c and convert the units to m^3 kg^{-1} by multiplying by a factor of 1000. The critical density ρ_c is shown in Figure 3.4 for a range of surface temperature from -50 °C to 0 °C. The critical density varies from greater that 830 kg m^{-3} to 808 kg m^{-3}, with greater critical densities for colder temperatures. Equations (3.23) and (3.24) are frequently used in firn models [*Arnaud et al.*, 2000; *Goujon et al.*, 2003], although, there is suggestion that variability in close-off depth is greater in warmer sites than in colder sites [*Hörhold et al.*, 2011]. This imples the the relationship between temperature and the critical density is more complex than the relationship in Equation (3.24).

Delta-age from the age of the ice at bubble close-off is the lower bound for the lock-in age. In some cases the lock-in depth coincides with the bubble close-off depth, assuming no non-diffusive zone is present.

3.2.7 Lock-in

Gas transport in firn is defined by three zones: the convective zone, diffusive zone and non-diffusive zone. The lock-in depth is defined as the bottom of the diffusive firn column.

Below the lock-in depth is the bubble close-off depth, where gases are trapped in bubbles in the ice. The lock-in delta-age is more useful than that at bubble close-off delta-age in adjusting ice and gas age records, because the lock-in zone is where air is first isolated from the atmosphere. The gas-age ice-age at bubble close-off is an over-estimate of the delta-age.

The porosity is defined based on the density:

$$\phi = (1 - \frac{\rho}{\rho_{ice}}) \tag{3.25}$$

The porosity is composed of open porosity ϕ_o, where gases diffuse and closed porosity ϕ_c, where gases are trapped in bubbles,

$$\phi = \phi_o + \phi_c. \tag{3.26}$$

The closed porosity ϕ_c is approximated based on the porosity and the pore volume P_c at close-off,

$$\phi_c = 0.37\phi(\phi/P_c)^{-7.6}. \tag{3.27}$$

The pore volume P_c at close-off is based on the volume V_c at close-off from Equation (3.23) and density at close-off ρ_c [*Martinerie et al.*, 1994],

$$P_c = 1 - \frac{\rho_c}{\rho_i} = \rho_c V_c. \tag{3.28}$$

The gas lock-in zone is at the bottom of the diffusive firn column. We assign the lock-in zone when the open porosity ϕ_o is 0.10 [*Orsi*, 2011]. The closed porosity is evaluated from the density of close-off ρ_c. A previous study has compared the closed porosity to density [*Schwander et al.*, 1993] and agrees with the relationship used in Equations (3.27) and (3.28) The total porosity ϕ is evaluated from the density using Equation (3.25).

We determine the open porosity using Equation (3.26). This method of assigning the lock-in depth and age based on the density is an approximation. We recognize the method of determining the diffusive firn column height is best replaced with a transient gas transport model that incorporates diffusion from gravitational settling, and thermal and concentration gradients. The model used here does not incorporate the effects of rapid temperature changes at the surface on gas transport in the firn.

Table 3.2: The lock-in open porosity values for one Greenland and two Antarctic ice cores. The lock-in open porosity is site dependent and based on firn-air measurements.

Ice core	Open porosity	Reference
WSD	0.10 ± 0.02	*Orsi* [2011]
GISP2	0.13	*Goujon et al.* [2003]
Vostok	0.21	*Goujon et al.* [2003]

3.3 Grain-size model

It is necessary to have a boundary condition and initial condition for the grain size r_s to use a Coble-type creep equation [*Coble*, 1970]. Because grain size measurements are scarce, we propose a method that relates the steady-state densification of firn with a transient model that includes grain size. The surface grain radius r_s can be determined by equating a steady-state model in Equations (3.2) and (3.3) [*Herron and Langway*, 1980; *Li and Zwally*, 2004; *Helsen et al.*, 2008] with a Coble creep equation [*Coble*, 1970], such as Equation (3.8).

Combining Equations (3.8) and (3.2), we solve for the grain size radius r_s,

$$r_0 = \frac{c^*}{k_c \exp(-E_c/RT)\sigma}. \tag{3.29}$$

Any of the steady-state type models, including Herron and Langway, Li and Zwally and Helsen, may be be used to determine c^*, where c^* is c_0 for $\rho <= 550$ kg m^{-3} and c_1 for $\rho >$ 550 kg m $^{-3}$.

The grain size determined from Equation (3.29) shows the dependence on temperature and accumulation rate. This relationship should be verified with grain size measurements from field observations. It is a method to determine values for the grain size when no other method is available. However, results using this relationship are within observed grain size from optical measurements [*Scambos et al.*, 2007].

3.4 Modeling sub-annual firn layers

Observations from firn cores reveal seasonally variation in grain size, conductivity, density and densification rates. We applied the coupled grain growth, heat transfer and firn den-

sification model with monthly time steps to allow for processes that happen on seasonal timescales and would be missed with annual time steps. We seek to generate density and grain size profiles similar to what is observed, including minima and maxima in variation.

The procedure for this experiment is similar to the coupled grain growth, heat transfer and densification model with a few changes. The time steps are taken monthly instead of annually, and we do not use an effective temperature, but rather allow the seasonal variation in temperature to drive the Arrhenius -type rate equation.

The grain growth as in Equation (3.18), developed seasonal layers, with larger grains in the summer due to the Arrhenius factor and smaller grains in the winter. The amplitude between grain sizes in summer and winter layers is maintained throughout the grain size profile through this model. Seasonal differences in grain sizes at the surface are preserved, where layers that originated in the summer maintain larger grains throughout densification than layers that formed in the winter. The model is unable to replicate the switch in densification rates at densities of 600-650 kg m^{-3} [*Hörhold et al.*, 2011; *Freitag et al.*, 2004] described in Section 3.1.3. Observations show that the densification rate is sensitive to grain size, indicating that the effects of grain size need to be included in the model physics.

Including layering in models is important for assessing how sub-annual features in grain size and density evolve. For paleoclimate questions where lock-in and bubble close-off density are consequential, the variability in density is important.

Including seasonal layering in firn models is necessary to improve predictions of delta-age, however, there are complications. For example is the accumulation rate constant through out the year or does the pattern in accumulation rate favor one season? This is a problem familiar to the stable isotope community, where oxygen and deuterium isotopes from precipitation are a proxy for temperature, and that proxy can be biased if the accumulation is not constant throughout the year. A realistic parameterization of the seasonality of accumulation does not yet exist.

Future work for the modeling of sub-annual layers includes experimenting with other grain growth models, and constraining the densification model to reflect variability in densification observed in field and laboratory measurements.

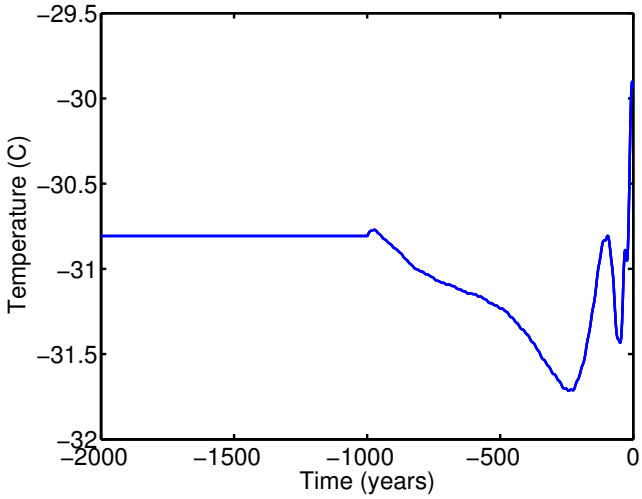

Figure 3.5: The recent surface temperature history for WSD from an inverse method using borehole temperature data [*Orsi*, 2011].

3.5 West Antarctic Ice Sheet Divide core delta-age and lock-in

The coupled grain-growth, heat-transfer and densification model is applied to the West Antarctic Ice Sheet Divide core (WDC) for the past 2000 years. Initial conditions and boundary conditions for the model are based on preliminary results from the drilling project. The shallow temperature profile is from January, 2008 and measurements have an accuracy of 0.2 K [*Orsi*, 2008]. The seasonal cycle influences the measurement, as is expected for a borehole temperature taken in the summer. Figure 3.5 shows the surface temperature, determined using an inverse procedure [*Orsi*, 2011]. The current density profile and accumulation history (Figure 3.6) are preliminary results from the WDC [*McConnell*, 2011]. The surface density is assumed to be 330 kg m^{-3}.

The model was tuned using the coefficients from tuned for the Anatarctic Peninsula [*Arthern et al.*, 2010]. The coefficient k_c in Equation (3.8) is 9.2×10^{-9} kg^{-1} ms and 3×10^{-9} kg^{-1} ms for the upper two zones of densification. The value of k_c is modified from the published value of 3.7×10^{-9} kg^{-1} ms to fit the current density profile for WDC, where the published values for k_c were tuned for conditions in the Antarctic Peninsula [*Arthern et al.*, 2010].

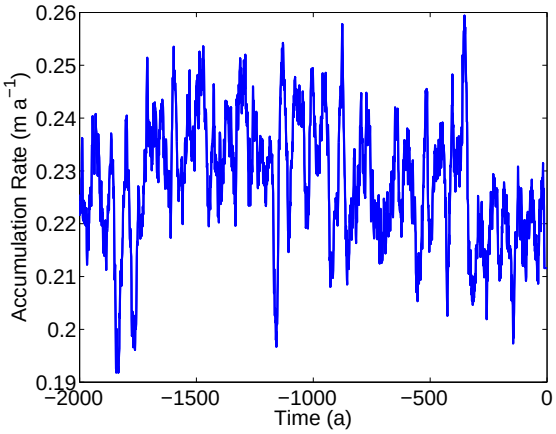

Figure 3.6: The preliminary accumulation rate for WSD [*McConnell*, 2011] in units of m a^{-1} ice equivalent.

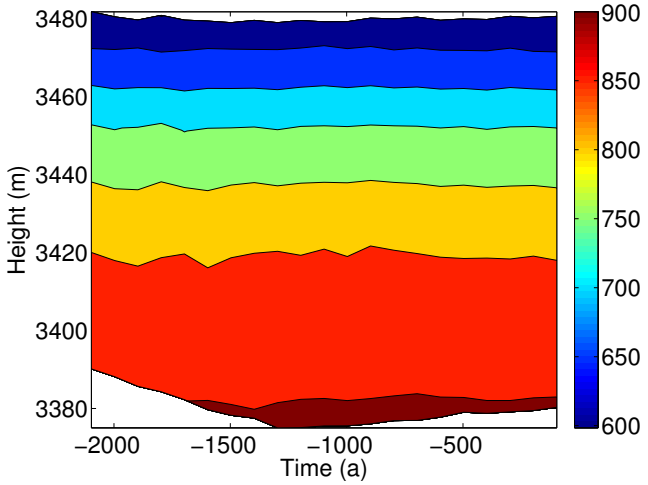

Figure 3.7: The density evolution at WDC for 2000 a.

Modeled 1-d evolution for density, temperature, and grain size at WDC are shown in Figures 3.7, 3.8, and 3.9. The final density profile in Figure 3.10 is less than 10% different than the measured density [*McConnell*, 2011]. It is not possible now to compare the final modeled grain-size profile in Figure 3.11 with measured data because data are scarce.

The modeled lock-in age for WDC is shown in Figure 3.12. The present lock-in age is approximately 210 years, 5 years younger than the delta-age previously measured [*Mischler et al.*, 2009]. The lock-in depth for WDC is shown in Figure 3.13. The modeled lock-in depth at present is 68m. Current lock-in depth estimates from other work are 65.5m [*Mischler et al.*, 2009], and 66.8m [*Battle et al.*, 2011], less than 2.5 meters shallower than our modeled estimate. The diffusive firn column from δKr and δN isotopes, along with their uncertainties are shown in Figure 3.13. The lock-in depth estimated from the isotopes (including the convective zone) is assumed to be 2 m greater the diffusive firn column measurements [*Orsi*, 2011]. The lock-in zone from δKr and δN has greater variability than the modeled lock-in results. The δKr and δN lock-in is more shallow than the modeled results for the last 500 years. Before this time, the lock-in depth estimates from δKr and δN and the modeled lock-in depth do not appear to be in phase. The δKr and δN method has uncertainty based on the location of the convective zone, and the lock-in depth from

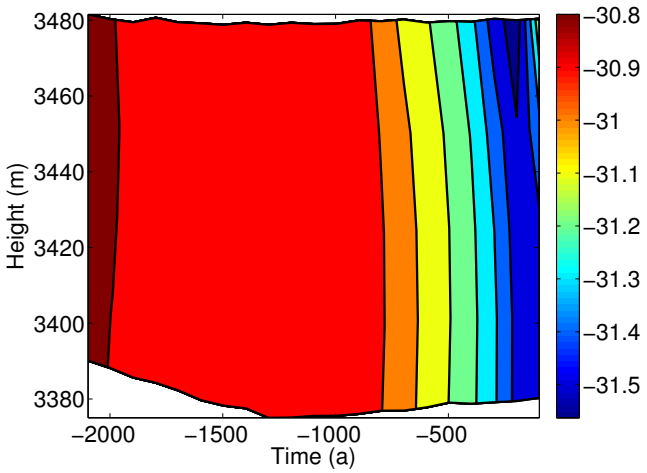

Figure 3.8: Modeled evolution of 1-d temperature field at WDC. The temperature field is relatively constant until about 700 years ago, when warmer surface temperatures began advecting down into the ice. The boundary condition T_s(0,t) is shown in Figure 3.5.

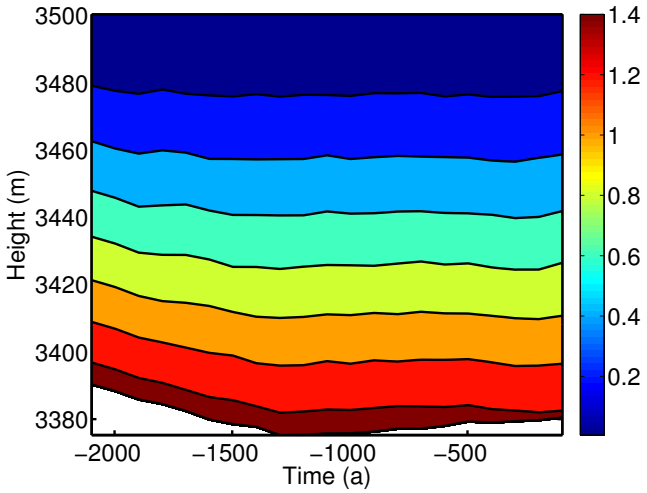

Figure 3.9: Modeled grain-size evolution for WAIS, with color bar reflecting the grain radius in units of μm.

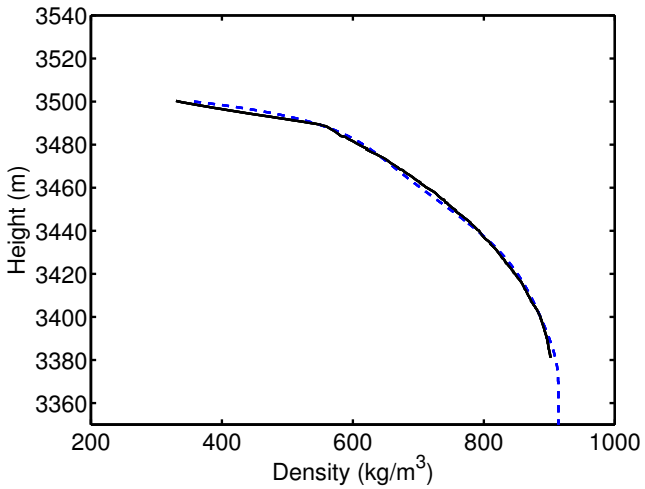

Figure 3.10: Present day density profile at WDC modeled (solid black) and measured (dashed blue)

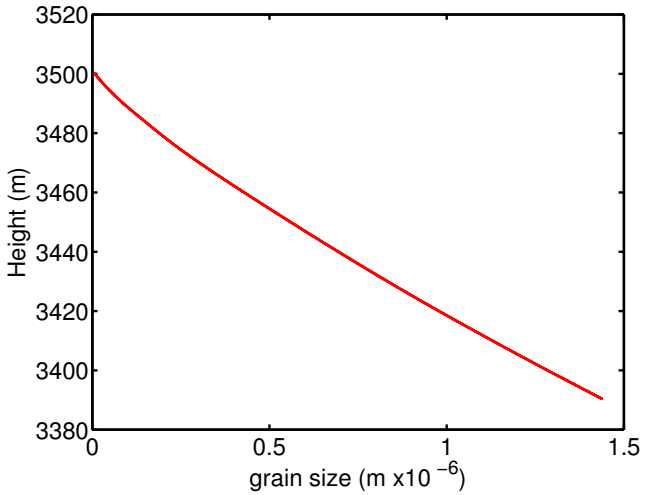

Figure 3.11: The modeled grain-size profile for WAIS.

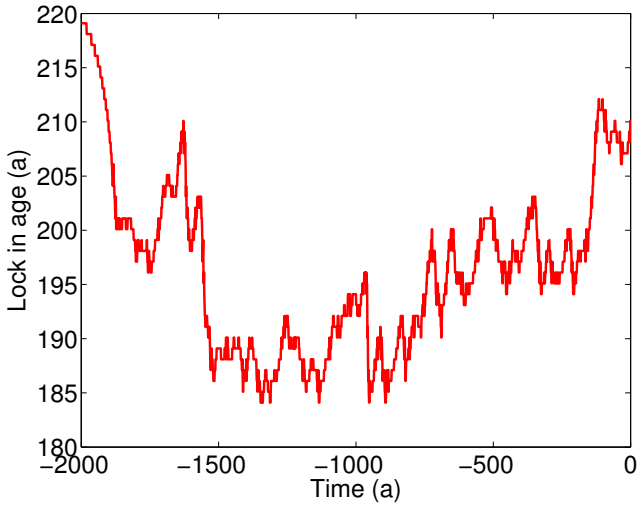

Figure 3.12: The lock-in age for WDC, estimated from firn densification modeling. The present lock-in age is approximately 205 years. The lock-in age before 200 AD is artifact from the model spin up.

the densification model is based on pore volume, and includes errors in estimating the open porosity at the lock-in.

The results from WDC, including the lock-in age and depth and bubble close-off age and depth, are preliminary including several preliminary datasets [*McConnell*, 2011; *Orsi*, 2011]. We are encouraged that our results are similar to results using laboratory-based methods. The next step is to apply the firn model to ice cores at Summit, Greenland, where numerous observations are available for model validation. Ideally, the grain size modeling can be compared as well.

3.6 Discussion and conclusions

A model has been developed to track the evolution of firn densification, with grain growth and heat transfer. This model determines the lock-in depth and delta-age as well as the bubble close-off age and depth. Other firn models have included grain growth, as far as we know, this is the first model to include grain growth and determine the evolution of the gas-age ice-age offset through time.

Model limitations include the lack of grain size data, and uncertainty in how to assign

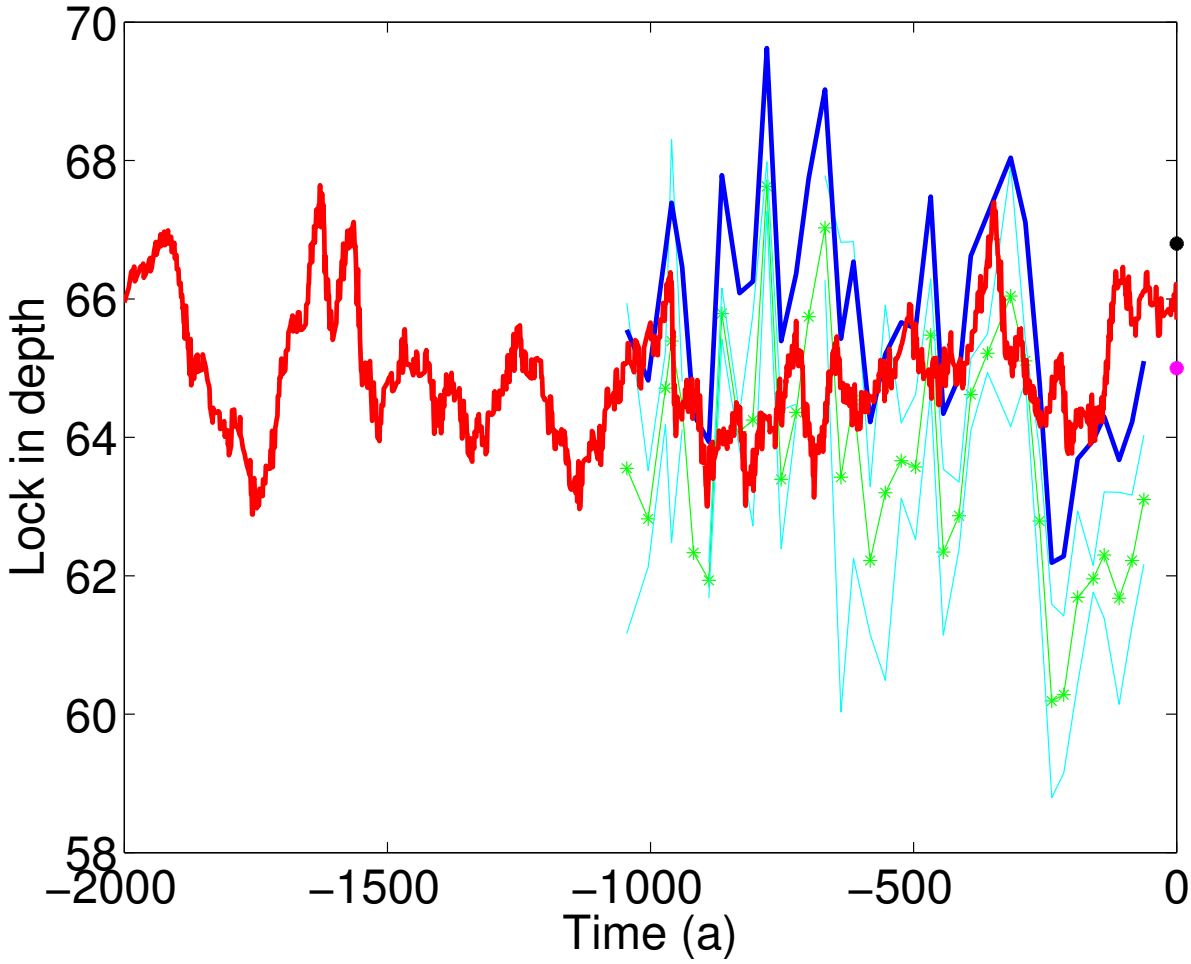

Figure 3.13: The diffusive column height modeled from the porosity (red). The krypton and nitrogen measurements (green stars) with uncertainty (cyan). The lock-in zone is estimated to be 2m greater than the δKr and δN measurements [*Orsi*, 2011, blue]. The diffusive firn column height of 65.5m [*Mischler et al.*, 2009, pink circle]. The diffusive firn column is estimated to be 66.8m [*Battle et al.*, 2011, black circle]

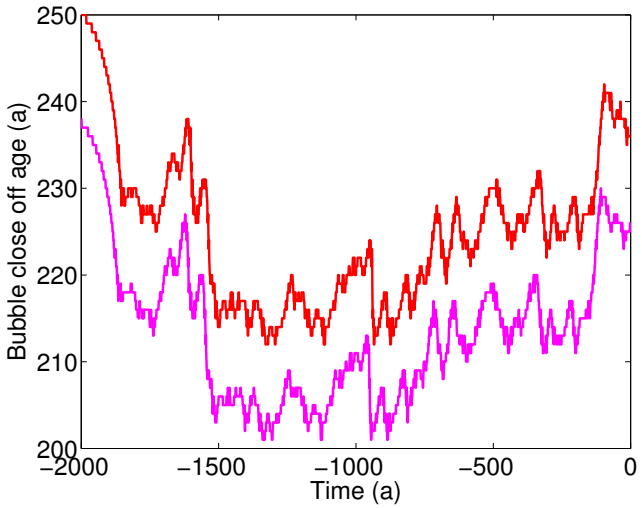

Figure 3.14: The bubble close-off age for WDC using the critical density based on the pore volume [*Martinerie et al.*, 1994, red] and constant 815 kg m^{-3} [*Barnola et al.*, 1991, pink]. The lock-in age before 200 AD is artifact from the model spin up.

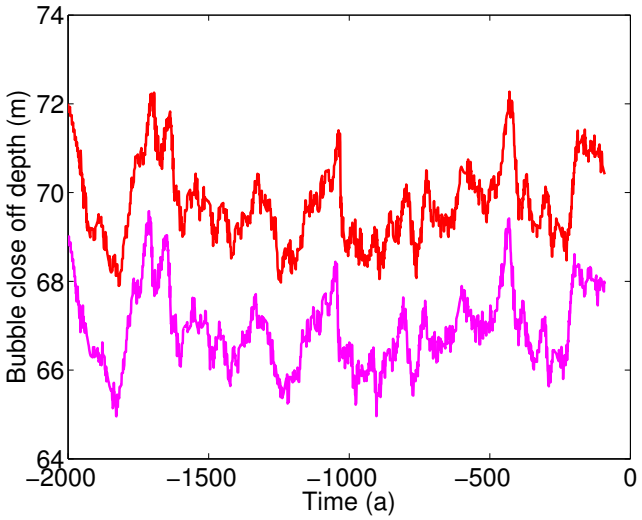

Figure 3.15: The bubble close-off depth for WDC using the critical density based on the pore volume [*Martinerie et al.*, 1994, red] and constant 815 kg m^{-3} [*Barnola et al.*, 1991, pink]. The lock-in age before 200 AD is artifact from the model spin up.

grain size boundary conditions. We recognize the modeled densification rate is very sensitive to grain size. Parameters for the densification model were originally derived using data from the Antarctic Peninsula [*Arthern et al.*, 2010]; additional work is needed to test the model using observations from other sites.

In an effort to capture features generated by seasonally varying temperatures (and potentially varying insolation), smaller time steps are needed for the coupled grain-growth and densification models. Our preliminary results need to be further constrained to reproduce the density variability observed in shallow firn cores. The coupled model has been applied to WSD, from 2000 a to present, to determine the lock-in and bubble close-off ages and depths. With an estimate of the accumulation and temperature records for the rest of the record, we can extend the delta-age record back further. In the meantime, future work includes applying the firn model to the Summit, Greenland ice cores, GRIP and GISP2 and comparing the results to previous work for these cores.

Chapter 4

SELF-CONSISTENT PALEOCLIMATE INFERENCES FROM MODELS OF ICE SHEETS

We have developed a self-consistent approach for modeling ice sheets to improve our understanding of ice-sheet evolution and paleoclimate reconstructions. The self-consistent model combines physical processes in the ice sheet in an integrated fashion. By using multiple data sets including observations from ice cores and radar layers, together with numerical approximations for physical processes in the ice sheet, we can constrain paleoclimate conditions that cannot be directly observed. Simultaneously we can constrain the past ice-sheet evolution, including the changes in the ice-sheet thickness and divide migration. The self-consistent model consists of modules, or subroutines, connected in an iterative loop. Using multiple data sets, including 2-d radar isochrones and 1-d ice-core records, allows additional constraints of the paleoclimate histories and ice-sheet evolution that affect the physical processes that produce these data sets. This is an improvement over using ice cores or radar data alone. Here, we establish the proof of concept that the self-consistent model can recover synthetic paleoclimate histories and ice-sheet evolution from data. This work paves the way for simultaneously reconstructing both the paleoclimate and ice-sheet evolution by using multiple datasets in a method that is self-consistent.

4.1 Introduction

Ice sheets are inherently self-consistent systems, obeying conservation of mass, momentum, and energy. Snow accumulates on the surface, and densifies as it advects downward, transitioning into ice. Although ice is the solid phase of H_2O, ice sheets deform and flow as a quasi-viscous fluid, due to gravity. While ice sheets as physical systems obey the conservation laws, the novel aspect of my research is that ice-sheet behavior has not previously been modeled to enforce self consistency, in this case determining a suite of histories (including accumulation rate, velocity and temperature fields, and thickness) that incorporate the gas-

age ice-age offset (delta-age), sparse depth-age profiles of ice cores, and radar isochrones. The goal is to determine a suite of histories that are compatible with physically based ice-sheet models and that fit the depth-age data well. The self-consistent approach determines chronologies for ice cores and the past configuration (including thickness and ice dynamics) of ice sheets. Antarctic ice cores are particularly difficult to date because the accumulation rates are low and annual layers are stretched due to ice flow and are too thin to date with high accuracy. Often annual layers are missing due to wind scouring. Radar layers, dated where they intersect ice cores, allow us to spatially extend ice-core age information, but we still need accurate dates on the radar layers.

Ice sheets operate in four dimensions including time. Data sets including ice cores, boreholes, radar and satellite provide up to 3-d information from the current ice sheet. We build numerical schemes to incorporate time, an additional dimension, to infer as much as possible about the previous ice-sheet configuration and climate conditions. Modeling applications allow us to combine multiple datasets to develop a cohesive understanding of the evolution of the ice-sheet and climate.

This work addresses several over-arching questions in glaciology that have important implications.

(1) Paleoclimate applications require an accurate chronology in order to determine the precise timing of climate events. This is necessary for studying individual ice cores, and also for comparing climate events across several ice-core records. When a climate event is not simultaneous among records, it is especially important to have accurate chronologies to accurately assign the timing. An example is warming events in the Northern and Southern hemispheres. We know that the Poles are not symmetric in the patterns of warming and cooling, but rather act like a bipolar seesaw [*Broecker*, 1998]. Comparing ice-core records to other records such as sediment cores and cave speleothems, again requires accurate chronologies to ensure that the best interpretations are made.

(2) The past ice-sheet configuration includes the past ice-sheet thickness (1-d and 2-d) and volume (3-d). Establishing where the ice was in the past is important for many facets of Earth science. Temperature reconstructions from stable isotopes must be corrected for

the ice-sheet elevation, where colder temperatures are experienced at higher elevations. Isostatic-rebound studies require an estimate of the past ice-sheet volume to determine the rate of rebound of the Earth since the last glacial period when there was a greater ice load on the Earth's lithosphere. Isostatic rebound is one of the greatest uncertainties in ice-sheet contributions to sea-level rise from gravity satellites including GRACE (Gravity Recovery and Climate Experiment) [*Rignot et al.*, 2011, e.g.].

(3) The spatial accumulation-rate history could help to constrain Global Circulation Models (GCM). Data for precipitation (referred to as accumulation in polar regions) and temperature are important for constraining GCM results. Inverse methods applied to ice-core records provide some of the only records of accumulation rate from polar regions. The accumulation rate is equivalent to P-E (precipitation minus evaporation).

4.1.1 Ice flow and deformation

As ice advects from the surface towards the bed, it undergoes internal deformation due to longitudinal and shear stresses. If the accumulation rate increases, more mass enters the glacier and the glacier will either thicken or flow faster to accommodate the increase in mass. The thickness and divide migration respond to the changes in accumulation rate and flux changes at the ice-sheet boundaries. Approximations for modeling ice flow include the *Dansgaard and Johnsen* [1969] model and Shallow Ice Approximation [*Paterson*, 1994, SIA, p. 86]. Ice-flow modeling can be conducted in 1-d, 2-d and 3-d applications, depending on the research question and nature of the site. Here we use 2-d ice-flow models to capture upstream variations in the accumulation rate and spatial variation in the ice-sheet thickness.

4.1.2 Firn densification

Snow turns into ice over hundreds to thousands of years, and in the process, traps atmospheric gases. Gas bubbles are always younger than the enclosing ice, often by an uncertain amount. This age difference, called delta-age, can be estimated with firn-compaction models; which depend on accumulation rates in the past. Firn-densification models [*Herron and*

Langway, 1980; *Spencer et al.*, 2001; *Goujon et al.*, 2003; *Arthern et al.*, 2010, e.g.] require knowledge of the temperature and accumulation rate. The bubble close-off history is the age difference between the ice and air when the bubbles are trapped. Delta-age is more difficult to determine for Antarctic ice because there are fewer constraints from thermally fractionated gases to independently check firn-densification models [*Goujon et al.*, 2003]. Delta-age is larger for East Antarctic ice cores, because the ice is colder and the accumulation rate is lower. It is especially important to constrain delta-age for these ice cores, however, because the uncertainty is also great. To address questions regarding timing of climate events in the temperature record and atmospheric-gas records, an accurate estimate of delta-age is required. During Antarctic Glacial terminations, temperature precedes changes in carbon dioxide by 800 years [*Caillon*, 2003]. If the uncertainty in delta-age is greater, the timing of climate events could be missed, including asynchronous changes in atmospheric gas concentration and temperature.

4.1.3 Inverse methods

We use geophysical inverse methods [*Aster et al.*, 2005; *Hansen*, 1998; *Parker*, 1994, e.g.] to infer boundary conditions, initial conditions and coefficients, which are parameters of a model for which we are solving. The model parameters cannot be directly measured; therefore we use an inverse method composed of a forward problem and an inverse problem. The forward problem makes a prediction of observable data. The inverse problem finds the best model to fit the observable data to some tolerance that depends on the data.

4.1.4 Previous work

Previous work [*Lemieux-Dudon et al.*, 2010], determined thinning functions (See Section 2.1.2), accumulation-rate history, ice age, and gas age for four ice cores, including the Greenland core North GRIP (NGRIP), and three Antarctic cores including Vostok, EPICA Dome C (EDC), and EPICA Dronning Maud Land (DML). Their method included a Bayesian statistical framework used with a Monte Carlo inverse method. Background scenarios were generated for each ice core, tying in best estimates for thickness changes and accumulation

rates determined from oxygen isotopes $\delta^{18}O$. Thinning functions were determined using ice-flow models and values from the literature. In the forward problem, simplified relationships among the parameters were assumed, avoiding the computational load of running the complex forward algorithms (including firn models and ice-flow models) thousands or millions of times to solve the inverse problem. Results included suites of histories for the EDC and DML cores, and the authors did not include dating updates to the Vostok and NGRIP cores, citing too few data are used to constrain the Vostok chronologies and artificially preventing chronology updates in the GICC05 chronology for NGRIP. In the work presented here we focus on one ice-core record rather than several at once. We use a frequentist statistical framework, which does not require *a priori* knowledge of the nature of the model or model statistics. Rather than form simplified relationships among the variables, we use an iterative procedure to combine inverse problems, with physical approximations for 2-d ice flow and firn densification.

4.2 Methods

4.2.1 Generating synthetic data

Using synthetic data is an important step to ensure that the self-consistent model converges as expected, before applying the self-consistent method to real data. Since we use known values of the parameters to generate these particular synthetic data, we can test how well the self-consistent model recovers the known values. Values for many of the ice-sheet parameters used to generate the data are shown in Appendix G. The flowchart in Figure 4.1 shows how the synthetic data are generated using a series of forward models. The upper box shows arbitrarily assigned values, including layer ages, a spatial and temporal accumulation-rate, bed elevation, an initial steady-state ice-sheet thickness and velocity shape functions. Details on how the steady-state ice-sheet thickness is derived are found in *Koutnik* [2009, Appendix E p. 244-250]. The middle box in Figure 4.1 shows parameters determined with a 2-d dynamical forward model with a prescribed analytic temperature field. Using the assigned accumulation rate $\dot{b}(x,t)$ and the initial ice-sheet thickness $H(x,0)$, we use a limited-domain model (See references [*Koutnik and Waddington*, 2012, In review; *Koutnik*,

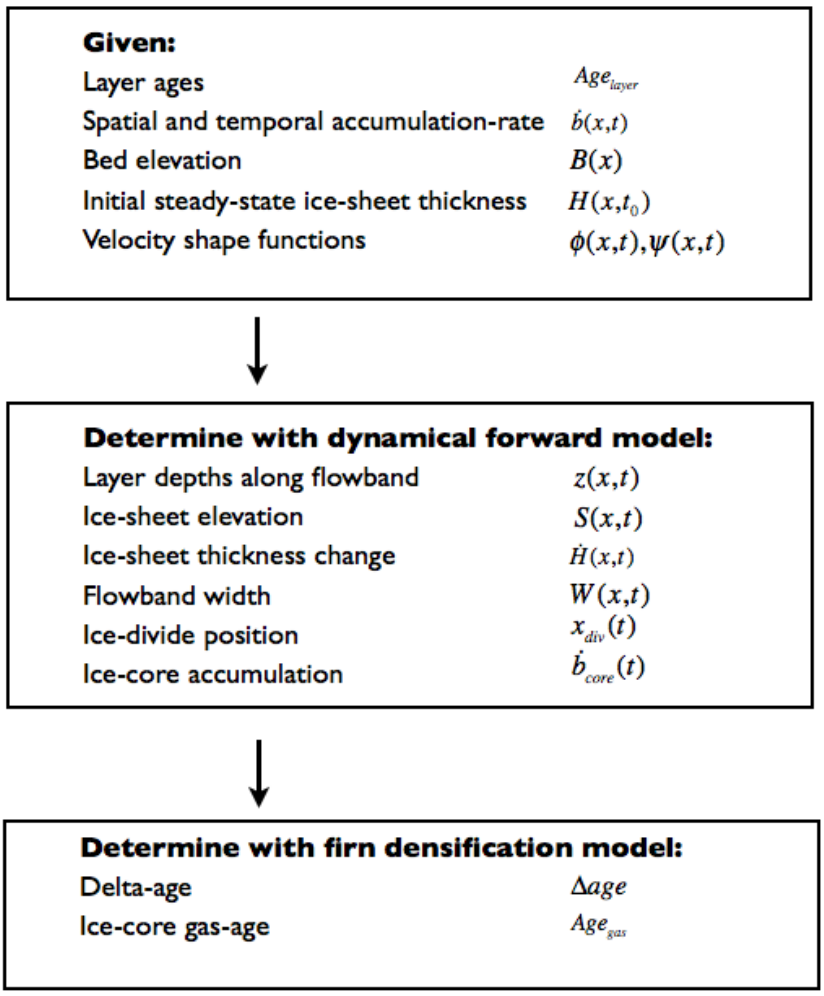

Figure 4.1: Synthetic data are generated for the self-consistent method using forward models, including a dynamical flow model (middle) and a firn-densification model (bottom).

2009, Chapter 4] for details), where we can be computationally efficient and focus on the ice flow within the domain, which evolves as if it were part of a full-domain ice sheet. The limited-domain model includes determination of the ice fluxes at the boundaries Q_{in} and Q_{out}, consistent with the evolution of a full ice-sheet. The dynamical forward model determines the past configuration of the ice-sheet, including: surface elevation $S(x,t)$, temporal surface elevation change $\dot{S}$, ice-sheet thickness $H = S - B$, and divide migration. We determine the horizontal and vertical velocity field by integrating the displacement of particles. From the particle trajectories, we can generate synthetic layers.

Red noise (see Appendix B), is added to the radar-layer depths. The 1-σ depth uncertainty is 3m. The dynamical forward problem is further described in Appendix H.

With a known velocity field and surface elevation history, we can calculate model values of observable ice-sheet parameters at the ice core. We define and refer to the ice-core accumulation rate $\dot{b}_{core}$ as accumulation rate at the time and place where particles were deposited prior to following trajectories that brought them to the ice-core site today. Unless the ice core is drilled at a divide that has not migrated, there are upstream effects for snow that falls and advects to the current ice-core location. The ice-core accumulation rate $\dot{b}_{core}$, as we have defined it, is not the accumulation rate that falls at the ice-core site, but rather includes upstream variations in the accumulation that is advected to the current ice-core location. In the lower box in Figure 4.1 a transient firn-densification model determines the delta-age, using the ice-core accumulation rate $\dot{b}$ and temperature field for the ice core. The gas age Age_g is evaluated from the ice age Age_i and delta age Δage,

$$Age_g = Age_i - \Delta age. \tag{4.1}$$

Table 4.2.1 describes the variables in the flowchart in Figure 4.1, displaying the parameters and where they are assigned or generated.

Synthetic data sets are generated with two accumulation-rate patterns $\dot{b}(x,t)$,

$$\dot{b}(x,t) = b_t(t) + b_x(t)x, \tag{4.2}$$

which vary spatially and temporally. The functions b_t and b_x define the magnitude and slope of the spatially linear accumulation rate through time. The first data set is similar to

Table 4.1: The synthetic data generated for the self-consistent method is similar to WAIS site conditions. We generate the data using forward models including a dynamical flowband model and a firn densification model. Figure 4.1 shows a flowchart with similar variables.

Variable	Description	Model evaluated
x	Distance along flowband	Assigned
A_{layer}	Layer age	Assigned
$\dot{b}(x,t)$	Spatial and temporal accumulation-rate	Assigned
$H(x,t_0)$	Initial ice-sheet thickness	Assigned
$z_{layer}(x)$	Layer depths along flowband	Dynamical ice flow
W	Flowband width	Dynamical ice flow
$S(x,t)$	Ice-sheet surface elevation	Dynamical ice flow
$\partial S(x,t)/\partial x$	Spatial derivative of surface elevation	Dynamical ice flow
$\partial H(x,t)/\partial t$	Temporal change in ice-sheet thickness	Dynamical ice flow
$\phi(x,t)$	Horizontal-velocity shape function	Dynamical ice flow
$\psi(x,t)$	Vertical-velocity shape function	Dynamical ice flow
$x_{divide}(t)$	ice-divide position	Dynamical ice flow
$\dot{b}_{core}(t)$	Ice-core accumulation rate	Interpolation
$\Delta age(t)$	Ice-core delta-age	Firn densification
Age_{gas}	Ice-core gas-age	Firn densification

estimates for WAIS [*Neumann et al.*, 2008] and the second varies smoothly through time. The same spatial gradient b_x is used for both accumulation-rate histories. The two patterns differ in the temporal variation.

Synthetic data set 1: estimates for WAIS

We note that preliminary data from the WAIS ice core show that there is potentially significant melting at the bed and consequently, the ice is not as old [*Fudge et al.*, 2011] as was estimated in the site selection [*Conway et al.*, 2005]. However, we assume that the ice can be dated back to 60 ka without being compromised by flow disruptions at the bed. From shallow radar layers we know that the Holocene accumulation history at the WAIS divide shows a persistent accumulation gradient [*Neumann et al.*, 2008]. Figures 4.2 and 4.3 show the spatially and temporally varying accumulation-rate patterns used in the dynamical flowband model. The accumulation rate is lower in the glacial with a minimum at 20 ka and increases to a maximum at 10 ka in the Holocene.

Figure 4.4 shows the surface evolution with the WAIS-like accumulation rate used to generate the data, as is shown in Figure 4.1. The surface evolution was determined using a dynamical ice-flow model.

Figure 4.5 shows where the ice core intersects the synthetic radar layers. Particles in the ice core started along the flowband between the divide at 21.1 km and the ice-core site at 3 km, (assuming the divide position has not changed). The accumulation rate $\dot{b}_{core}$ experienced by the ice in the core (Figure 4.6) is derived from those origin points in space and time. This synthetic example resembles WAIS, where the ice core is located 24 km downslope of the present divide. Because there is a strong spatial gradient in the accumulation, the upstream accumulation rate is greater and the annual layers are thicker. Other upstream effects are also important. If the snow falls upstream at a higher elevation, the isotope record will reflect colder temperatures than the temperature at the ice-core site. This is more difficult to adjust for because the spatial and temporal corrections for isotopes must be known.

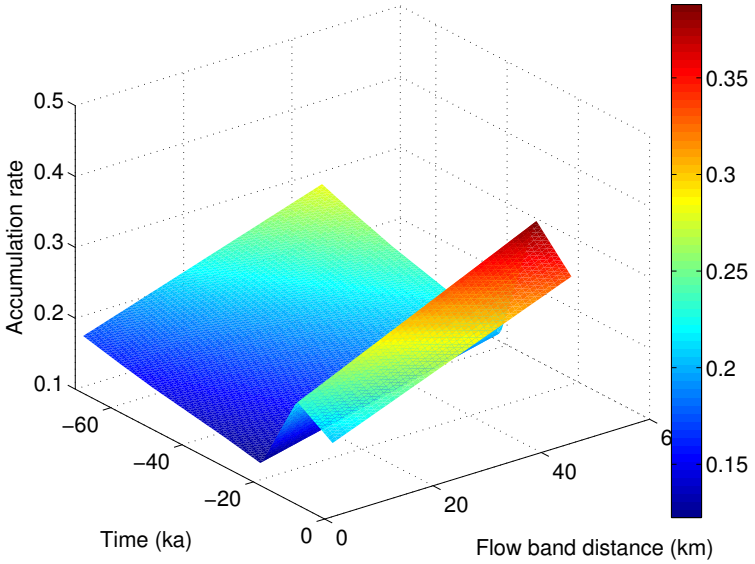

Figure 4.2: The synthetic spatial and temporal accumulation rate $\dot{b}(x,t)$. Temporal variation includes a minimum at 20 ka and maximum in the Holocene at 10 ka. The divide is at 21.1 km and the ice-core site is at 3 km on the flowband. The spatial accumulation-rate pattern is similar to estimates for WAIS [*Neumann et al.*, 2008], with the Ross Sea on the left, and Amundsen Sea on the right.

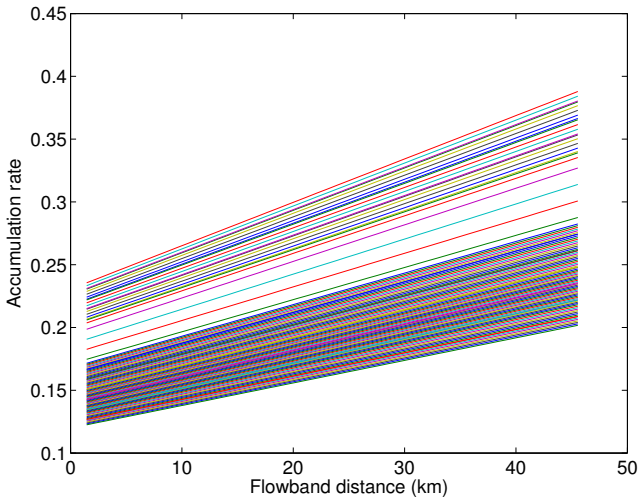

Figure 4.3: The synthetic accumulation rate $\dot{b}(x,t)$ has a spatial slope that changes magnitude through time. The advection from upstream develops relatively thicker layers at the core site at 3 km. This figure is a view along the time axis of Figure 4.2.

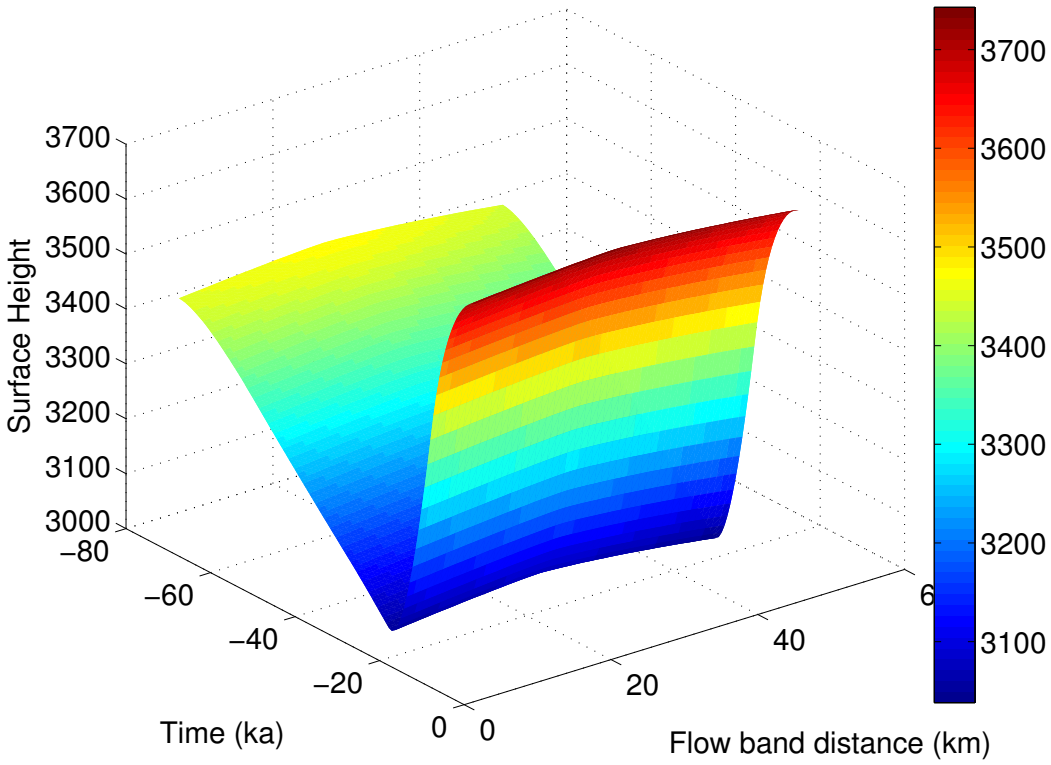

Figure 4.4: The surface evolution resulting from the accumulation rate in Figures 4.2 and 4.3, as determined by the dynamic forward model used to generate the data. This surface-evolution history is used without modification in the kinematic forward model in the inverse method.

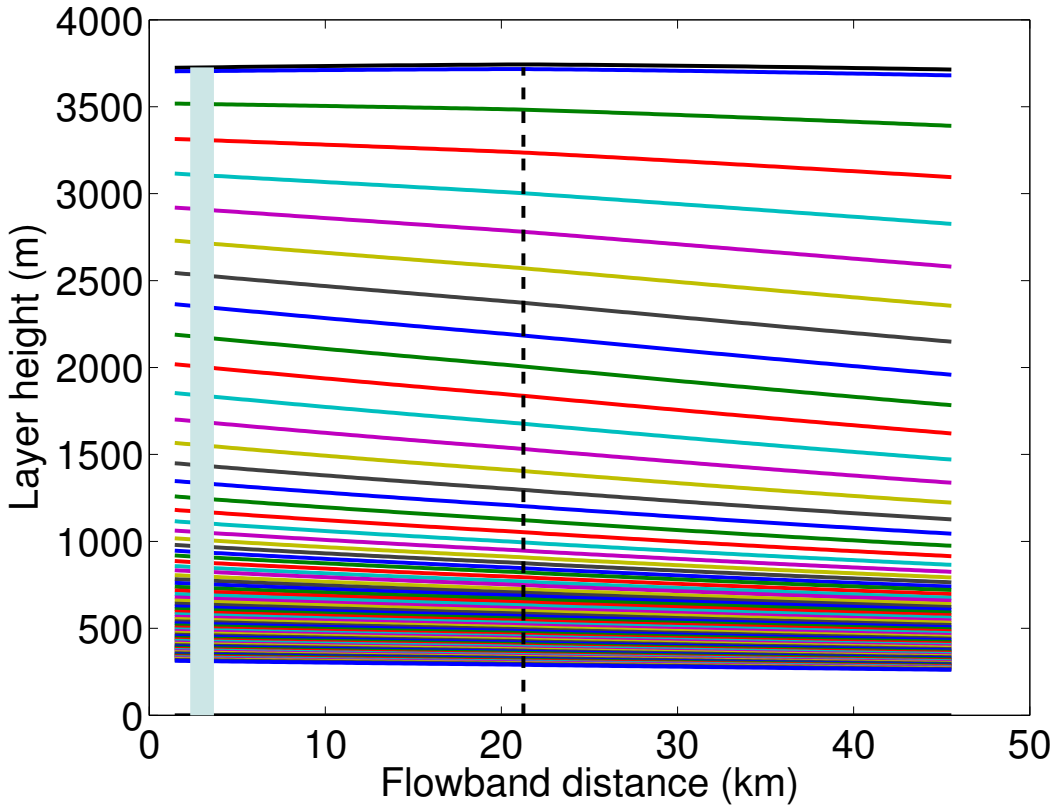

Figure 4.5: The synthetic radar layers and ice core are shown with the modern surface elevation and divide position (dashed vertical line), 21.1 km along the flowband. The core is at 3 km on the flowband, 18.1 km from the ice divide. Not all of these synthetic radar layers are used in the inverse method.

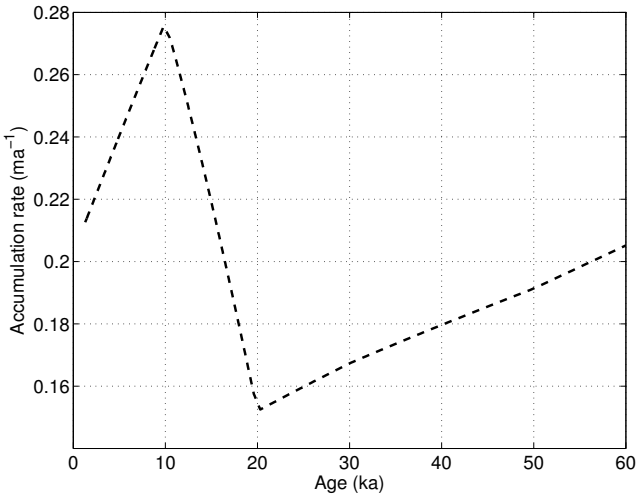

Figure 4.6: The synthetic accumulation rate $\dot{b}(t)$ for ice recovered in the ice-core site includes upstream effects, accumulation that fell and advected to the present ice-core location, 18.1 km from the ice divide. The history of the accumulation rate for the ice in the core is not equivalent to the accumulation-rate history at the current ice-core location.

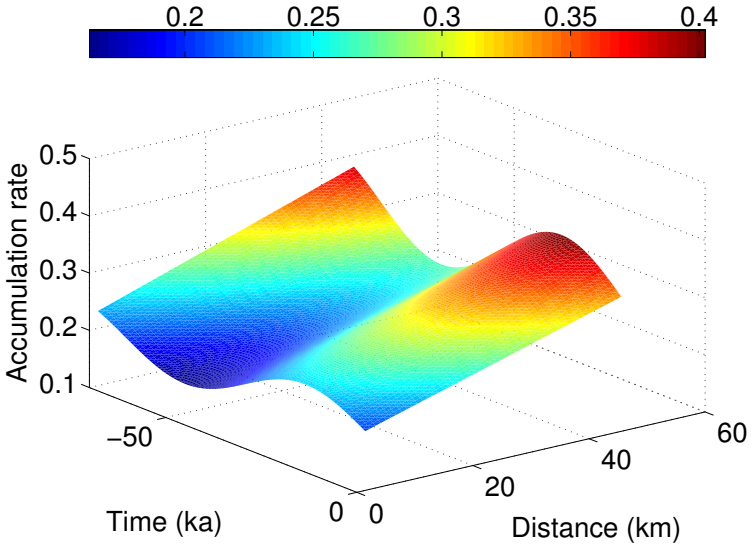

Figure 4.7: The second synthetic spatial and temporal accumulation rate $\dot{b}(x,t)$. The spatial accumulation-rate pattern is similar to *Neumann et al.* [2008], with the Ross Sea on the left, and Amundsen Sea on the right. The divide is at 16.8 km and the ice-core site is at 3 km on the flowband.

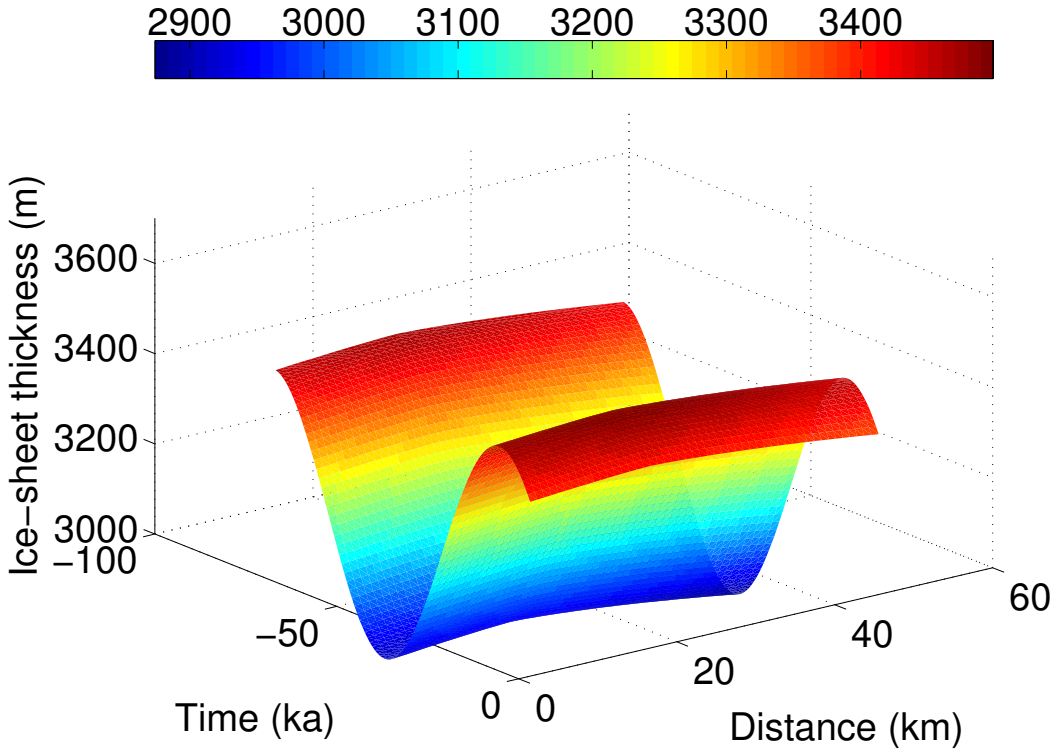

Figure 4.8: The surface evolution for the second synthetic example. This surface evolution is determined in the dynamic forward model used to generate the data. This surface-evolution history is used without modification in the kinematic inverse problem.

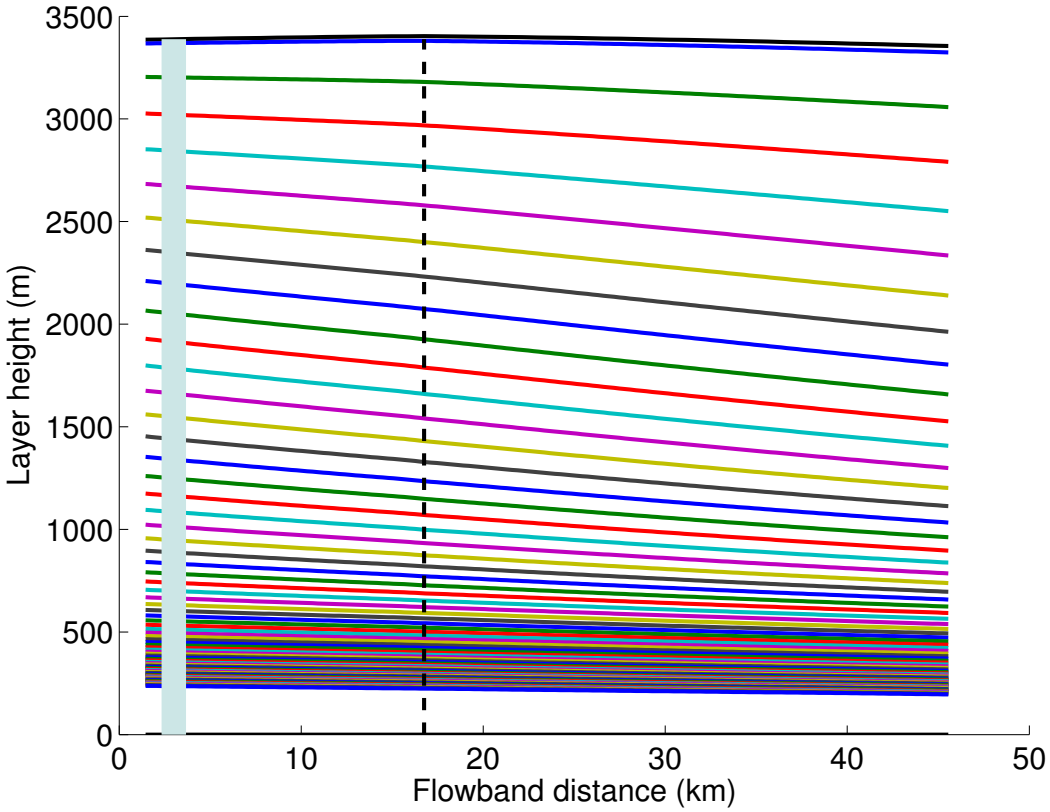

Figure 4.9: The synthetic radar layers and ice core (solid vertical line) are shown with the modern surface elevation and divide position (dashed vertical line), 16.8 km along the flowband. The current ice divide position is different for the second data set than the first, as shown in Figure 4.5, due to differences in the synthetic accumulation rate (Figures 4.2 4.7). The ice core at 3 km is approximately 13.8 km from the ice divide. Not all of these synthetic radar layers are used in the inverse problem.

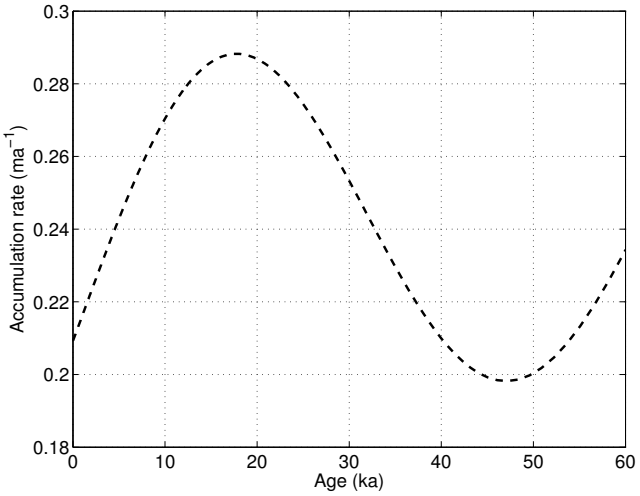

Figure 4.10: The synthetic accumulation rate $\dot{b}(t)$. The accumulation rate at the ice-core site includes upstream effects, which includes accumulation that fell and advected to the present ice-core location, 16.8 km from the ice divide. The accumulation rate at the ice core is not equivalent to the accumulation that fell directly at the current ice-core location.

Synthetic data set 2: accumulation rate with smooth temporal variation

The second synthetic $\dot{b}$ data set varies smoothly; as shown in Figure 4.7, the temporal pattern $b_t(t)$ in Equation (4.2) is sinusoidal. The spatial-gradient history $b_x(t)$ is the same as was used to create data set 1. The ice-thickness history associated with the smooth accumulation rate in Figure 4.7 is determined using a dynamical forward model. The synthetic radar layers and ice-core location are shown in Figure 4.9. The present ice divide is located at 16.8 km in this synthetic case, different from 21.1 km in the previous case. This difference in the present ice divide is due to the change in the thickness, which is caused by a different accumulation rate pattern. In the second synthetic data set, the ice core is 13.8 km from the present ice divide. The ice-core accumulation rate $\dot{b}_{core}$ in Figure 4.10 has a smooth temporal pattern.

4.3 Self-consistent method

4.3.1 Overview

The goal of this work is to develop and integrate several modular units into a model to better constrain past ice dynamics and paleoclimate records. The model development includes three modeling efforts,

(1) inference of histories of spatial accumulation patterns from layers in a 2-d flowband model,

(2) determination of the ice-age gas-age (delta-age) difference at each depth from a firn-densification model, and

(3) development of a continuous ice-core chronology that can be used to date radar layers.

These models are introduced below and shown in Figure 4.11.

The modules presented here can be replaced while still following the logic path in Figure 4.11. We show a generic dating scheme as might be used for dating an Antarctic ice core; however, processes incorporated in the modules should reflect the site-specific considerations. Such considerations may include the nature of the ice-bed interface (frozen, melting or sliding).

4.3.2 Inferring Histories of Accumulation

This geophysical inverse problem infers the spatial and temporal patterns of accumulation rate based on dated internal layers detected by ice-penetrating radar. Similar methods have been used, implementing 2-d forward models with an inverse approach [*Martín et al.*, 2006]. Previous work paired inverse methods with 2.5-d flowband forward models to determine the accumulation rate [*Waddington et al.*, 2007; *Steen-Larsen et al.*, 2010], and the surface elevation $S(x,t)$ [*Koutnik*, 2009]. We use a 2-d kinematic flowband forward model of suitable complexity to calculate present-day internal-layer geometry from a specified spatial and temporal accumulation-rate history, and other rheological parameters. The surface elevation $S(x,t)$ is specified and is not updated in the iterative procedure. The forward problem uses an analytic temperature field [*Paterson*, 1994, p. 216] with a constant surface boundary condition of 29.7 °C similar to WAIS today [*Orsi*, 2009]. The initial guess for

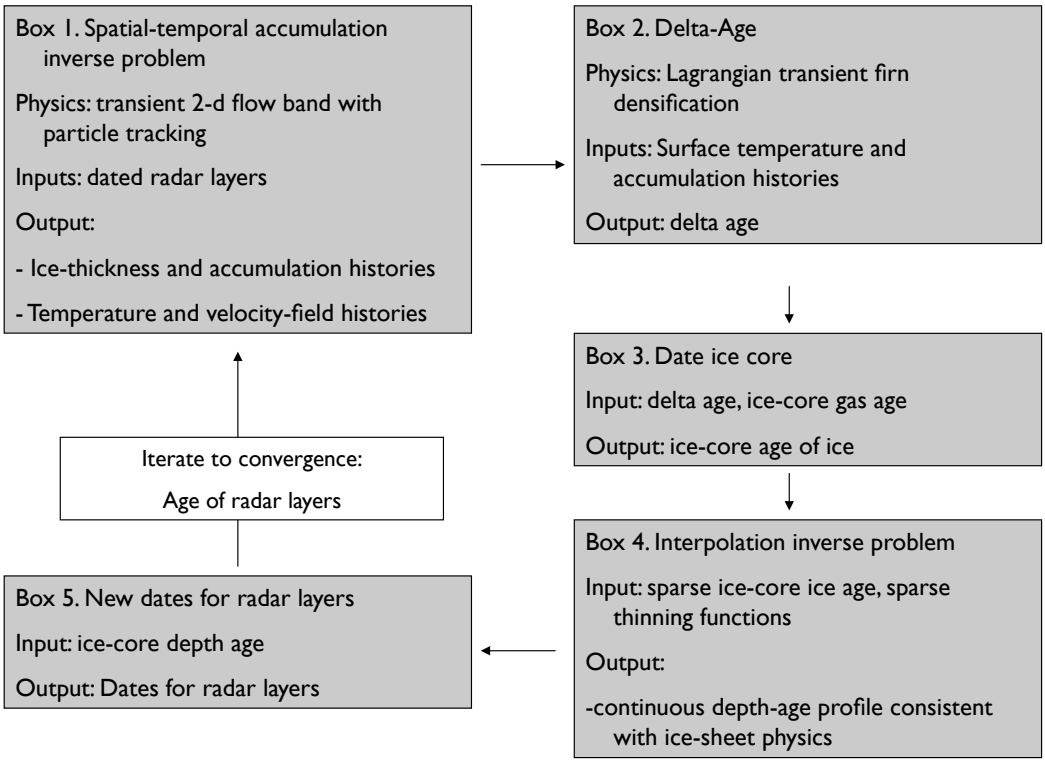

Figure 4.11: The self-consistent method uses several modules, as outlined in the flow chart. Flow begins in the upper left corner and proceeds clockwise until the convergence criteria are met (white box).

the accumulation rate is constant and uniform. Other options for the estimation the initial accumulation rate include the local layer approximation [*Waddington et al.*, 2007, LLA]. The inverse problem selects a spatially and temporally smooth accumulation-rate to match the radar layers at an appropriate level of accuracy. The modern spatial accumulation rate and horizontal velocity also constrain the problem. The inverse procedure is described in *Koutnik* [2009, Chapter 5].

Given the age and depth of a layer, this method infers a spatial and temporal accumulation-rate history that matches radar layers well, but not exactly, to avoid over-fitting the data. This non-linear problem uses the Tikhonov regularization method, implementing a Lagrangian trade-off parameter to determine the best solution, with a residual norm equivalent to a tolerance value based on the quantity of data and their uncertainties.

The layer thickness λ at the ice core is determined as the difference in the layer depths. The thinning function Λ is found by rearranging the equation,

$$\lambda = \Lambda \dot{b}_{core}. \tag{4.3}$$

More discussion about the thinning function is found in Section 2.1.2.

4.3.3 Firn densification

The coupled firn model in Chapter 3 includes grain growth, heat transfer and densification. For this application we are not considering changes in the surface temperature, which would otherwise result in changes in the densification rate and bubble close-off age. The bubble close-off age is affected primarily by changes in the accumulation.

4.3.4 Inferring an ice-core chronology

We infer the ice-core depth-age from the gas-age record. The age of the ice is the age of the gas plus the delta-age (Equation (4.1)). Using gas ages is an important method for dating deeper ice. In practice, the shallow ice can sometimes be dated by counting annual layers until the layers become too thin to count reliably.

In Chapter 2, we motivated the need for a physically based method for inferring the depth-age relationship for an ice core. We showed why interpolations including linear and

Table 4.2: The synthetic scenarios for self-consistent model results

Scenario number	Initial guess of radar-layer ages for inverse problem	Generated synthetic accumulation rate $\dot{b}(x,t)$
1	10% too young	WAIS-like
2	10% too old	WAIS-like
3	10% too young	smoothly varying
4	10% too old	smoothly varying

exact-fit splines are inadequate, because they include no physics representing ice deformation. We implement the same inverse procedure here to determine the depth-age relation of the ice core. The sparse ice-age data come from dated gas ages and calculations of the delta-age. Additional data could be used in the future, including depth-age data from layer counting. We add one additional data point at the surface, where we know that the depth and age are zero.

4.4 Results

Using WAIS-like data, we apply the self-consistent method to four data scenarios listed in Table 4.4. For scenarios (1) and (2), the radar-layer ages initially are 10% younger and (2) 10% older than the true radar layers. The synthetic accumulation rate in Figure 4.2 is similar to WAIS reconstructions has abrupt changes in the temporal variation $b_t(t)$ including a minimum at 10 ka and a minimum at 20 ka. Five self-consistent iterations, following the Figure 4.11 flowchart were made for each scenario. For scenarios (3) and (4), the initial guess for the radar-layer ages is similar to scenarios (1) and (2), at 10% younger and older than the true radar layers respectively, and the synthetic accumulation history is smoothly varying, without corners.

In all four scenarios, red noise has been added to radar-layer depths, assuming an uncertainty of 3m. Red noise with an uncertainty of 2% of the age was also added to the correct (synthetic) gas ages.

4.4.1 Results for WAIS-like synthetic accumulation rate

The results for scenario (1) are shown in Figure 4.12 through 4.18. The results for scenario 2 are shown in Figures 4.19 through 4.25. In scenarios (1) and (2), the best depth-age of the radar layers is constrained to within 6% of the true radar-layer ages. The sparse ice ages are within 2.5% of the true ice ages.

Scenario (1) results

In scenario 1, I start the self-consistent method with radar layers that are 10% younger than the true ages. Consequently in the first iteration of the self-consistent loop, the 2-d flowband inverse method (in Box 1 in Figure 4.11) produces accumulation rates (Figure 4.12) that are higher than the synthetic accumulation rate $\dot{b}$ to reach the radar-layer depth data. In iterations 2 through 5, the accumulation rate decreases toward the true accumulation rate. Figure 4.13 shows the difference between the inferred model and the correct synthetic accumulation rate. The largest deviations are at the maximum and minimum in the accumulation rate at 20 ka and 10 ka. The inverse problem incorporates a smoothness constraint on the temporal variation, and that constraint does not allow the inferred accumulation rate to reproduce the abrupt changes in the synthetic solution. Yet, the inferred accumulation rate clearly contains structure from fitting noisy data. A future experiment could be to relax the smoothness constraint at those few times when we do not expect the solution to be smooth.

The dates of the radar layers shows the greatest improvement in the second self-consistent iteration (Figure 4.14). At the first iteration, ages are 10% too young, whereas subsequent iterations are within 3% of the true age. There is insignificant improvement after the second self-consistent iteration. The trend in the increase from radar layers is due to the linear increase in the age uncertainty on the gas-age control points. If a constant uncertainty were used, this trend would likely not be present.

The interpolated ice-core accumulation rate $\dot{b}_{core}$ is shown in Figure 4.15. The accumulation rate from the first iteration is higher than the synthetic value because the radar layers are assumed to be too young, causing us to infer a higher accumulation rate. Subsequent

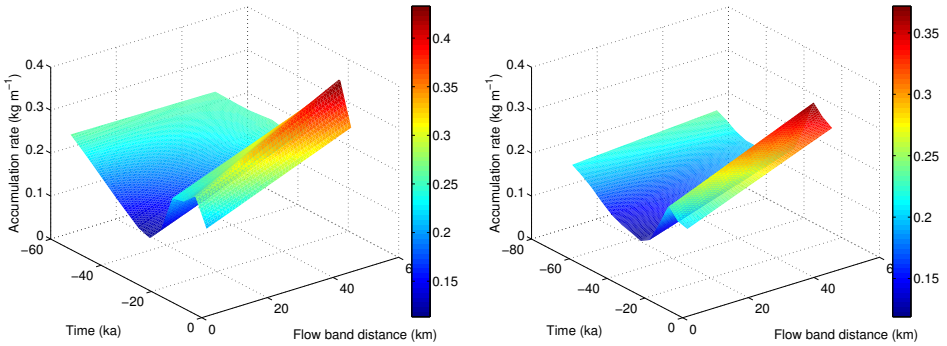

(a) Iteration 1

(b) Iteration 2

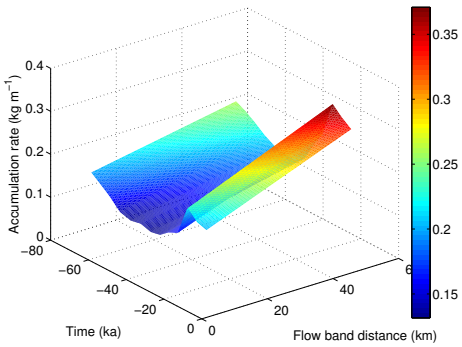

(c) Iteration 3

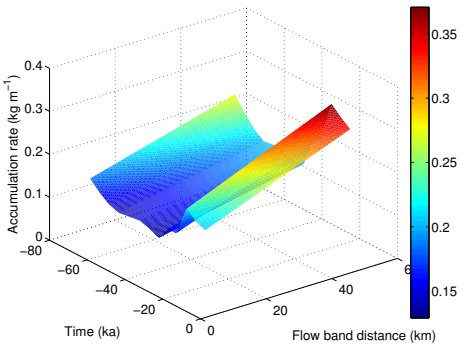

(d) Iteration 4

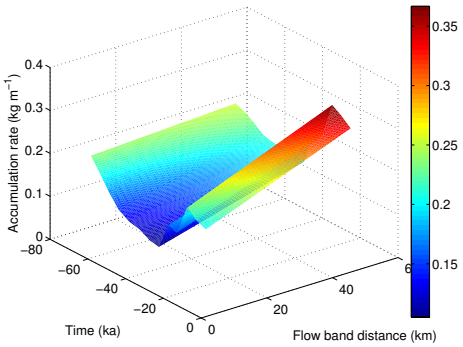

(e) Iteration 5

Figure 4.12: The spatial and temporal accumulation rate inferred from 5 iterations of the self-consistent loop, beginning with layer ages that are 10% younger than the true layer ages.

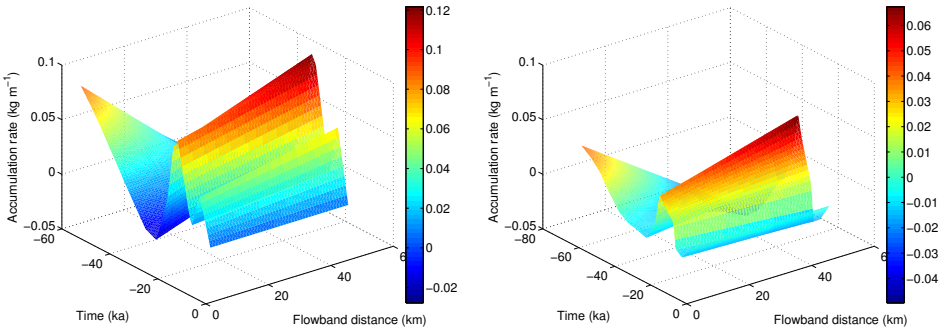

(a) Iteration 1

(b) Iteration 2

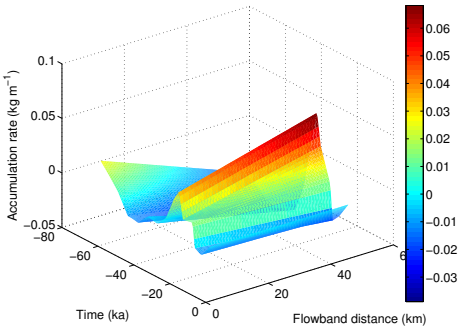

(c) Iteration 3

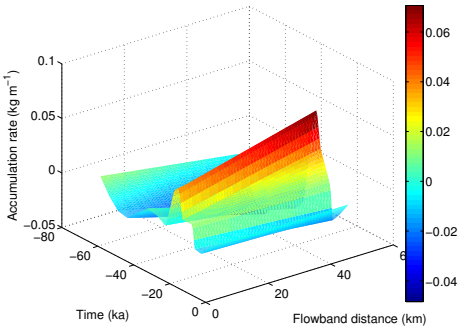

(d) Iteration 4

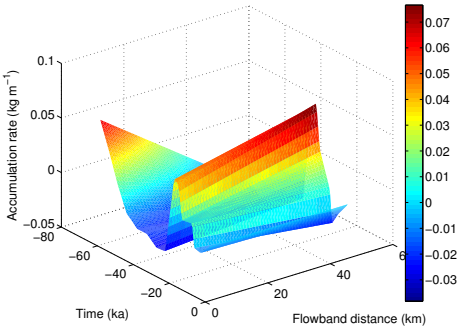

(e) Iteration 5

Figure 4.13: The difference between the recovered accumulation rate from the 5 iterations in Figure 4.12 and the synthetic accumulation rate in Figure 4.2.

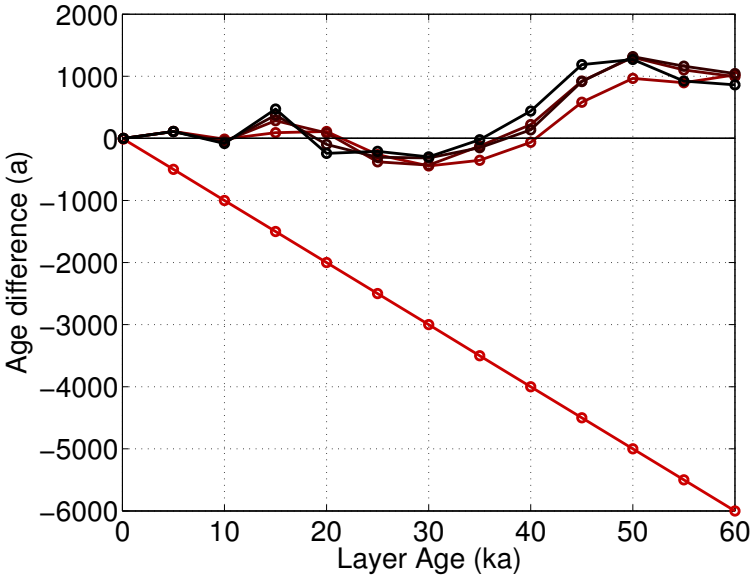

(a)

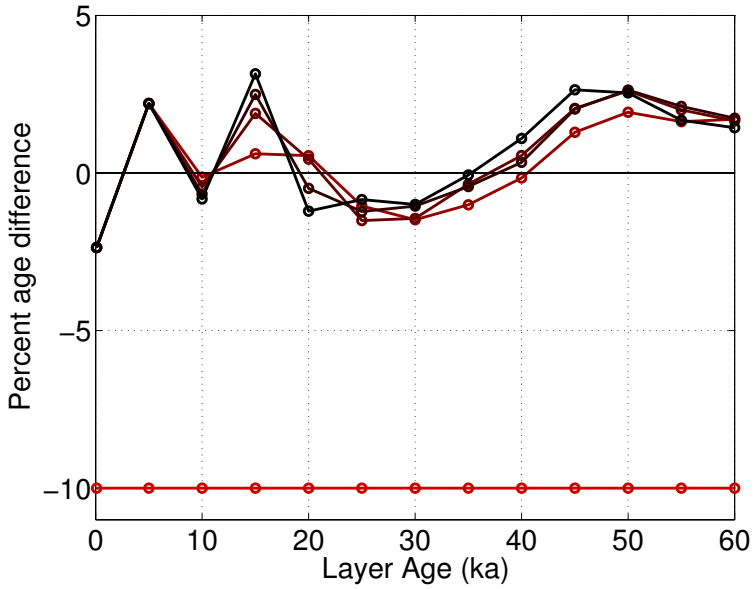

(b)

Figure 4.14: (a) The age difference between the true ages and the age updates from the dating from gas ages and delta-age. (b) The percent difference between the true ages and the age of ice, determined from the delta age and gas age. The percent difference for the first self-consistent iteration is 10% younger and the percent difference for iterations 2-5 is less than 3%.

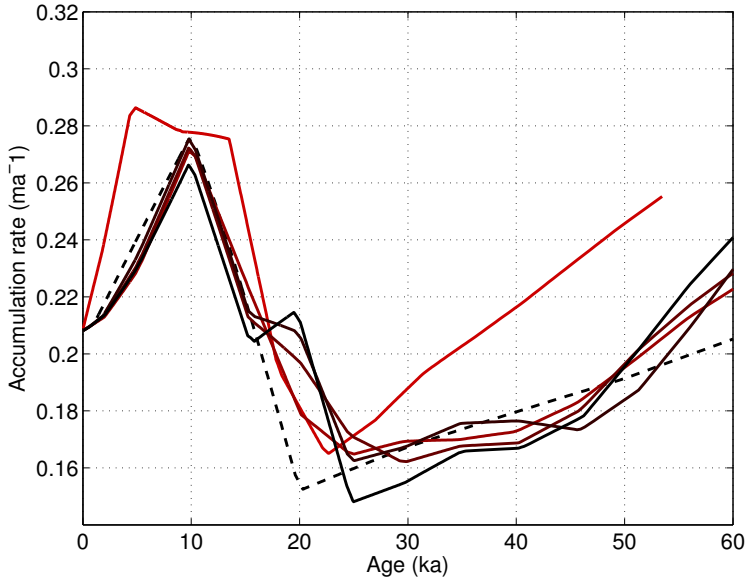

Figure 4.15: The synthetic accumulation rate at origin points of ice in the ice core (dashed black), and results from the self-consistent loop from the first iteration (light red) to the final iteration (dark red).

iterations bring the inferred values closer to the synthetic accumulation rate, with little improvement after the second iteration.

The bubble close-off ages for the self-consistent iterations are shown in Figure 4.16. The larger accumulation in the first iteration produces a smaller bubble close-off age. The second through fifth iterations are closer to the true bubble close-off age.

Results from the ice-core dating inverse problem are shown in Figure 4.17. The depth-age profile inferred from the inverse method is shown for all 5 iterations. The 5 inferred solutions are indistinguishable by eye and produce the same depth-age relationship of the sparse ice-ages.

Figure 4.18 shows a comparison between the true sparse ice ages and the ages of ice dated through noisy gas ages and delta-age. The gas ages include red noise based on 2% uncertainty of the age. All of the iterations have a difference between the true and inferred ice ages within 2.5% with insignificant improvement in subsequent model iterations. Here we find that the uncertainty in the gas-age data controls how well the self-consistent model

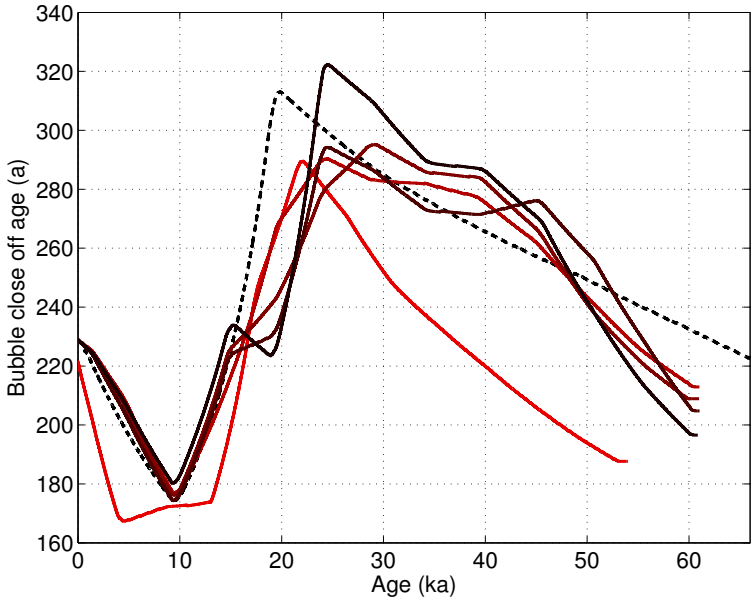

Figure 4.16: The bubble close-off results for the loop beginning with younger radar layers. The final bubble close-off result (light red) is near the synthetic bubble close-off (dashed black). Results from iterations transition color from light to dark red.

can fit the sparse age data for the ice. While uncertainty in delta-age is important, for a relatively warm, high-accumulation polar site, the delta-age and its uncertainty are small compared to the 2% uncertainty used for the gas ages.

Scenario (2) results

For scenario 2 we begin with radar layers that are 10% older than the correct layer ages. Figure 4.19 shows the spatial and temporal accumulation rate inferred from the inverse method for 5 iterations. The difference between the inferred accumulation rate and synthetic accumulation rate in Figure 4.20 shows that the inferred accumulation rate deviates from the synthetic accumulation rate.

The dating of the radar layers shows the greatest improvement in the first self-consistent iteration (Figure 4.31). The radar-layer ages for iterations 2-5 are under 4% different from the true age. As in scenario 1, the increase in the percent difference between the inferred age and the true age for older layers is due to the linear increase in the uncertainty from

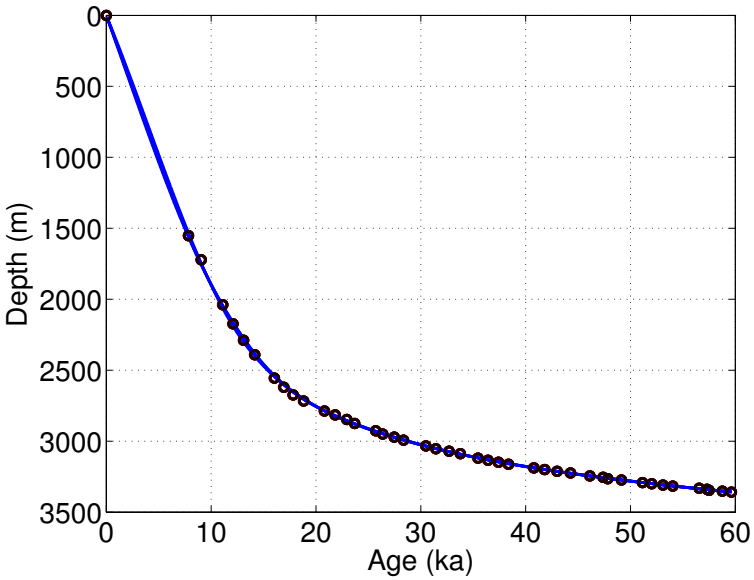

Figure 4.17: The complete depth-age curve of the ice core starting with radar layers younger than the true age. The depth age (blue) solutions from the inverse method for the 5 inferred solutions appear indistinguishable by eye at this scale. The ages of the ice inferred from the gas age and delta-age (circles) for the 5 iterations vary in color from light red to black, but appear indistinguishable at this scale.

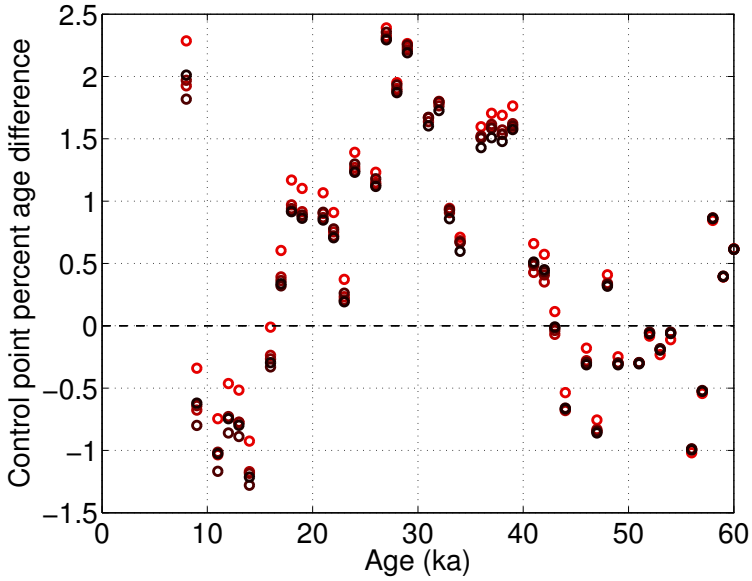

Figure 4.18: The difference between inferred age and true age at ice-core control points. Residual value color transitions from light red to dark for the five iterations. The difference between the true sparse ice age and the ice age inferred from noisy gas ages and delta-age is within 2.5%.

the gas-age control points.

The interpolated ice-core accumulation rate is shown in Figure 4.22. In the first iteration the accumulation rate is too low because we assumed the radar layers were older than the true age. The ice-core accumulation rate $\dot{b}_{core}$ from subsequent iterations is closer to the synthetic value, with little improvement after the first iteration.

The bubble close-off ages for the self-consistent iterations (determined in Box 2 of Figure 4.11) is shown in Figure 4.23. The first iteration produced a small accumulation rate (Figure 4.22), resulting in a greater age of the ice at bubble close-off. Iterations 2-5 are closer to the true bubble close-off age, with little improvement after the second iteration.

The continuous ice-core depth-age inferred from the inverse method (Box 4 of Figure 4.11) for the 5 iterations is shown in Figure 4.24. The sparse age points for the ice derived from the gas ages and calculated delta-age are shown for the five iterations. To better show the differences in the sparse ice ages from Figure 4.24, we show the percent difference between the inferred ages at control points and true ages at those points in Figure 4.25. The

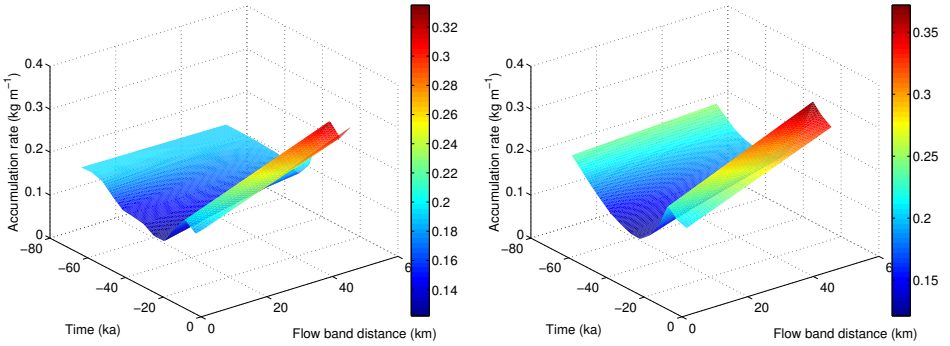

(a) Iteration 1

(b) Iteration 2

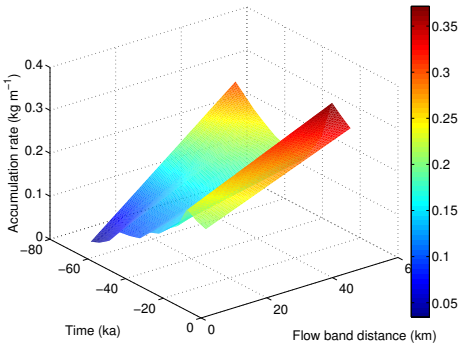

(c) Iteration 3

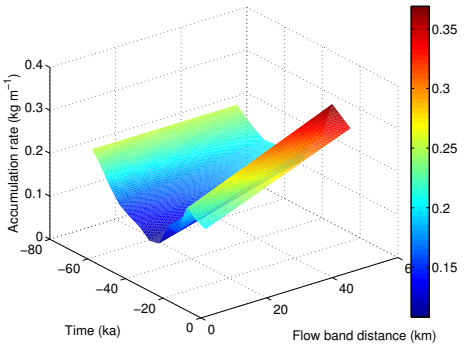

(d) Iteration 4

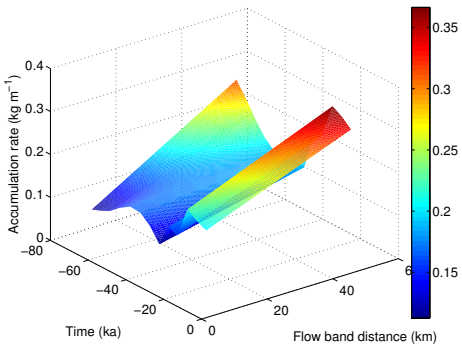

(e) Iteration 5

Figure 4.19: The spatial and temporal accumulation rate inferred from 5 iterations of the self-consistent loop, beginning with layer ages that are 10% older than the true layer ages.

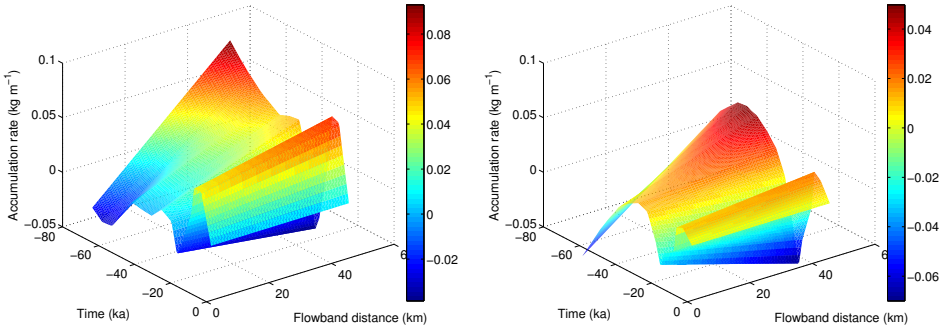

(a) Iteration 1

(b) Iteration 2

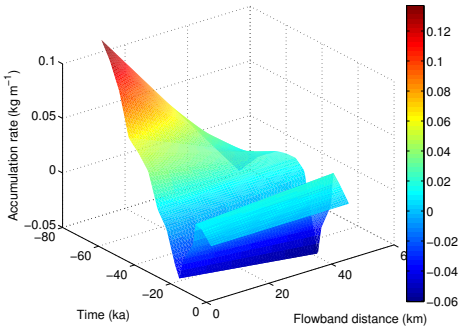

(c) Iteration 3

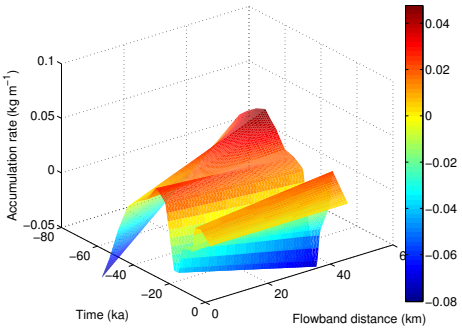

(d) Iteration 4

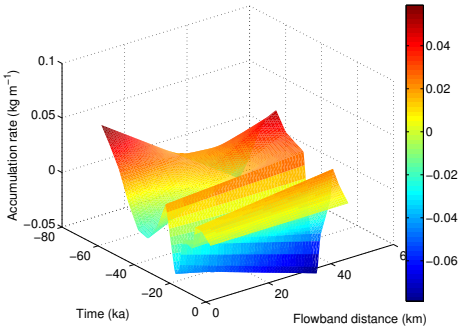

(e) Iteration 5

Figure 4.20: The difference between the recovered accumulation rate from the 5 iterations in Figure 4.19 and the synthetic accumulation rate in Figure 4.7.

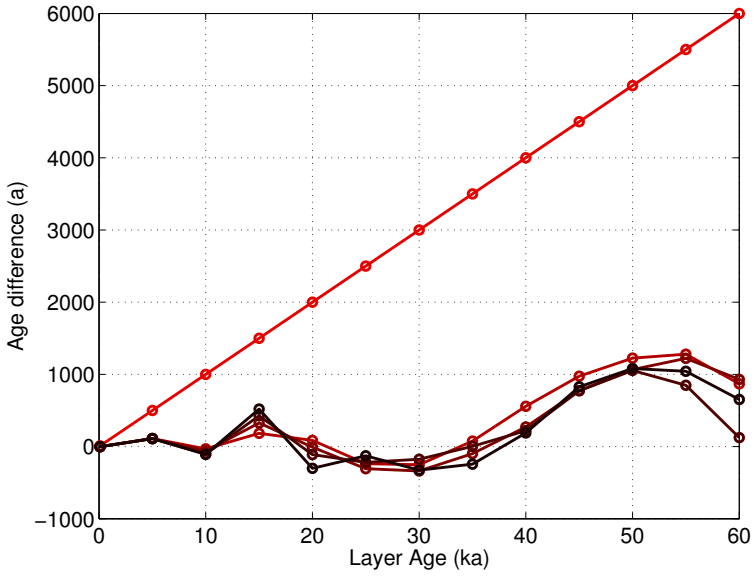

(a)

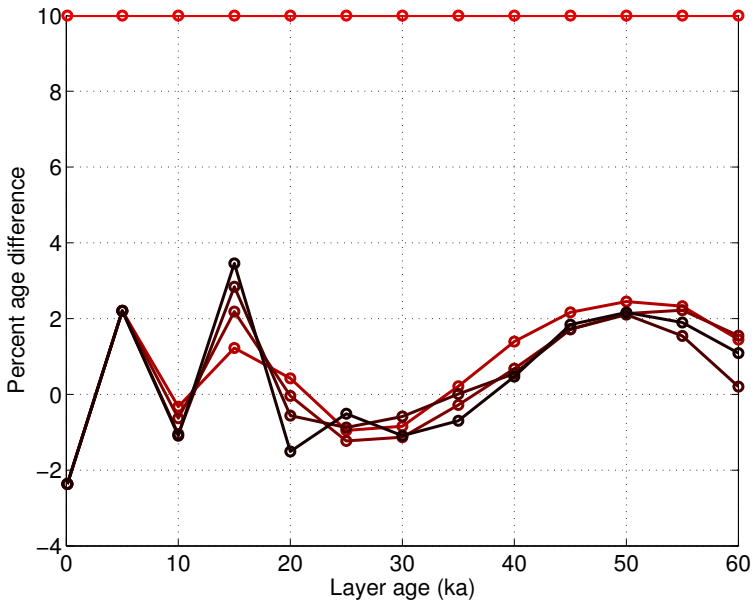

(b)

Figure 4.21: (a) The age difference between the true ages and the age updates from the dating from gas ages and delta-age. (b) The percent difference between the true ages and the age of ice, determined from the delta age and gas age. The percent difference for the first self-consistent iteration is 10% greater and the percent difference for iterations 2-5 is less than 4%.

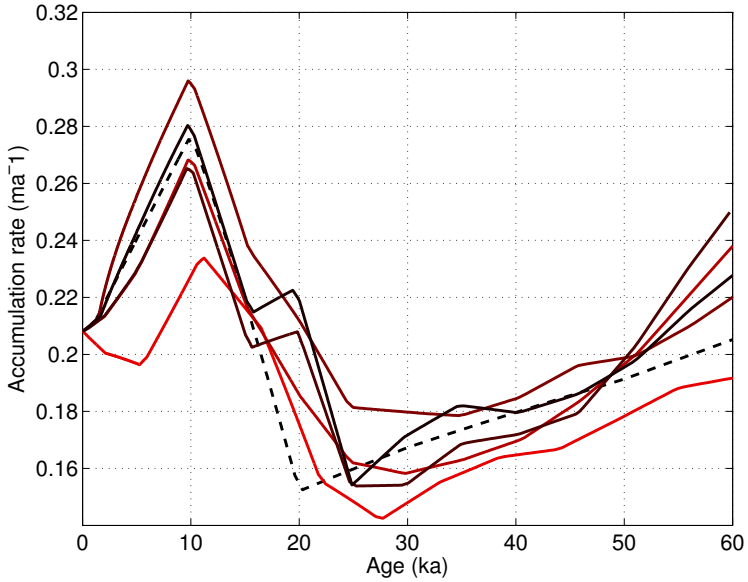

Figure 4.22: The accumulation rate for the ice core. The synthetic accumulation is dashed black. The first iteration accumulation rate is light red and subsequent iteration results are darker red.

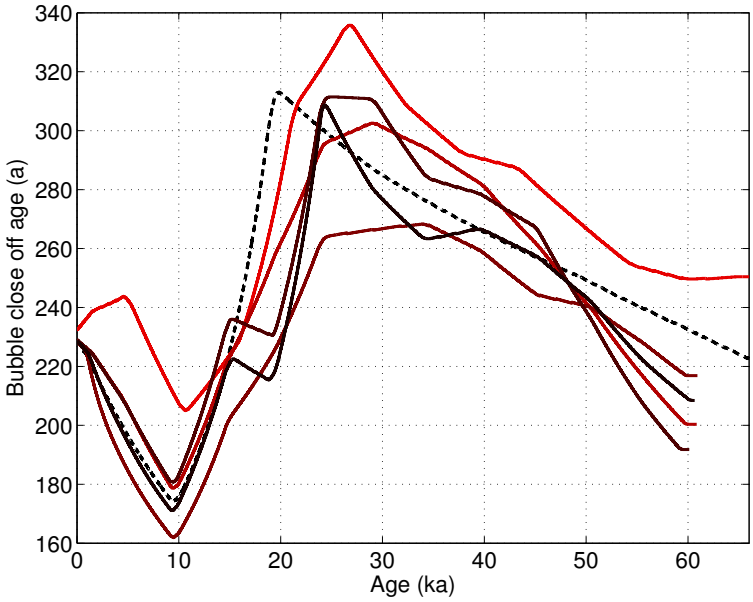

Figure 4.23: The bubble close-off results for the loop beginning with older radar layers. The final bubble close-off result (light red) is near the synthetic bubble close-off (dashed black). Results from iterations transition color from light to dark red.

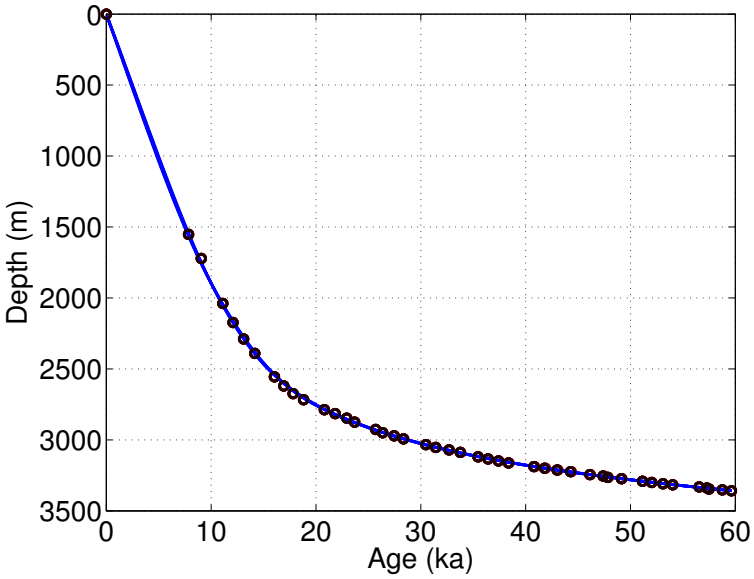

Figure 4.24: The depth age of the ice core starting with radar layers younger than the true age. The 5 inferred solutions for the depth age (blue) from the inverse method appear indistinguishable by eye at this scale. The ice ages inferred from the gas age and delta-age (circles) for the 5 iterations vary in color from light red to black, but appear indistinguishable at this scale.

percent difference between the inferred ages and the true ages of the ice are within 2.5%. Through the self-consistent method we are able to predict the age of the ice within 2.5% despite the uncertainty in the gas age (2%) and accumulation rate with error transferred from the uncertainty radar layer depths. With different realizations of red noise on the radar layers and gas ages, we would expect different patterns in the percent difference.

Koutnik [2009] and *Waddington et al.* [2007] show the resolving power of the 2-d inverse procedure decreases for the older radar layers and with distance from the divide. We do not formally show the resolving power of the inverse method, which requires calculation of impulse functions, similar to spike model tests described in Appendix F, with the difference that this is for a non-linear inverse problem, where as Appendix F is for a linear inverse problem. The resolving power is not formally shown in this work and would follow a procedure similar to previous work [*Koutnik*, 2009].

Results from scenario 1 and 2 show that the second self-consistent iteration is sufficient

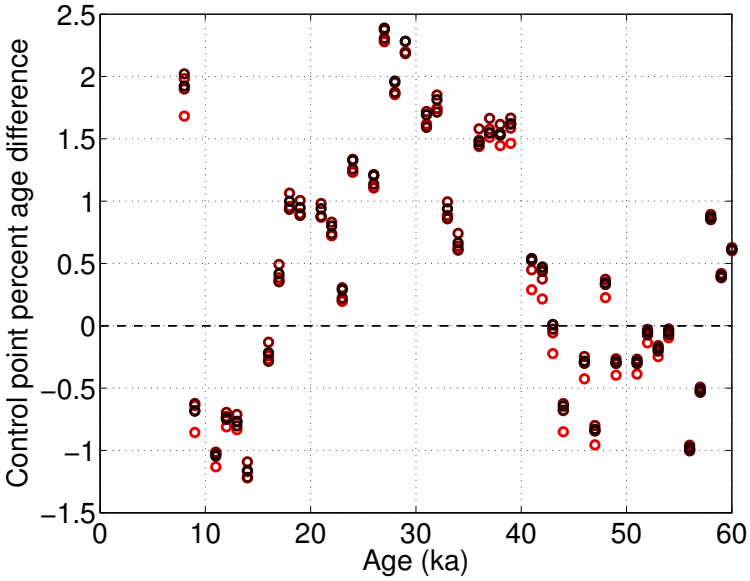

Figure 4.25: The age difference between inferred and true ice-core control points. Residual value color transitions from light red to dark for the five iterations. The difference between the true sparse ice age and the ice age inferred from noisy gas ages and delta-age are within 2.5%.

for both dating the ice core and radar layers, and estimating the past ice-sheet accumulation. Subsequent self-consistent iterations do not improve the inferred solutions.

In addition to the two scenarios shown here with radar-layer ages at 10% greater and less than the true radar layers, experiments were performed with initial estimates of radar-layer ages 20% greater than and less than the actual ages. The results were similar to the results shown here; in the second iteration, the inferred radar ages were within 2% of the actual ages.

To test how much the uncertainty in the gas ages affects the depth-age solutions for the sparse ice ages and radar layers, we assume a 1-σ uncertainty of the gas age equal to 0.5%. Residuals for the radar layer and sparse ice ages are smaller than when the gas age uncertainty is 2%. The residuals with the gas age uncertainty at 0.5% are within 1%. Because the residuals are not within 0.5%, deviations in the accumulation rate, translated through the delta-age, make the residuals greater than the uncertainty in the age. In the case that the gas age uncertainty is 2%, the delta-age error is small relative to the gas age

error.

4.4.2 Results for a smoothly varying synthetic accumulation

Scenarios (3) and (4) use data with a smoothly varying accumulation-rate history (Figure 4.7). Because the abrupt changes in scenario 1 produced relatively large mismatches, these new scenarios are designed to determine how well the inverse problem can recover an accumulation rate that varies smoothly in time and space.

Scenario (3) results

In Scenario (3), the radar layers are initially assumed to be 10% younger than the true ages. The difference between the true ages and inferred radar-layer ages for 5 iterations is shown in Figure 4.26(a). The percent difference in age of the radar layers is shown in Figure 4.26(b). Similar to scenarios (1) and (2), there is insignificant improvement in the layer dating after the second iteration. Iterations 2-5 are all within 6% of the true radar-layer ages.

The ice-core accumulation rate is shown in Figure 4.27. The accumulation rate for the first iteration is higher than the synthetic value because we assume the radar-layer ages are younger than the true ages. Subsequent iterations are closer to the synthetic value. Figure 4.28 shows the bubble close-off for the five iterations. The bubble close-off is small for the first iteration due to the higher accumulation rate. Subsequent iterations are closer to the synthetic bubble close-off. The depth-age profile of the ice core in Figure 4.29, is inferred from sparse gas-age data. Figure 4.30 shows the residual between the true and inferred gas-ages. The residual values are less than 2.5%.

Scenario (4) results

In Scenario (4) the radar layers are initially assumed to be 10% older. The age difference between the true and inferred radar-layer ages is shown in Figure 4.31(a). The percent difference is shown in Figure 4.31(b). Figure 4.32 shows the interpolated ice-core accumulation rate. The bubble close-off age is shown in Figure 4.33. Figure 4.34 shows the ice-core

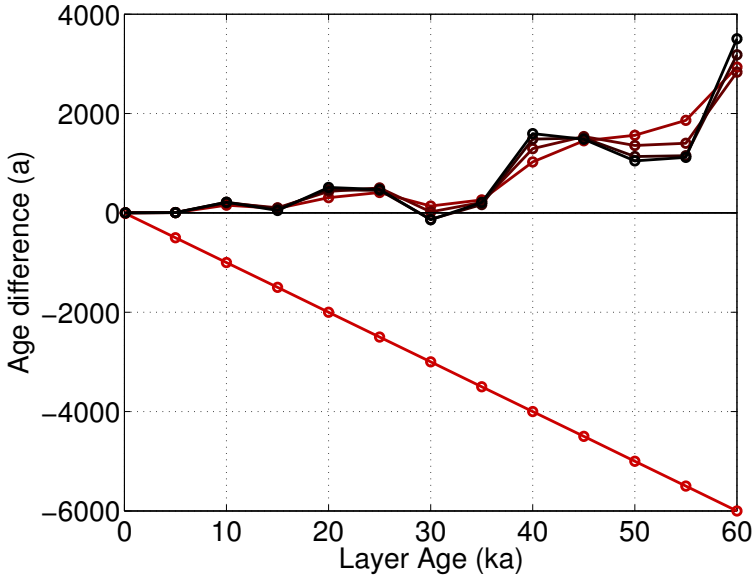

(a)

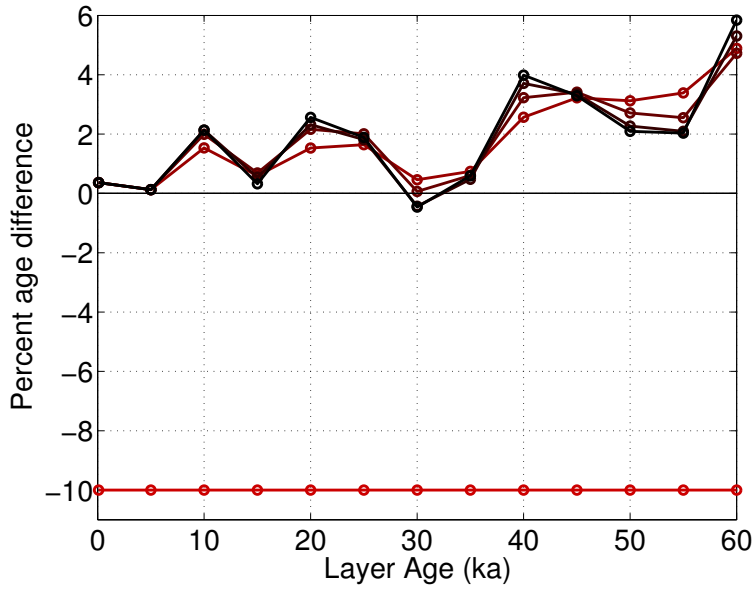

(b)

Figure 4.26: (a) The age difference between the true ages and the age updates from the dating from gas ages and delta-age. (b) The percent difference between the true ages and the age of ice, determined from the delta age and gas age. The percent difference for the first self-consistent iteration is 10% and the percent difference for iterations 2-5 is less than 6%.

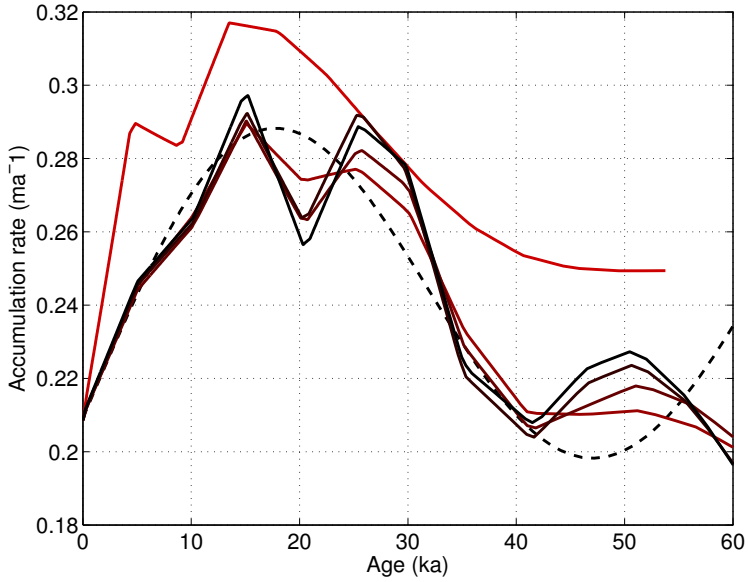

Figure 4.27: The accumulation rate for the ice core. The synthetic accumulation is dashed black. The first iteration accumulation rate is light red and subsequent iteration results are darker red.

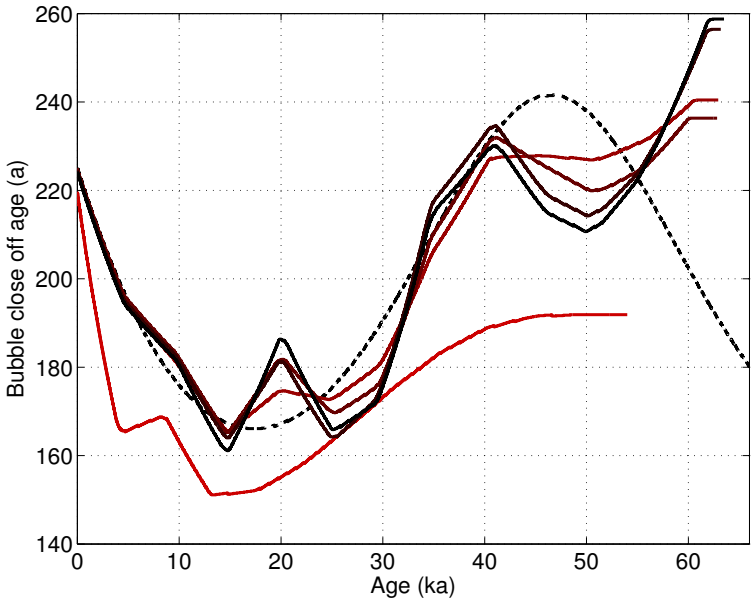

Figure 4.28: The bubble close-off results for the loop beginning with younger radar layers. The final bubble close-off result (light red) is near the synthetic bubble close-off (dashed black). Results from iterations transition color from light to dark red.

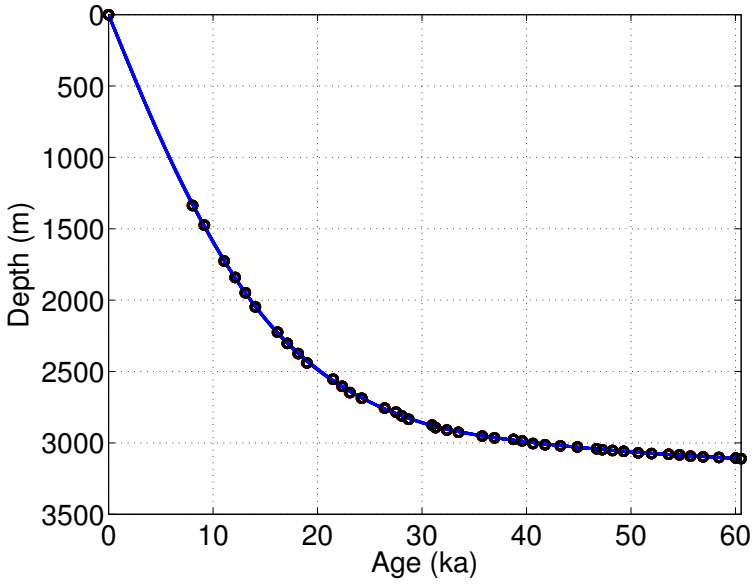

Figure 4.29: The depth age of the ice core starting with radar layers younger than the true age. The 5 inferred solutions for the depth age (blue) from the inverse method appear indistinguishable by eye at this scale. The ice ages inferred from the gas age and delta-age (circles) for the 5 iterations vary in color from light red to black, but appear indistinguishable at this scale.

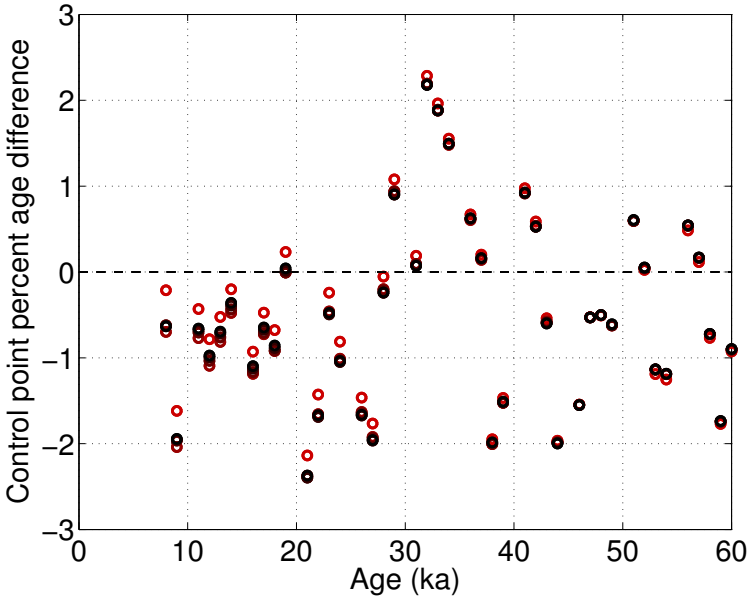

Figure 4.30: The age difference between inferred and true ice-core control points. Residual value color transitions from light red to dark for the five iterations. The difference between the true sparse ice age and the age of ice determined from noisy gas ages and delta-age is mostly within 2%.

depth-age relationship determined from sparse ages of ice, inferred from the delta-age and gas-age. The difference between the true and inferred ages of ice is shown in Figure 4.35 shows the difference is less than 2.5%.

4.5 Discussion and conclusions

The four scenarios with incorrect initial radar-layer ages rule out the possibility that the self-consistent method is sensitive to the initial estimate for the layer ages. By using other initial estimates, including 20% greater and less than the correct layer ages, I found similar results; only 2 iterations are necessary to improve the estimates of the layer ages, ice-core ages and delta-age.

We find that the self-consistent method requires 2 iterations to recover different synthetic accumulation rates, with sharp corners in scenarios (1) and (2) and a smooth sine function in Scenarios (3) and (4). That is, our regularization method that minimizes the spatial and temporal smoothness of the accumulation rate history does not require additional iterations when the synthetic accumulation rate has abrupt changes, as in the Figure 4.2 accumulation rate used in scenarios (1) and (2). However, the abrupt changes in the accumulation rate cannot be recovered.

Using gas-age uncertainties of 0.5% of the age allows a tighter constraint on the sparse ice ages and layer ages. This also provides an improved estimate of the ice-core accumulation rate and delta-age. The uncertainty in the gas ages is an important constraint on the self-consistent model.

The self-consistent method described here demonstrates that the modules can be combined to provide a depth-age relationship for an ice core and radar layers, and the procedure incorporates physically reasonable histories of accumulation and ice dynamics. We use synthetic data to establish the method, and show that we can converge on the correct depth-age relationship and a suite of histories for accumulation-rate, delta-age and ice dynamics.

The self-consistent method is not limited to the scope presented here; rather, we present an idea about how models can be combined to get the full richness of several datasets in unison. There are several ways that this self-consistent method can be modified.

(1) Modules using one physical description can be replaced with other modules that capture

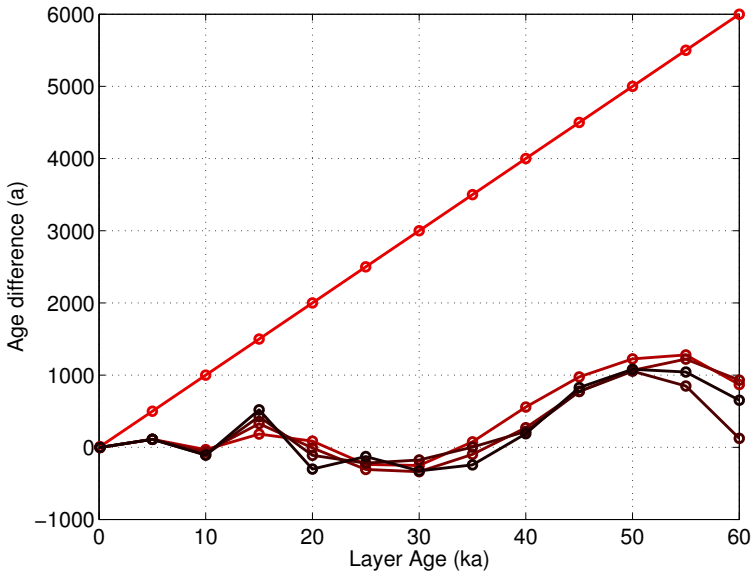

(a)

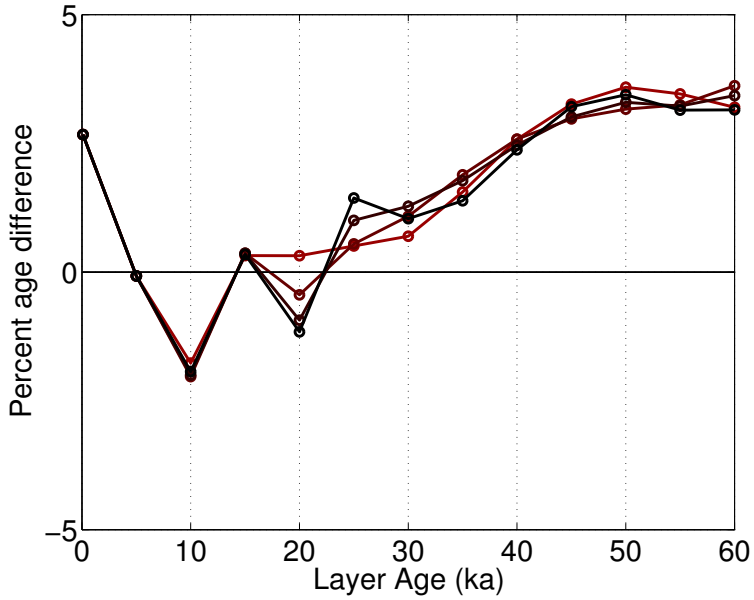

(b)

Figure 4.31: (a) The age difference between the true ages and the age updates from the dating from gas ages and delta-age. (b) The percent difference between the true ages and the age of ice, determined from the delta age and gas age. The percent difference for the first self-consistent iteration is 10% greater and the percent difference for iterations 2-5 is less than 5%.

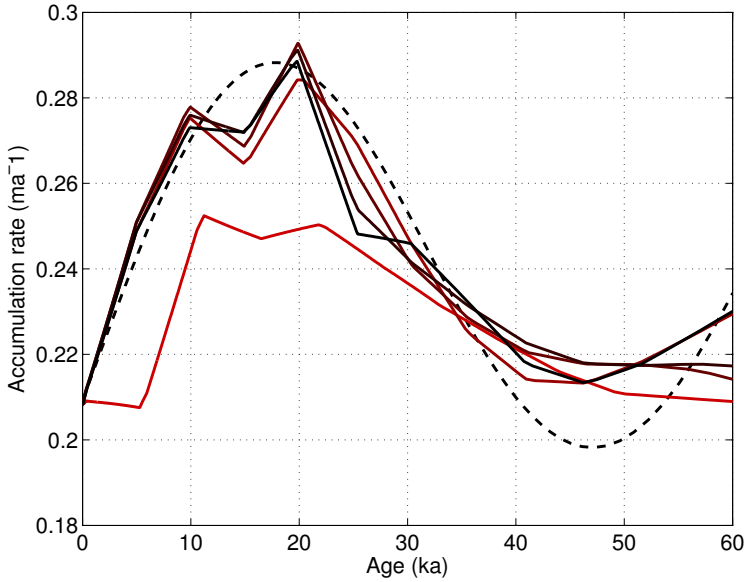

Figure 4.32: The accumulation rate for the ice core. The synthetic accumulation is dashed black. The first iteration accumulation rate is light red and subsequent iteration results are darker red.

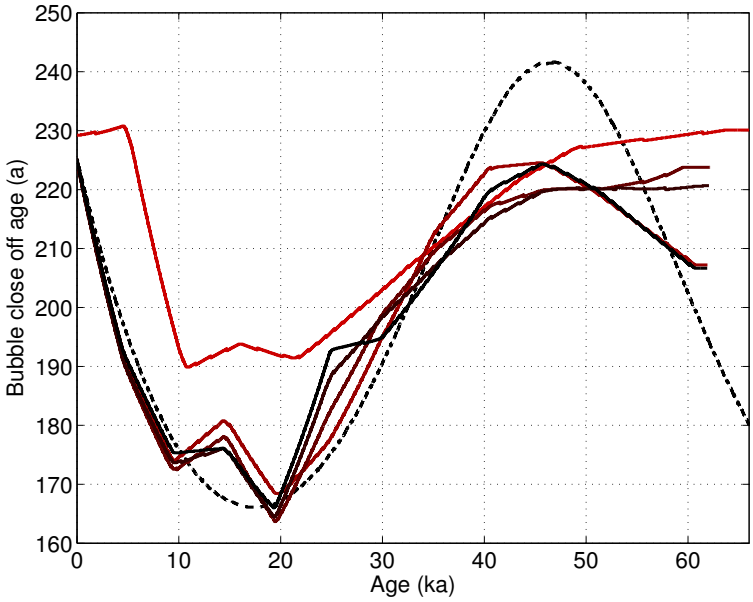

Figure 4.33: The bubble close-off results for the loop beginning with older radar layers. The final bubble close-off result (light red) is near the synthetic bubble close-off (dashed black). Results from iterations transition color from light to dark red.

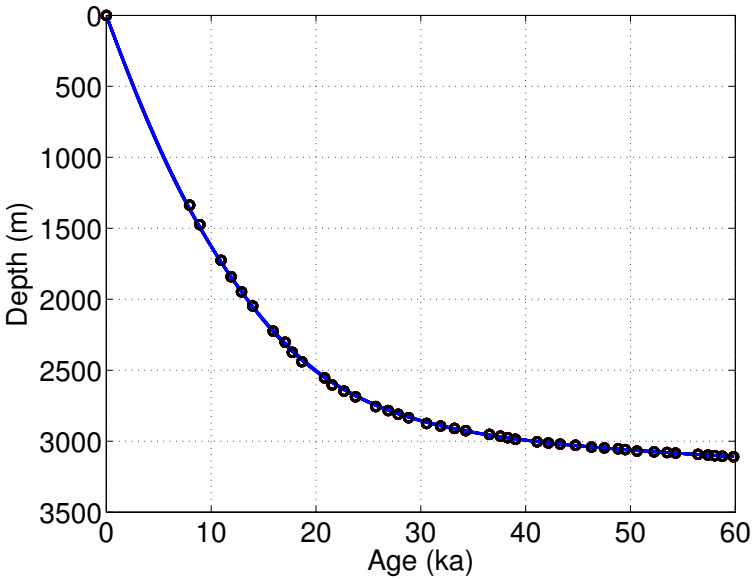

Figure 4.34: The complete depth-age of the ice core starting with radar layers older than the true age. The depth age (blue) from the 5 iterations for the inverse method appear indistinguishable by eye at this scale. The age of the ice inferred from the gas age and delta-age (circles) for the 5 iterations vary in color from light red to black, but appear indistinguishable at this scale.

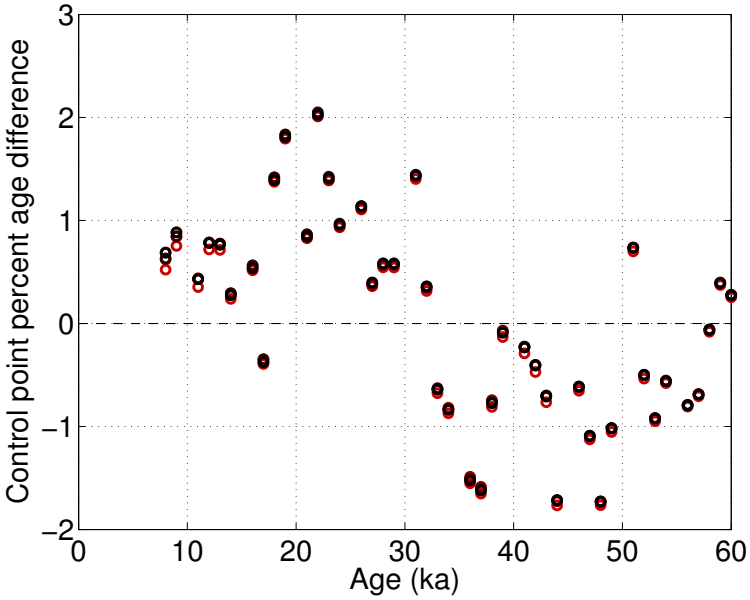

Figure 4.35: The percent difference between inferred and true ice-core control-points ages. Residual-value color transitions from light red to dark for the five iterations. The difference between the true sparse ice age and the ice age inferred from noisy gas ages and delta-age is mostly within 2.5%.

different dominant processes, as is appropriate for the site.
(2) Additional model parameters can be included in the inverse procedure. Previous inverse procedures solved for the surface elevation $S(x,t)$. We prescribed a surface evolution and did not solve for this parameter, due to computational limitations. Solving for the thickness history is important for determining the ice-sheet evolution.
(3) Different data or more data can play an important role in constraining the solution. Depending on the confidence in different data, we could use a combination of data sources to constrain the problem. In this work we use an analytic temperature field, as opposed to including heat transfer in a thermo-dynamic model. The current temperature profile can add another useful constraint to the problem. Furthermore, weighting can be transferred to the 'best' data. Annual layer counting using physical and chemical methods offers the most accurate dating with the lowest uncertainty. At the depth where layer counting is no longer viable, sparse control points tie discrete depth-age dating to other chronologies including methane records from other ice cores and cave speleothems. Ice-flow models are useful for determining a continuous depth-age between sparse control points.

We recognize that there are limitations to this method. Because we are using synthetic data generated with the same physics, we avoid the problem of inappropriate physics contributing error to this work; however, we recognize that this method assumes that the ice-deformation models for firn densification and ice flow are perfect and we do not include errors in the forward models as part of the method. When this method is applied to observation-based data, the modeling errors will need to be considered, in addition to errors in the inferred solutions, including the accumulation rate and delta-age.

Chapter 5

CONCLUSIONS

5.1 Summary

This work links several physical processes, approximated by numerical methods in modular units, into one self-consistent glaciological model. The modules have been developed and combined in a way that recognizes that the processes are not independent, even though they may have different characteristic temporal and spatial scales. The self-consistent model is greater than the sum of its parts. Climate histories, which are generally measured directly or inferred numerically, can affect different processes. For example, the surface temperature can be reconstructed using borehole thermometry or stable isotopes. The temperature reconstruction is important for small-scale and large-scale processes, including grain growth and internal deformation of the ice sheet (from changes in the temperature-dependent viscosity).

In Chapter 1, I introduced the idea of the self-consistent method to combine modules and a variety of data to answer important lines of research in glaciology, including determination of the past geometry of polar ice sheets and further refinement of the chronology of ice cores and radar isochrones.

Chapter 2 motivated the need for a robust dating scheme for ice cores using a physically based approach, and presented an inverse method, paired with a 1-d ice-flow model to determine a continuous ice-core chronology from sparse data. The physically based inverse approach is more in line with thinking like an ice sheet, and we show this is a better way to determine the depth-age relationship than linear and spline interpolations of sparse data.

In Chapter 3 I developed a new model for firn densification, coupled with grain growth and heat transfer. I applied the model to the preliminary WAIS D accumulation and temperature record for the last 2000 years. I found that the results agreed with gas lock-in depths based on Kr and N isotopes [*Orsi*, 2011].

Chapter 4 presented the synthesis of the previous chapters, that is the self-consistent method, which incorporates several modules into one model. First, a 2-d kinematic flowband forward model is paired with an inverse problem to determine the past spatial history of accumulation rates. Then, these accumulation-rate histories are input for a firn-densification model that determines delta-age, the gas-age ice-age offset. By assuming that sparse gas ages (for example, control points from methane) are accurate, then dated an ice core, and radar-detected layers where they intersect the ice core. The redated radar layers allow us to return to the first step, and rederive spatial patterns of past accumulation rate and ice-sheet geometry, including ice thickness and divide position. The loop continues until the accumulation-rate patterns and the ages no longer change.

New work presented in this thesis includes the development of an inverse procedure to determine a robust ice-core chronology, a Lagrangian firn-densification model incorporating grain growth and heat transfer to determine delta-age, and a self-consistent method, to piece together several different modular units into a consistent description of the past ice sheet geometry and dating. The self-consistent method is distinguished from previous work [*Lemieux-Dudon et al.*, 2010], by inclusion of a Frequentist statistical framework, which does not require *a priori* knowledge of solutions, as is required in a Bayesian framework. This method focuses on the accumulation rate and dating of one ice core and assumes that gas-age dating is correct. The self-consistent method is generally designed to take the most appropriate data constraints and models for the site.

We developed a Frequentist-based self-consistent method, to rigorously use ice-deformation physics at a range of spatial and temporal scales to determine a robust depth-age relationship for the ice core and radar layers, while determining an accompanying spatial and temporal accumulation-rate pattern.

There are challenges in the methods developed here. Forward models are approximations for physical processes. There are errors that are not easy to quantify. In inverse methods, it is difficult to quantify the errors from inadequacies of the models and the model parameters. Inverse problems are powerful tools for inferring model parameters, which can be coefficients, boundary conditions and initial conditions; however, there are potential problems with existence, uniqueness, and stability, and these problems are greater for non-linear problems.

5.2 Future work

Ice-flow modeling is useful for dating ice below where layer counting is no longer possible, and to expose problems or ambiguities in layer counting. Continued effort is necessary to refine and improve chronologies, and to reconstruct the past ice-sheet configurations. Future work includes making use of improved computational processing resources, and improved physical and computation theory that allows the reduction of computational time. Improved laboratory techniques are providing high-resolution measurements of chemistry, isotopes and gases, which will reduce the need for model-based dating. However, models will still be needed to infer past conditions and to predict possible future conditions. For example, when the temporal resolution of gas dating reduces the need of modeling to infer a depth-age relationship, we still need models to infer past ice-sheet thickness (and volume) and ice-divide migration, which are the product of past dynamical processes. In addition, the spatial and temporal pattern of past accumulation rate is needed to provide input or constraints for global climate models. Further, with a known accumulation-rate history, the temperature history can be inferred using bubble-number densities [*Spencer et al.*, 2006] and this temperature reconstruction can be used to check temperature reconstructions from oxygen isotopes and borehole thermometry.

We also expect that the self-consistent model will be even more useful as new technology emerges. For example, the proposed Rapid Access Ice Drill (RAID) could provide sparse depth-age data through dating of dust layers [*Bay et al.*, 2006] seen in the borehole. If successful, the RAID, in combination with the self-consistent model, would provide a means to increase the spatial extent of well-dated stratigraphy in ice sheets.

The self-consistent method described here is designed to infer histories of the spatial pattern of accumulation rates and of delta ages, and to produce self-consistent dates for ice cores and radar layers. The modules could be modified and expanded to incorporate more data and to include more complex processes in the forward models. This work a proof of concept, demonstrating that the approach is achievable and useful for providing a self-consistent view of ice-sheet evolution.

Specific future work remains to develop improved modular units:

1) the firn model should be extended to use time steps smaller than one year. Currently the model does not incorporate physics to reflect the seasonal variability in density that is observed in firn cores. Inclusion of that density variability should further reduce uncertainty in the delta-age result.
2) The inverse problem in which I infer the spatial and temporal patterns of accumulation rate currently uses kinematic particle tracking within a prescribed surface-evolution history, which was obtained from the dynamically-based forward model that created the synthetic data.. Future work should include a dynamically based forward method within the inverse problem, to allow a transient surface height and divide migration. This may require additional data to further constrain the divide migration and surface elevation through time. Additional constraints could be to prescribe the thickness history or to limit the rate of change of the surface elevation.

Now that the method has been shown to work with synthetic data, in future work I will use observations from existing ice cores and ice-penetrating radar surveys. Potential core sites include Summit, Greenland, and WAIS Divide in Antarctica. Summit is an ideal site because much is known about the site. WAIS Divide has potential to provide a high-resolution chronology for the past 60 ka. This chronology should be useful for improving dating of other Antarctic cores.

The self-consistent model provides a framework for virtual ice cores, where the radar layers spatially extend the ice-core information and enhance the value of the time and labor-intensive ice-core information. Boundary conditions, initial conditions, and physical properties including accumulation rate, thinning function, and layer thicknesses, may be determined for a virtual ice core anywhere along the flow path. The temporal resolution is unlikely to rival an ice-core dataset, but the rapid availability and reduced cost of modeling to provide a substitute promise to be useful.

For future site-selection work, the self-consistent model is a promising tool to infer information about the past climate at a potential ice-core location with information entirely collected at the surface of the ice sheet, including dated radar layers, the modern accumulation rate, thickness, temperature and horizontal velocity.

The self-consistent model promises to guide improvements in field observations, including

spatial and temporal sampling of data. Inverse modeling helps us to predict the resolution and uncertainty of the modeled parameters, based on an estimate of the data and data uncertainty. If a particular uncertainty or sampling interval is required to provide a coherent model solution at an adequate resolution and uncertainty, this information is valuable for designing an experiment and guiding the field campaign before lacing up the field boots. Providing the best modeling that the current computational resources and theory allow enhances field observations and allows us to get the greatest advancement from limited resources.

5.3 Implications

Improvements from the self-consistent method will help to further refine existing chronologies, while allowing us to more accurately infer the past accumulation rate and ice dynamics. Ice-core chronologies undergo continuous revision, as physical modeling and observation techniques improve, acting to improve precision and reducing uncertainty. This work demonstrates that a more integrated approach can determine the most accurate solutions, and that can ensure these solutions fit with the rest of the ice-sheet portrait.

BIBLIOGRAPHY

Alley, R. B., Flow-law hypotheses for ice-sheet modeling, *Journal of Glaciology*, *38*, 245–256, 1992.

American Meteorogical Society, *Glossary of Meteorology*, 2nd ed., Allen Press, Boston, MA, 2000.

Andersen, K. K., et al., High-resolution record of Northern Hemisphere climate extending into the last interglacial period, *Nature*, *431*(7005), 147–151, doi:10.1038/nature02805, 2004.

Andersen, K. K., et al., The Greenland ice core chronology 2005, 15–42ka. part 1: constructing the time scale, *Quaternary Science Reviews*, *25*(23-24), 3246–3257, doi: 10.1016/j.quascirev.2006.08.002, 2010.

Arnaud, L., J.-M. Barnola, and P. Duval, Physical modeling of the densification of snow/firn and ice in the upper part of polar ice sheets, *Physics of Ice Core Records*, pp. 285–305, 2000.

Arthern, R. J., and D. J. Wingham, The natural fluctuations of firn densification and their effect on the geodetic determination of ice sheet mass balance, *Climatic Change*, *40*(3-4), 605–624, doi:10.1023/A:1005320713306, 1998.

Arthern, R. J., D. G. Vaughan, A. M. Rankin, R. Mulvaney, and E. R. Thomas, In situ measurements of Antarctic snow compaction compared with predictions of models, *Journal of Geophysical Research*, *115*(F3), doi:10.1029/2009JF001306, 2010.

Aster, R. C., C. H. Thurber, and B. Borchers, *Parameter estimation and inverse problems*, Elsevier Academic Press, Boston, 2005.

Barnola, J.-M., P. Pimienta, D. Raynaud, and Y. S. Korotkevich, CO2-climate relationship as deduced from the Vostok ice core: a re-examination based on new measurements and on

a re-evaluation of the air dating, *Tellus B*, *43*(2), 83–90, doi:10.1034/j.1600-0889.1991.t01-1-00002.x, 1991.

Battle, M. O., J. P. Severinghaus, E. D. Sofen, D. Plotkin, A. J. Orsi, M. Aydin, S. A. Montzka, T. Sowers, and P. P. Tans, Controls on the movement and composition of firn air at the West Antarctic Ice Sheet Divide, *Atmospheric Chemistry and Physics Discussions*, *11*(6), 18,633–18,675, doi:10.5194/acpd-11-18633-2011, 2011.

Bay, R. C., N. E. Bramall, P. B. Price, G. D. Clow, R. L. Hawley, R. Udisti, and E. Castellano, Globally synchronous ice core volcanic tracers and abrupt cooling during the last glacial period, *Journal of Geophysical Research*, *111*(D11), doi:10.1029/2005JD006306, 2006.

Blunier, T., and E. J. Brook, Timing of millennial-scale climate change in Antarctica and Greenland during the last glacial period, *Science*, *291*(5501), 109–112, 2001.

Bogorodskii, V. V., C. R. Bentley, and P. E. Gudmandsen, *Radioglaciology*, D. Reidel Publishing Co., Dordrecht, Holland, 1985.

Broecker, W. S., Paleocean circulation during the last deglaciation: a bipolar seesaw?, *Paleoceanography*, *13*, 119, doi:10.1029/97PA03707, 1998.

Brook, E. J., J. W. C. White, A. S. M. Schilla, M. L. Bender, B. Barnett, J. P. Severinghaus, K. C. Taylor, R. B. Alley, and E. J. Steig, Timing of millennial-scale climate change at Siple Dome, West Antarctica, during the last glacial period, *Quaternary Science Reviews*, *24*(12-13), 1333–1343, doi:10.1016/j.quascirev.2005.02.002, 2005.

Buchardt, S. L., and D. Dahl-Jensen, Estimating the basal melt rate at North GRIP using a Monte Carlo technique, *Annals of Glaciology*, *45*, 137–142, doi:10.3189/172756407782282435, 2007.

Buizert, C., et al., Gas transport in firn: multiple-tracer characterisation and model intercomparison for NEEM, Northern Greenland, *Atmospheric Chemistry and Physics Discussions*, *11*(5), 15,975–16,021, doi:10.5194/acpd-11-15975-2011, 2011.

Caillon, N., Timing of atmospheric CO2 and Antarctic temperature changes across termination III, *Science*, *299*, 1728–1731, doi:10.1126/science.1078758, 2003.

Coble, R. L., Diffusion models for hot pressing with surface energy and pressure effects as driving forces, *Journal of Applied Physics*, *41*, 4798, doi:10.1063/1.1658543, 1970.

Cogley, J. G., et al., *Glossary of Glacier Mass Balance and Related Terms*, vol. IACS Contribution No. 2, 86, IHP-VII Technical Documents in Hydrology, UNESCO-IHP, Paris, 2011.

Conway, H., and L. A. Rasmussen, Recent thinning and migration of the Western Divide, central West Antarctica, *Geophysical Research Letters*, *36*(12), doi:10.1029/2009GL038072, 2009.

Conway, H., et al., Proposed drill site near the Ross-Amundsen ice divide, West Antarctica, *Tech. rep.*, University of Washington, 2005.

Cuffey, K., and W. S. B. Paterson, *The physics of glaciers*, 4th ed., Butterworth-Heinemann/Elsevier, Burlington, MA, 2010.

Cuffey, K. M., and G. D. Clow, Temperature, accumulation, and ice sheet elevation in central Greenland through the last deglacial transition, *Journal of Geophysical Research*, *102*(C12), 26,383–26,396, doi:10.1029/2001JD000672, 1997.

Dahl-Jensen, D., K. Mosegaard, N. Gundestrup, G. D. Clow, S. J. Johnsen, A. W. Hansen, and N. Balling, Past temperatures directly from the Greenland ice sheet, *Science*, *282*(5387), 268–271, doi:10.1126/science.282.5387.268, 1998.

Dansgaard, W., and S. J. Johnsen, A flow model and a time scale for the ice core from Camp Century, Greenland, *Journal of Glaciology*, *8*(53), 215–223, 1969.

EPICA members, Eight glacial cycles from an Antarctic ice core, *Nature*, *429*(6992), 623–628, doi:10.1038/nature02599, 2004.

Freitag, J., F. Wilhelms, and S. Kipfstuhl, Microstructure-dependent densification of polar firn derived from X-ray microtomography, *Journal of Glaciology*, *50*, 243–250, doi: 10.3189/172756504781830123, 2004.

Fudge, T. J., K. C. Taylor, H. Conway, E. D. Waddington, and K. C. McGwire, WDC06A-5; an initial chronology for the West Antarctic Ice Sheet Divide ice core from electrical measurements, AGU fall meeting abstract, 2011.

Fujita, S., J. Okuyama, A. Hori, and T. Hondoh, Metamorphism of stratified firn at Dome Fuji, Antarctica: a mechanism for local insolation modulation of gas transport conditions during bubble close off, *Journal of Geophysical Research*, *114*(F3), doi: 10.1029/2008JF001143, 2009.

Goujon, C., J.-M. Barnola, and C. Ritz, Modeling the densification of polar firn including heat diffusion: application to close-off characteristics and gas isotopic fractionation for Antarctica and Greenland sites, *Journal of Geophysical Research*, *108*(D24), doi: 10.1029/2002JD003319, 2003.

Gow, A. J., D. A. Meese, and R. W. Bialas, Accumulation variability, density profiles and crystal growth trends in ITASE firn and ice cores from West Antarctica, *Annals of Glaciology*, *39*, 101–109, doi:10.3189/172756404781814690, 2004.

Hansen, P. C., Analysis of discrete ill-posed problems by means of the L-curve, *SIAM Review*, *34*(4), 561, doi:10.1137/1034115, 1992.

Hansen, P. C., *Rank-deficient and discrete ill-posed problems: numerical aspects of linear inversion*, SIAM, Philadelphia, 1998.

Hawley, R. L., E. D. Waddington, R. B. Alley, and K. C. Taylor, Annual layers in polar firn detected by borehole optical stratigraphy, *Geophysical Research Letters*, *30*(15), doi: 10.1029/2003GL017675, 2003.

Helsen, M. M., M. R. van den Broeke, R. S. W. van de Wal, W. J. van de Berg, E. van Meijgaard, C. H. Davis, Y. Li, and I. Goodwin, Elevation changes in Antarc-

tica mainly determined by accumulation variability, *Science*, *320*(5883), 1626–1629, doi: 10.1126/science.1153894, 2008.

Herron, M., and C. Langway, Firn densification: an empirical model, *Journal of Glaciology*, *25*(93), 373–385, 1980.

Hörhold, M. W., S. Kipfstuhl, F. Wilhelms, J. Freitag, and A. Frenzel, The densification of layered polar firn, *Journal of Geophysical Research*, *116*(F1), doi:10.1029/2009JF001630, 2011.

Hutchinson, M. F., and F. R. de Hoog, Smoothing noisy data with spline functions, *Numerische Mathematik*, *47*(1), 99–106, 1985.

Jouzel, J., M. Stiévenard, S. J. Johnsen, A. Landais, V. Masson-Delmotte, A. Sveinbjornsdottir, F. Vimeux, U. von Grafenstein, and J. W. C. White, The GRIP deuterium-excess record, *Quaternary Science Reviews*, *26*, 1–17, doi:10.1016/j.quascirev.2006.07.015, 2007.

Kaspers, K. A., R. S. W. van de Wal, M. R. van de Broeke, J. Schwander, N. P. M. van Lipzig, and C. A. M. Brenninkmeijer, Model calculations of the age of firn air across the Antarctic continent, *Atmospheric Chemistry and Physics Discussions*, *4*(2), 1817–1853, doi:10.5194/acpd-4-1817-2004, 2004.

Koutnik, M. R., Inferring histories of accumulation rate, ice thickness, and ice flow from internal layers in glaciers and ice sheets, Ph.D. thesis, University of Washington, 2009.

Koutnik, M. R., and E. D. Waddington, A well-posed model of transient ice flow near an ice divide using a spatially limited domain, *Journal of Glaciology*, 2012, In review.

Landais, A., et al., Firn-air d15N in modern polar sites and glacial-interglacial ice: a model-data mismatch during glacial periods in Antarctica?, *Quaternary Science Reviews*, *25*(1-2), 49 – 62, doi:10.1016/j.quascirev.2005.06.007, 2006.

Lemieux-Dudon, B., E. Blayo, J.-R. Petit, C. Waelbroeck, A. Svensson, C. Ritz, J.-M. Barnola, B. M. Narcisi, and F. Parrenin, Consistent dating for Antarctic and Green-

land ice cores, *Quaternary Science Reviews*, *29*, 8–20, doi:10.1016/j.quascirev.2009.11.010, 2010.

Li, J., and H. J. Zwally, Modeling the density variation in the shallow firn layer, *Annals of Glaciology*, *38*(1), 309–313, doi:10.3189/172756404781814988, 2004.

Martín, C., R. C. A. Hindmarsh, and F. J. Navarro, Dating ice flow change near the flow divide at Roosevelt Island, Antarctica, by using a thermomechanical model to predict radar stratigraphy, *Journal of Geophysical Research*, *111*(F1), doi:10.1029/2005JF000326, 2006.

Martinerie, P., D. Raynaud, D. M. Etheridge, J. Barnola, and D. Mazaudier, Physical and climatic parameters which influence the air content in polar ice, *Earth and Planetary Science Letters*, *112*(1-4), 1–13, doi:10.1016/0012-821X(92)90002-D, 1992.

Martinerie, P., V. Y. Lipenkov, D. Raynaud, J. Chappellaz, N. I. Barkov, and C. Lorius, Air content paleo record in the Vostok ice core (Antarctica) - A mixed record of climatic and glaciological parameters, *Journal of Geophysical Research-Atmospheres*, *99*(D5), 10,565–10,576, doi:10.1029/93JD03223, 1994.

McConnell, J. R., Shallow depth, age, accumulation, density and for WAIS D., preliminary data from the WAIS Divide Drilling project, 2011.

Menke, W., *Geophysical data analysis: discrete inverse theory*, Academic Press, San Diego, 1989.

Mischler, J. A., T. A. Sowers, R. B. Alley, M. Battle, J. R. McConnell, L. Mitchell, T. Popp, E. Sofen, and M. K. Spencer, Carbon and hydrogen isotopic composition of methane over the last 1000 years, *Global Biogeochemical Cycles*, *23*, doi:10.1029/2009GB003460, 2009.

Morse, D. L., E. D. Waddington, and E. J. Steig, Ice age storm trajectories inferred from radar stratigraphy at Taylor Dome, Antarctica, *Geophysical Research Letters*, *25*(17), 3383, doi:10.1029/98GL52486, 1998.

Morse, D. L., D. D. Blankenship, E. D. Waddington, and T. A. Neumann, A site for deep ice coring in West Antarctica: results from aerogeophysical surveys and thermo-kinematic modeling, *Annals of Glaciology*, *35*(1), 36–44, doi:10.3189/172756402781816636, 2002.

Nereson, N. A., and E. D. Waddington, Isochrones and isotherms beneath migrating ice divides, *Journal of Glaciology*, *48*(160), 95–108, 2002.

Nereson, N. A., C. F. Raymond, E. D. Waddington, and R. W. Jacobel, Migration of the Siple Dome ice divide, West Antarctica, *Journal of Glaciology*, *44*(148), 643–652, 1998.

Neumann, T. A., H. Conway, S. F. Price, E. D. Waddington, G. A. Catania, and D. L. Morse, Holocene accumulation and ice sheet dynamics in central West Antarctica, *Journal of Geophysical Research*, *113*, doi:10.1029/2007JF000764, 2008.

NSIDC, *Cryosphere Glossary*, National Snow and Ice Data Center, Boulder, CO, undated.

Orsi, A., WAIS divide borehole temperature record, in submission, 2008.

Orsi, A., preliminary WAIS surface temperature reconstruction, in submission, 2009.

Orsi, A., Personal communication, unpublished results, 2011.

Parker, R. L., *Geophysical inverse theory*, Princeton University Press, Princeton, N.J., 1994.

Parrenin, F., et al., The EDC3 chronology for the EPICA Dome C ice core, *Climate of the Past*, *3*(3), 485–497, 2007.

Patankar, S. V., *Numerical heat transfer and fluid flow*, Computational Methods in Mechanics and Thermal Sciences, Hemisphere Publishing Corporation, New York, 1980.

Paterson, W. S. B., *The physics of glaciers*, 3rd ed., Elsevier, Oxford, New York and Tokyo, 1994.

Paulsen, D. E., H. Li, and T. Ku, Climate variability in central China over the last 1270 years revealed by high-resolution stalagmite records, *Quaternary Science Reviews*, *22*, 691–701, doi:10.1016/S0277-3791(02)00240-8, 2003.

Petrenko, V. F., and R. W. Whitworth, *Physics of Ice*, Oxford University Press, New York, 1999.

Phillips, D. L., A technique for the numerical solution of certain integral equations of the first kind, *J. Assoc. Comput. Mach.*, *9*, 84–97, 1962.

Rasmussen, S. O., et al., A new Greenland ice core chronology for the last glacial termination, *Journal of Geophysical Research*, *111*(D6), 1–16, doi:10.1029/2005JD006079, 2006.

Raymond, M. J., and G. H. Gudmundsson, Estimating basal properties of ice streams from surface measurements: a non-linear Bayesian inverse approach applied to synthetic data, *The Cryosphere*, *3*, 265–278, doi:10.5194/tc-3-265-2009, 2009.

Reeh, N., D. A. Fisher, R. M. Koerner, and H. B. Clausen, An empirical firn-densification model comprising ice lenses, *Annals of Glaciology*, *42*(1), 101–106, doi:10.3189/172756405781812871, 2005.

Rignot, E., I. Velicogna, M. R. van den Broeke, A. Monaghan, and J. Lenaerts, Acceleration of the contribution of the greenland and antarctic ice sheets to sea level rise, *Geophysical Research Letters*, *38*(5), doi:10.1029/2011GL046583, 2011.

Scambos, T., T. Haran, M. Fahnestock, T. Painter, and J. Bohlander, MODIS-based mosaic of Antarctica (MOA) data sets: Continent-wide surface morphology and snow grain size, *Remote Sensing of Environment*, *111*, 242–257, doi:10.1016/j.rse.2006.12.020, 2007.

Schwander, J., J.-M. Barnola, C. Andri, M. Leuenberger, A. Ludin, D. Raynaud, and B. Stauffer, The age of the air in the firn and the ice at Summit, Greenland, *Journal of Geophysical Research*, *98*(D2), 2831–2838, 1993.

Schwander, J., T. Sowers, J.-M. Barnola, T. Blunier, A. Fuchs, and B. Malaizé, Age scale of the air in the Summit ice: implication for glacial-interglacial temperature change, *Journal of Geophysical Research*, *102*(D16), 19,483–19,493, doi:10.1029/97JD01309, 1997.

Schytt, V., Snow studies at Maudheim, and snow studies inland, *Scientific Results, Norwegian-British-Swedish Antarctic Expedition 1949-52*, *4*, 1958.

Sergienko, O. V., D. R. MacAyeal, and J. E. Thom, Reconstruction of snow/firn thermal diffusivities from observed temperature variation: application to iceberg C16, Ross Sea, Antarctica, 2004–07, *Annals of Glaciology*, *49*, 91–95, doi:10.3189/172756408787814906, 2008.

Severinghaus, J. P., and E. J. Brook, Abrupt climate change at the end of the last glacial period inferred from trapped air in polar ice, *Science*, *286*(5441), 930–934, doi: 10.1126/science.286.5441.930, 1999.

Severinghaus, J. P., T. Sowers, E. J. Brook, R. B. Alley, and M. L. Bender, Timing of abrupt climate change at the end of the Younger Dryas interval from thermally fractionated gases in polar ice, *Nature*, *391*(6663), 141–146, doi:10.1038/34346, 1998.

Solomon, S., D. Qin, M. Manning, Z. Chen, M. Marquis, K. Averyt, M. Tignor, and H. Miller (Eds.), *Contribution of Working Group I to the Fourth Assessment Report of the Intergovernmental Panel on Climate Change*, Cambridge University Press, Cambridge, United Kingdom and New York, NY, USA, 2007.

Spencer, M. K., R. B. Alley, and T. T. Creyts, Preliminary firn-densification model with 38-site dataset, *Journal of Glaciology*, *47*(159), 671–676, doi:10.3189/172756501781831765, 2001.

Spencer, M. K., R. B. Alley, and J. J. Fitzpatrick, Developing a bubble number-density paleoclimatic indicator for glacier ice, *Journal of Glaciology*, *52*(178), 358–364, doi: 10.3189/172756506781828638, 2006.

Steen-Larsen, H. C., E. D. Waddington, and M. R. Koutnik, Formulating an inverse problem to infer the accumulation-rate pattern from deep internal layering in an ice sheet using a Monte Carlo approach, *Journal of Glaciology*, *56*(196), 318–332, 2010.

Svensson, A., et al., A 60 000 year Greenland stratigraphic ice core chronology, *Climate Of The Past*, *4*(1), 47–57, 2010.

Taylor, K. C., et al., Dating the Siple Dome (Antarctica) ice core by manual and computer interpretation of annual layering, *Journal of Glaciology*, *50*(170), 2004.

Tikhonov, A. N., Solution of incorrectly formulated problems and the regularization method., *Sov. Math., Dokl.*, *5*, 1035–1038, 1963.

Trefethen, L. N., and D. Bau, III, *Numerical linear algebra*, Society for Industrial and Applied Mathematics (SIAM), Philadelphia, PA, 1997.

Truffer, M., The basal speed of valley glaciers: an inverse approach, *Journal of Glaciology*, *50*, 236–242, doi:10.3189/172756504781830088, 2004.

Van Trigt, R., H. A. J. Meijer, A. E. Sveinbjornsdottir, S. J. Johnsen, and E. R. Kerstel, Measuring stable isotopes of hydrogen and oxygen in ice by means of laser spectrometry: the Bølling transition in the Dye-3 (South Greenland) ice core, *Annals of Glaciology*, *35*, 125–130, doi:10.3189/172756402781816906, 2002.

Vinther, B. M., et al., A synchronized dating of three Greenland ice cores throughout the Holocene, *Journal of Geophysical Research*, *111*(D13), 1–11, doi:10.1029/2005JD006921, 2006.

Waddington, E., E. Brook, D. Morse, H. Conway, B. Barnett, and K. Taylor, Interpolation of sparse depth-age data in ice cores, and inference of accumulation-rate history: an inverse approach, *Seventh International Symposium on Antarctic Glaciology, Milano Italy, 25-29 August*, 2003.

Waddington, E. D., T. A. Neumann, M. R. Koutnik, H.-P. Marshall, and D. L. Morse, Inference of accumulation-rate patterns from deep layers in glaciers and ice sheets, *Journal of Glaciology*, *53*(183), 694–712, 2007.

Welch, B. C., and R. W. Jacobel, Analysis of deep-penetrating radar surveys of West Antarctica, US-ITASE 2001, *Geophysical Research Letters*, *30*(8), doi:10.1029/2003GL017210, 2003.

Appendix A

LIST OF TERMS

A	Flow-law softness parameter
$\dot{b}$	Accumulation rate
B	Bed elevation
c	Specific heat
g	Gravity
E_c	Activation energy from creep
E_g	Activation energy from grain growth
H	Ice-sheet thickness
K	Thermal conductivity
κ	Thermal diffusivity
n	Flow law exponent
ϕ	Horizontal velocity shape function
ψ	Vertical velocity shape function
Q	Ice flux
ρ	Density
R	Gas constant
S	Surface elevation
u	horizontal velocity
$\bar{u}$	Depth-averaged horizontal velocity
w	Vertical velocity
W	Width of flowband

Appendix B

RED NOISE

A red-noise series, $f(t)$, is also known as a Markov Process and an Autoregressive (AR-1) Process. Red noise is similar to a random walk, where each step is determined by memory of the previous step and a random component. The red noise series (Dennis Hartmann, pers. comm.) is generated by,

$$f(t + \Delta t) = \alpha f(t) + (1 - \alpha^2)^{1/2} \epsilon(t), \tag{B.1}$$

where α is the autocorrelation coefficient, $0 \leq \alpha \leq 1$, that describes the memory of previous states at the lag Δt. For perfect persistence $\alpha = 1$, and for white noise with no memory of the previous time step, $\alpha = 0$. The random noise $\epsilon(t)$ has zero mean and unit variance, and Δt is the time interval between data points. The autocorrelation function r that describes α is an exponential,

$$r(\tau) = \exp(-\tau/T), \tag{B.2}$$

and the e-folding decay time for the autocorrelation is given by,

$$T = -\Delta t / \ln \alpha. \tag{B.3}$$

For α= 0.98 and time steps Δt= 100 years, the timescale for noise is approximately 5000 years.

The synthetic ages A used in this work are the sum of the red noise scaled by the data uncertainty σ_A and true ages A_t,

$$A = f(t + \Delta t)\sigma_A + A_t. \tag{B.4}$$

Appendix C

LINEAR INVERSE PROCEDURE

The steps for the linear inverse procedure with Tikhonov regularization are shown below.

1. Guess the initial trade-off parameter ν.

2. Evaluate the model $\mathbf{m}$ using Singular Value Decomposition (SVD) as in Equation (2.19).

3. Calculate the model semi norm in Equation (2.12).

4. Calculate the residual and residual norm in Equations (2.13) and (2.14).

5. Repeat steps 2-4 until an L-curve plot similar to Figure 2.10 is generated. Select the best value for the trade-off parameter ν and cooresponding model $\mathbf{m}$ at the corner of the L-curve.

In Chapter 2 there are two inverse procedures. In the first inverse procedure the model $\mathbf{m}$ is the thinning function $\Lambda(a)$ and the data are the thinning functions known at the depth-age nodes $\Lambda(A)$. In the second inverse procedure the model is the accumulation rate $\dot{b}(a)$ and the data are the depths of known ages, $z(A)$.

Appendix D

CONDITIONING AND NUMERICAL ACCURACY

The conditioning of a nonsingular coefficient matrix $\mathbf{G}$ is important for determining the numerical accuracy of the solution to a linear system $\mathbf{Gm} = \mathbf{d}$. In mathematics literature this style of equation is conventionally termed $\mathbf{Ax} = \mathbf{b}$; however for the sake of clarity we use the labeling convention used in inverse theory literature. The condition number κ of a nonsingular matrix $\mathbf{G}$ is defined by the product of its norm and that of its inverse. When the 2-norm is used the condition number is

$$\kappa_2(\mathbf{G}) = ||\mathbf{G}^{-1}||_2 \cdot ||\mathbf{G}||_2. \tag{D.1}$$

If $\mathbf{G}$ has no inverse (for example a rectangular matrix), it is typical to use the ratio of the maximum and minimum singular values of $\mathbf{G}$, Σ_{max} and Σ_{min}.

$$\kappa(\mathbf{G}) = \frac{\Sigma_{max}}{\Sigma_{min}}. \tag{D.2}$$

For a backward stable algorithm for solving $\mathbf{Gm} = \mathbf{d}$ the relative error in the numerical solution $\tilde{\mathbf{m}}$ is determined by the machine precision ϵ_{mach} and the condition number [*Trefethen and Bau*, 1997, p. 106,166] of $\mathbf{G}$.

For the computed model $\tilde{\mathbf{m}}$ from Equation (2.17) and the true model solution $\mathbf{m}_{true}$,

$$\frac{||\tilde{\mathbf{m}} - \mathbf{m}_{true}||}{||\mathbf{m}_{true}||} \leq C\kappa\left([\mathbf{G}^T \nu \mathbf{L}^T] \begin{bmatrix} \mathbf{G} \\ \nu\mathbf{L} \end{bmatrix}\right)\epsilon_{mach}, \tag{D.3}$$

where C is a constant usually independent of the coefficient matrix $[\mathbf{G}^T \nu \mathbf{L}^T] \begin{bmatrix} \mathbf{G} \\ \nu\mathbf{L} \end{bmatrix}$ or the right hand side $[\mathbf{G}^T \nu \mathbf{L}^T] \begin{bmatrix} \mathbf{d} \\ \mathbf{0} \end{bmatrix}$. From Equation (D.3), a linear system has the order of accuracy defined by the condition number of its coefficient matrix times machine epsilon. For example, a condition number 10^{10} and double point machine precision $\epsilon_{mach} = 10^{-16}$,

would result in a relative error of roughly 10^{-6}, or 6 digits of solution accuracy in the numerical solution $\tilde{\mathbf{m}}$ when solving Equation (2.17). Increased accuracy can be achieved by solving Equation (2.17) with a method including the SVD so the $\kappa\left(\begin{bmatrix}\mathbf{G}\\ \nu\mathbf{L}\end{bmatrix}\right)$, rather than $\kappa\left(\begin{bmatrix}\mathbf{G}\\ \nu\mathbf{L}\end{bmatrix}^T\begin{bmatrix}\mathbf{G}\\ \nu\mathbf{L}\end{bmatrix}\right)$ is effectively used.

Appendix E

SINGULAR VALUE DECOMPOSITION (SVD)

To avoid instabilities from taking the inverse of a poorly conditioned matrix, we solve Equation (2.17) using the SVD. The matrices $\mathbf{U}, \mathbf{S}$ and $\mathbf{V}$ form the SVD,

$$\mathbf{U}_{m\times n}\mathbf{S}\mathbf{V}^T = \begin{bmatrix} \mathbf{G} \\ \nu\mathbf{L} \end{bmatrix}. \tag{E.1}$$

The normal-equation formulation of $\mathbf{m}$ in Equation (2.17) is solved using the SVD from Equation (E.1),

$$\mathbf{m}_{svd} = \mathbf{V}\mathbf{S}^{-1}\mathbf{U}^T \begin{bmatrix} \mathbf{d} \\ \mathbf{0} \end{bmatrix}. \tag{E.2}$$

Recognizing the $\mathbf{U}^T$ matrix is composed of two parts, $\mathbf{U_q}^T$ and $\mathbf{U_0}^T$,

$$\mathbf{U}^T = [\mathbf{U}_q^T \quad \mathbf{U}_0^T], \tag{E.3}$$

where the $\mathbf{U_0}^T$ matrix is multiplied by the zero vector in Equation (E.2) and $\mathbf{U_q}^T$ multiplies the $q \times 1$ vector $\mathbf{d}$. We combine Equations (E.2) and (E.3) as follows,

$$\mathbf{m}_{svd} = \mathbf{G}^{\#}_{svd}\mathbf{d} = \mathbf{V}\mathbf{S}^{-1}\mathbf{U_q}^T\mathbf{d}. \tag{E.4}$$

Equation (E.4) is equivalent to Equation (E.2) and is dimensionally correct for statistical analysis in Appendix F.

Appendix F

UNCERTAINTY AND RESOLUTION

We determine the model covariance and resolution [*Aster et al.*, 2005; *Menke*, 1989; *Hansen*, 1998] assuming that data errors are independent and normally distributed. The estimated model parameters have a multivariate-normal distribution with model covariance

$$\mathbf{C}_m = \mathbf{G}^{\#}_{svd}\mathbf{C}_d\mathbf{G}^{\#T}_{svd}. \tag{F.1}$$

The generalized inverse matrix $\mathbf{G}^{\#}$ has already been scaled by the uncertainty (Equation 2.5), and the model covariance is

$$\mathbf{C}_m = \mathbf{G}^{\#}_{svd}\mathbf{G}^{\#T}_{svd}. \tag{F.2}$$

The one standard deviation, $\sigma_{\mathbf{m}}$, is the square root of the diagonal of the model covariance and has components,

$$\sigma_{m_k} = \sqrt{\mathbf{C}_{m_{kk}}}. \tag{F.3}$$

We show the 1-σ 66% confidence interval as $\mathbf{m} \pm \sigma_{\mathbf{m}}$ in Figure 2.5.

The resolution matrix, $\mathbf{R}_m$, defined as

$$\mathbf{R}_m = \mathbf{G}^{\#}_{svd}\mathbf{G}, \tag{F.4}$$

describes how well the model solution is resolved by the model geometry. A characteristic of zero-order Tikhonov regularization is a symmetric resolution matrix; however, higher order Tikhonov regularization matrices can be asymmetric depending on the symmetry of $\mathbf{G}$. The ideal case is a resolution matrix equivalent to an identity matrix, which has perfect resolution. The columns of the resolution matrix are called resolution kernels. The model resolution matrix can be tested for how well a true model $\mathbf{m}_{true}$ may be recovered by the inverse problem. The expected solution $\mathbf{m}_E$,

$$\mathbf{m}_E = \mathbf{R}_m\mathbf{m}_{true}. \tag{F.5}$$

We use two tests to examine the resolution of the inverse method. The first test is a spike model test. These kernels are the equivalent of multiplying delta functions (set as $\mathbf{m}_{true}$ in Figures 2.11 and 2.12) by the resolution matrix. For perfect resolution, the resulting $\mathbf{m}_E$ is a delta function; however, in practice the dependence of any particular model parameter on other model parameters depends largely on the nature of the forward problem.

The second resolution test is performed to estimate the resolution of each model solution. The $\mathbf{m}_{true}$ vector is set to the accumulation rate used to make the synthetic data. For the steady-state inverse problems $\mathbf{m}_{true}$ is composed of ones, the non-dimensional accumulation rate used to make the data. For the transient inverse problems $\mathbf{m}_{true}$ is composed of a time-varying accumulation rate (with dimensional form in Figure 2.16) used to make the data.

Appendix G

SELF-CONSISTENT MODEL ICE-SHEET PARAMETERS

Ice-sheet parameters used to create the synthetic data in the dynamic forward problem and in the two-dimensional inverse method in Box 1 of Figure 4.11.

g	Gravity	9.8 m s^{-2}
A	Flow-law softness parameter	4.0×10^{-4} $kPa^{-3}s^{-1}$
B	Bed elevation	0 m
c	Specific heat	2093 J $kg^{-1}K^{-1}$
q_{geo}	Geothermal flux	0.055 W m^{-2}
T_s	Surface temperature	243.45 K
n	Flow-law exponent	3
h_d	divide kink height	0.2
h_f	flank kink height	0.2
ρ	Density	917
W	Width of flowband	1
	Spatial domain, total	45 km
Δx	Spatial step size	900 m
$\Delta\hat{z}$	Non-dimensional vertical step size	0.001
	Time domain, total	70 ka
Δt	Time step size	700 a

Appendix H

DYNAMIC FLOWBAND MODEL

A dynamical 2-d flow band model determines radar layer depths along the flow band based on an accumulation rate $\dot{b}(x,t)$. The dynamical model is used to determine the surface elevation, surface elevation change, and shape functions, used in the kinematic inverse problem. Non-dimensional height $\bar{z}$ is evaluated based on the surface elevation S and bed height B,

$$\bar{z} = \frac{z - S}{S - B} \tag{H.1}$$

The dynamic flux Q,

$$Q(x,t) = W(x) \int_{B(x)}^{S(x,t)} u(x,\zeta,t) d\zeta = W(x) H(x,t) \bar{u}(x,t). \tag{H.2}$$

The flow band model includes a variable width W to account for divergence in the direction of flow x. We prescribe the width along the flow band $W(x)$ and allow W to change when necessary based on the continuity equation.

The depth-averaged velocity $\bar{u}$,

$$\bar{u}(x,t) = 2A\left(\rho g \frac{\partial S(x,t)}{\partial x}\right)^n \int_0^1 \int_0^{\hat{z}} \exp\left(-\frac{Q}{RT(\hat{\zeta},t)}\right)(1-\hat{\zeta})^n d\hat{\zeta} d\hat{z}. \tag{H.3}$$

The velocity shape functions ϕ and ψ describe the shape of the horizontal and vertical velocities $u(x,\hat{z})$ and $w(x,\hat{z})$. The shape function ϕ derived using a shallow ice flow approximation with an isothermal, parallel-sided slab,

$$\phi(x,\hat{z}) = \left(\frac{n+2}{n+1}\right)(1 - (1 - \hat{z}^{n+1})). \tag{H.4}$$

The vertical velocity shape functions ψ is defined as

$$\psi(x,\hat{z}) = \left(\frac{n+2}{n+1}\right)\left(\hat{z} - \frac{1}{n+2}\right)\left(1 - (1-\hat{z})^{n+2}\right). \tag{H.5}$$

Shape functions are assumed to be constant for the distance x along the flow band. It is possible to include shape functions that reflect site appropriate dynamics, which may include melting and ice-divide related flow effects [*Nereson and Waddington*, 2002].

We use velocity shape functions from *Nereson and Waddington* [2002], which allow the transition from divide to flank flow. The horizontal-velocity shape function is based on the shape function at the divide ϕ_d and at the flank ϕ_f as a linear mixture,

$$\phi(x, \hat{z}, t) = \alpha(x)\phi_d(\hat{z}, t) + [1 - \alpha(x)]\phi_f(\hat{z}, t). \tag{H.6}$$

The factor $\alpha(x)$ defines the proportion of divide flow and flank flow. The horizontal-velocity shape functions [*Dansgaard and Johnsen*, 1969] for the flank ϕ_f and divide ϕ_d are defined based on height z in relation to the kink height h,

$$\phi_{f,d}(\hat{z}, t) = \frac{1}{1 - h_{f,d}/2}\frac{z}{h} \qquad z < h_{f,d} \tag{H.7}$$

$$\phi_{f,d}(\hat{z}, t) = \frac{1}{1 - h_{f,d}/2} \qquad z \geq h_{f,d} \tag{H.8}$$

The vertical-velocity shape functions [*Dansgaard and Johnsen*, 1969] for the flank and divide are defined as

$$\psi_{f,d}(\hat{z}, t) = \frac{1}{1 - h_{f,d}/2}\frac{z^2}{2h_{f,d}} \qquad z < h_{f,d} \tag{H.9}$$

$$\psi_{f,d}(\hat{z}, t) = \frac{1}{1 - h_{f,d}/2}(z - h/2) \qquad z \geq h_{f,d} \tag{H.10}$$

We use the kink height h=0.2 for the divide and flank, h_d and h_f.

The velocity field is be evaluated from the shape functions and depth-averaged velocities. The horizontal velocity evaluated for each time step,

$$u(x, \hat{z}) = \bar{u}(x)\phi(x). \tag{H.11}$$

The vertical velocity evaluated for each time step is evaluated based on the horizontal velocity assuming continuity,

$$w(x, \hat{z}) = -(\dot{b} - \frac{dS}{dt})\psi(x) + u\left(\frac{dB}{dx}(1 - \hat{z}) + \frac{dS}{dx}\hat{z}\right) - H(x)\bar{u}\int \frac{d\phi(x, \hat{z})}{dx}dz. \tag{H.12}$$

The ice-sheet thickness changes $\partial H/\partial t$ are evaluated for each time step,

$$\frac{\partial H(x, t)}{\partial t} = -\frac{1}{W(x)}\left(\frac{\partial Q(x, t)}{\partial x}\right) + \dot{b}(x, t). \tag{H.13}$$

Integrating the velocities u and w over a time step Δt allows particle tracking from the surface to a predicted layer at depth $\hat{z}$.

Appendix I

KINEMATIC FLOWBAND MODEL

A 2-d kinematic flow-band model has been developed to predict the shape of radar layers when subjected to transient accumulation-rate histories $\dot{b}(x,t)$. With distance along flow-band x we assume a spatially uniform constant ice sheet thickness $H(x)$, defined as the difference in the bed $B(x)$ and surface $S(x)$. The flow-band width W is assumed to be constant and equal to 1. Figure I.1 shows a representation of the 2-d kinematic model domain.

The non-dimensional height $\hat{z}$ is defined in terms of the surface and bed elevations,

$$\hat{z} = \frac{z - B}{S - B}. \tag{I.1}$$

Variation in the accumulation rate is accounted for in the ice-sheet flux Q,

$$Q = Q_{in} + \int_{x_{in}}^{x_{end}} \left(\dot{b}(x) - \frac{dS(x)}{dt} - \frac{dm(x)}{dt} \right) W(x) dx. \tag{I.2}$$

The flux into the domain, Q_{in} is assigned from the dynamic code boundary condition.

Determining Q between nodes where W and $\dot{b}$ are known involves using gamma functions. The depth-averaged velocity $\bar{u}(x)$ along the flow band is defined as,

$$\bar{u}(x) = \frac{Q(x)}{W(x)H(x)}. \tag{I.3}$$

Equation I.3 is evaluated for the accumulation-rate at each time step. This method makes the assumption that the velocity field is a steady-state solution for each time step.

The velocity field is be evaluated from the shape functions and depth-averaged velocities. The horizontal velocity evaluated for each time step,

$$u(x, \hat{z}) = \bar{u}(x)\phi(x). \tag{I.4}$$

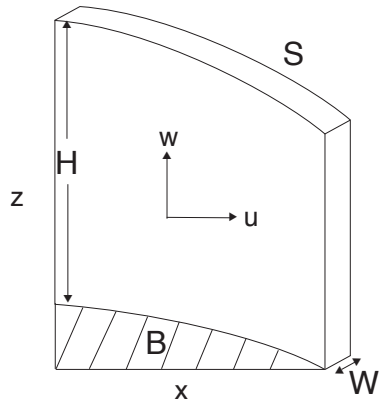

Figure I.1: The 2-d kinematic flow-band model has a spatially varying bed and surface elevations that are constant in time.

The *Nereson and Waddington* [2002] shape functions used in the dynamical forward problem are used also in the kinematic forward problem.

The vertical velocity evaluated for each time step is evaluated based on the horizontal velocity assuming continuity,

$$w(x,\hat{z}) = -(\dot{b} - \frac{dS}{dt})\psi(x) + u\left(\frac{dB}{dx}(1-\hat{z}) + \frac{dS}{dx}\hat{z}\right) - H(x)\bar{u}\int \frac{d\phi(x,\hat{z})}{dx}dz. \tag{I.5}$$

Integrating the velocities u and w over a time step Δt allows particle tracking from the surface to a predicted layer at depth $\hat{z}$.

VITA

Jessica Lundin is at the Glaciology Group in the Earth and Space Sciences Department at the University of Washington.